

# Aerothermodynamic Environment Estimation Throughout the Entry Corridor from Discrete High Fidelity Solutions

Andrew J. Hyatt\* and Kate E. Johnson\*

*NASA Johnson Space Center, Houston, TX, United States of America*

Accurate prediction of aerothermodynamic environments is critical to Thermal Protection System design and mission success. Engineering correlations exist for predicting aerothermodynamic environments for various geometries and flight conditions, but generally more accurate approaches are required for detailed design. Approaches have been developed to use mission specific high-fidelity Computational Fluid Dynamics solutions to provide environments on the entire surface of the spacecraft. Each of these approaches provides approximations between high-fidelity solutions using different independent parameters to correlate or interpolate. In this investigation, a series of high-fidelity solutions have been used to interpolate in a number of different interpolation spaces, including those used in previous approaches. Six aerothermodynamic environment parameters have been considered, including heat flux, pressure, shear stress, edge Mach number, boundary layer thickness, and momentum thickness Reynolds number. The Log( $\rho$ ), Log(V),  $\alpha$  interpolation space was found to provide the most accurate approximation of the aerothermodynamic environments between the high-fidelity solutions. The investigation also found that the interpolation accuracy for heat flux, pressure, and edge Mach number was relatively insensitive to the high-fidelity solution resolution, though constraining the spacing to no more than 900 m/s and 5800 meters in the velocity and altitude dimensions respectively was found to estimate 99% of the heat flux values on the heatshield within  $\pm 5\%$ , for the Apollo spacecraft and corresponding re-entry corridor considered in this investigation. These constraints were identified while developing a method for recommending high-fidelity solution resolution for an interpolation space of interest, which has also been described. The shear stress and boundary layer thickness were sensitive to the resolution of the interpolation space.

## Nomenclature

<i>BLPROP</i>	Boundary Layer Property Prediction
<i>CBAERO</i>	Configuration Based AERodynamics
<i>CFD</i>	Computational Fluid Dynamics
<i>CM</i>	Command Module
<i>CPU</i>	Central Processing Unit
<i>DPLR</i>	Data Parallel Line Relaxation
<i>LEO</i>	Low Earth Orbit
<i>M</i>	Mach number
<i>M<sub>e</sub></i>	Edge Mach number
<i>MPI</i>	Message Passing Interface
<i>P</i>	Pressure
<i>p</i>	Parameter of interest
<i>q</i>	Dynamic pressure
<i>q<sub>c</sub></i>	Convective heat flux
<i>q<sub>ref</sub></i>	Heat flux (engineering correlation estimate)

---

\* Aerospace Engineer, NASA Johnson Space Center, 2101 E. NASA Pkwy, Houston, TX, AIAA Member.

$q_w$	Heat flux
$R$	Radius
$Re$	Reynolds number
$Re_\theta$	Momentum thickness Reynolds number
$SCEBD$	Self-Consistent Effective Binary Diffusion
$STEAM$	Software Toolkit for Engineering and Aeroscience Models
$T$	Temperature
$T_r$	Rotational temperature
$T_t$	Translational temperature
$T_v$	Vibrational temperature
$TPS$	Thermal Protection System
$V$	Velocity
<i>Greek</i>	
$\alpha$	Angle-of-Attack
$\delta$	Boundary Layer Thickness
$\epsilon$	Emissivity
$\mu$	Mean
$\mu_\infty$	Freestream Viscosity
$\rho$	Density
$\sigma$	Standard Deviation
$\tau_w$	Shear Stress
<i>Subscript</i>	
$c$	Convective
$e$	Boundary layer edge
$\infty$	Freestream
$\theta$	Momentum thickness
$n$	Normalized
$r$	Rotational
$ref$	Reference (engineering correlation estimate)
$poi$	Point of Interest
$t$	Translational
$v$	Vibrational
$w$	Wall

## I. Introduction

Atmospheric entry of both robotic and human exploration spacecraft can lead to extreme aerothermodynamic environments. Design of the Thermal Protection System (TPS) to protect the astronauts and payloads requires accurate characterization of the environment. For smaller spacecraft, characterizing the heat flux at the stagnation point may be sufficient to design the TPS.

Correlations exist for the stagnation point convective heat flux. Some of the earliest examples include Fay and Riddell<sup>1</sup> in 1958, Marvin and Deiwert<sup>2</sup> in 1966, and Sutton and Graves<sup>3</sup> in 1971. In 2014, Brandis and Johnson<sup>4</sup> developed updated correlations for stagnation point heat flux using modern coupled Computational Fluid Dynamics (CFD) and shock layer radiation solutions,

For  $3 \text{ km/s} \leq V < 9.5 \text{ km/s}$ :

$$q_c = 7.455 \times 10^{-9} \rho_\infty^{0.4705} V_\infty^{3.089} R^{-0.52} \quad (1)$$

For  $9.5 \text{ km/s} \leq V < 17 \text{ km/s}$ :

$$q_c = 1.270 \times 10^{-6} \rho_\infty^{0.4678} V_\infty^{2.524} R^{-0.52} \quad (2)$$

For a specific spacecraft with a defined or effective heat shield radius, these correlations simplify to the form:

$$q_c = C \rho_\infty^M V_\infty^N \quad (3)$$

These correlations are very powerful because of how fast they can provide estimates. They can be used early in the design process to help narrow down candidate TPS materials on a given trajectory or, to some extent, to define the entry corridor possible for a specific TPS. However, all these correlations are limited to the stagnation point.

For larger or more complex spacecraft, it becomes critical to consider the environments away from the stagnation point. Larger spacecraft may experience boundary layer transition leading to turbulent heat fluxes that exceed the heat flux at the stagnation point. Spacecraft that attach to the launch vehicle through the heatshield often have features away from the stagnation point that are less capable and experience higher heat fluxes than the acreage TPS. These are just a couple reasons it may be critical to evaluate the environments on the entire spacecraft.

In 1999, Olynick et. al<sup>5</sup> outlined an approach to predict the pressure, heat flux, and surface shear over the entire surface of the spacecraft. This approach required a series of roughly eight CFD solutions along a design trajectory to develop a unique fit of the CFD solutions at each location on the surface. This fit followed the familiar form of the stagnation point correlations,

$$P, q_c, \tau = C \rho_\infty^M V_\infty^N \quad (4)$$

and used an optimization scheme, such as least squares, to determine the C, M, and N values that best fit the CFD solutions at each location on the surface of the spacecraft. These correlations could then be extended to other trajectories for the same geometry.

In 2006, Greene and Hamilton<sup>6</sup> developed the Boundary Layer Property Prediction (BLPROP) tool in support of the Space Shuttle Program Return to Flight effort. The tool used a database of high-fidelity solutions and interpolated between them to the desired flight condition. BLPROP first interpolated in angle-of-attack. From there, a normalization step was performed prior to interpolating in Mach number. The normalization step was then reversed after interpolation was complete, and was used to account for differences in Reynolds number between the database solutions and the desired flight condition.

Finally, in 2007, Kinney<sup>7</sup> proposed using high-fidelity CFD solutions to *anchor* the engineering solutions provided by Configuration Based Aerodynamics (CBAERO).<sup>8</sup> The anchoring process started by calculating correction factors, the ratio of the high-fidelity CFD solution quantity over the engineering prediction quantity, at each available CFD solution. The correction factors are then interpolated to, and used to update, all the CBAERO solutions in the database in Mach, dynamic pressure, and angle-of-attack space, or any set of two of those parameters. The aerothermodynamic environment along a desired trajectory can then be interpolated from these anchored CBAERO solutions in the same Mach, dynamic pressure, and angle-of-attack space.

Each of these existing approaches use vehicle specific CFD solutions and either 1) curve fit them or 2) interpolate between them to provide the desired environments along a given trajectory. However, each use a different interpolation scheme. The objective of this paper is to investigate directly interpolating between CFD solutions for the dependent parameters of interest, including convective heat flux ( $q_w$ ), pressure ( $P_w$ ), shear stress ( $\tau_w$ ) magnitude, edge Mach number ( $M_e$ ), boundary layer thickness ( $\delta$ ), and momentum thickness Reynolds number ( $Re_\theta$ ). Heat flux ( $q_w$ ) is critical for material response modeling used to determine the temperature distribution throughout the TPS and the level of recession for ablative materials. Pressure ( $P_w$ ) is critical for aerodynamics and is often used to correlate material properties in material response modeling as well. Some materials also have shear stress ( $\tau_w$ ) capability limits. The edge Mach number ( $M_e$ ) and momentum thickness Reynolds number ( $Re_\theta$ ) are often used in the development of boundary layer transition models.<sup>9,10</sup> Lastly, boundary layer thickness ( $\delta$ ) is sometimes used to develop engineering augmentation models for geometric features.<sup>11,12</sup> Given how shear stress ( $\tau_w$ ), edge Mach number ( $M_e$ ), boundary layer thickness ( $\delta$ ), and momentum thickness Reynolds number ( $Re_\theta$ ) are used, they are less critical near the stagnation point where the notion of a boundary layer breaks down.

For this investigation, various interpolation spaces are considered for each parameter. The investigation then explores the change in accuracy as the number of CFD solutions used to construct the interpolation spaces is reduced. CFD solutions can be computationally expensive so identifying the required number to achieve a desired accuracy can be beneficial. Finally, the paper investigates a method for recommending altitude and velocity database spacing constraints based on an interpolation space and dependent variable of interest.

## II. Background

The Apollo geometry was selected for this investigation due to the relevance to many current NASA and commercial spacecraft while avoiding proprietary and export concerns. The Apollo re-entry capsule had a spherical heatshield, 3.912 meters in diameter, shown in Figure 1. Similarly, the Orion, SpaceX Dragon, and Boeing Starliner re-entry capsules are all blunt bodies with spherical heatshields, ranging in size from 4 to 5 meters. For example, the Orion Crew Module uses a spherical heatshield 198 inches (5.0292 meters) in diameter.<sup>14</sup> The Apollo 4 trajectory is particularly relevant for Orion since it re-entered at lunar return velocity, and so that will be the focus for this investigation.

Apollo 4 was an uncrewed flight test of the Saturn V launch vehicle and the Command Module (CM) that eventually took astronauts to the Moon. The mission launched from the Kennedy Space Center on November 9, 1967 and splashed down in the Pacific Ocean later that same day. The re-entry trajectory is shown in Figure 2. The spacecraft starts on the top right of the figure at entry interface (velocity of roughly 11 km/s and altitude of 120 km) and decelerates until it reaches splashdown on the bottom left of the figure.

To facilitate this investigation, 185 discrete high-fidelity CFD solutions were computed. These solutions only modeled half of the heatshield. By neglecting roll, symmetry could be assumed across the pitch plane reducing the computational cost by a factor of two. Modeling the backshell, particularly the separated wake region, was also out of scope for this investigation which allowed the solution domain to be truncated at the heatshield shoulder. These two limitations significantly reduced the computational cost of generating the set of high-fidelity solutions.

### A. Grid

The grid used for the CFD solutions is shown in Figure 3. The grid terminated at the shoulder because this investigation focused on the heatshield and did not include the conic backshell. The grid was composed of four point matched blocks, outlined in magenta, and included 25,088 surface cells. The surface grid was then extruded 128 steps to generate a volume grid of 3,211,264 cells. Figure 3a shows only the surface grid and Figure 3b includes the surface along with the pitch plane and the exit plane of the extruded volume grid prior to grid adaptation.

A grid resolution study was performed to ensure the CFD solutions were grid independent. The grid used to calculate the series (database) of solutions was actually a sequenced version of a more resolved grid that was generated on the Apollo heat-shield geometry. Table 1 shows the dimensions of both the original and the sequenced grids. Solutions were computed on both grids at the 7.5 km/s, 60 km altitude, angle-of-attack of 156 degree condition. The full resolution grid was shock aligned and clustered using the built in capability within the CFD solver to achieve a cell Reynolds number at the wall of 0.5, which was half of the standard setting used for the database cases. Figure 4 illustrates the differences between the two

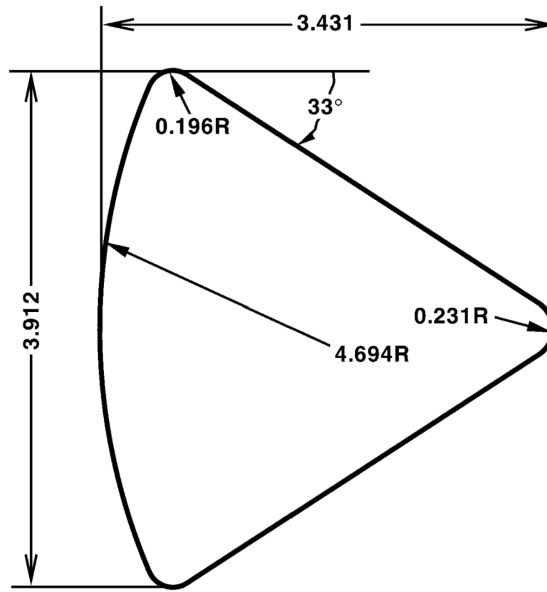


**Figure 1.** Schematic of the Apollo Command Module.<sup>13</sup> All dimensions are in units of meters.

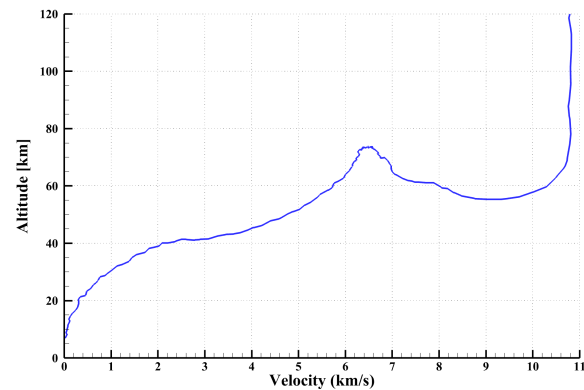
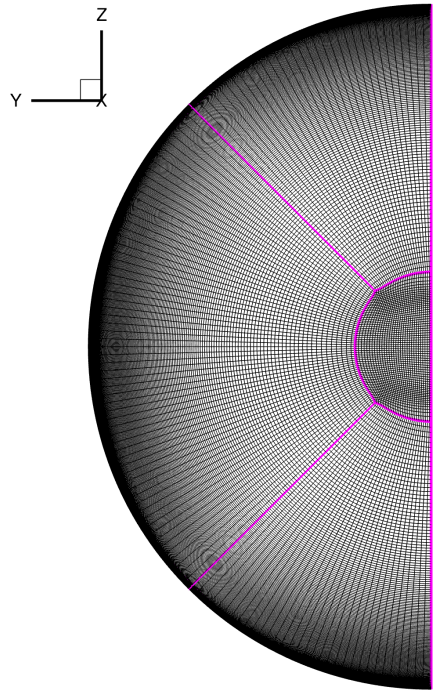
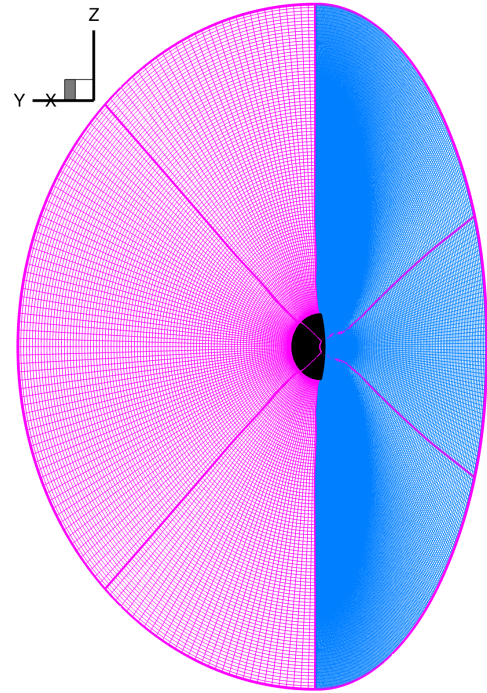


**Figure 2.** Apollo 4 re-entry trajectory.



(a) Surface grid



(b) Surface grid with pitch plane (blue) and exit plane (magenta) at the heatshield shoulder

**Figure 3.** Initial CFD grid prior to shock tailoring. The mesh is composed of four point matched blocks, which are outlined in magenta.

grids in the I and J dimensions (on the surface) and in the pitch plane. The sequenced grid was created by removing every other cell from the shock aligned full resolution grid. Figure 5 compares the computed heat fluxes on the two grids. Figure 5(c) shows the percent difference between the computed solutions. The differences over much of the heat-shield were nearly zero, and the largest differences were less than 2%, verifying that the sequenced grid was adequate for the CFD solutions computed for this investigation.

Block	Full Grid			Sequenced Grid		
	I	J	K	I	J	K
1	128	64	256	64	32	128
2	360	64	256	180	32	128
3	360	128	256	180	64	128
4	360	64	256	180	32	128

**Table 1.** Grid cell count for both the full and sequenced versions of the grid.

## B. CFD

The Data Parallel Line Relaxation (DPLR)<sup>15</sup> code was used to generate each of the CFD solutions. DPLR uses a finite volume approach to solve the Navier-Stokes equations and includes both thermal and chemical non-equilibrium, allowing it to accurately predict aerothermal environments on spacecraft at Low Earth Orbit (LEO), lunar, and interplanetary entry velocities. It also leverages Message Passing Interface (MPI) to run in parallel and scales efficiently on modern CPU compute clusters.

All of the solutions used the same set of physical models. This initial investigation only considered laminar solutions and each used the 11-species Park 90<sup>16</sup> chemistry model. The solutions assumed vibrational

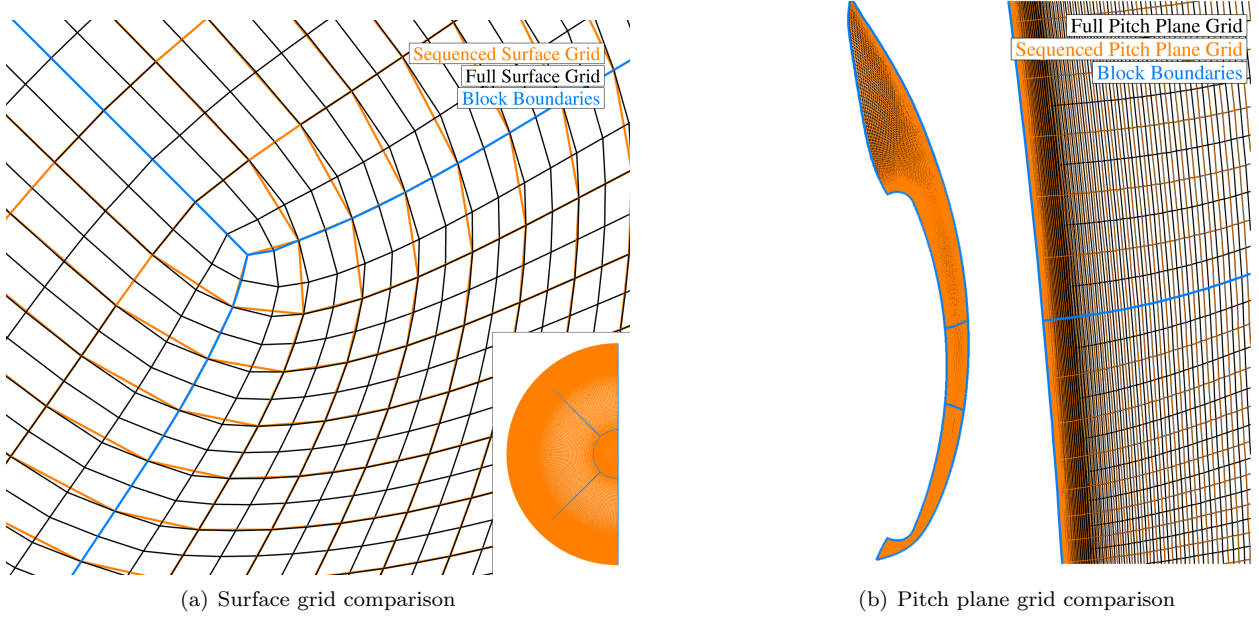


Figure 4. Comparison of the full resolution grid and the sequenced grid. The full resolution grid is shown in black and the sequenced grid in orange. The block boundaries are shown in blue.

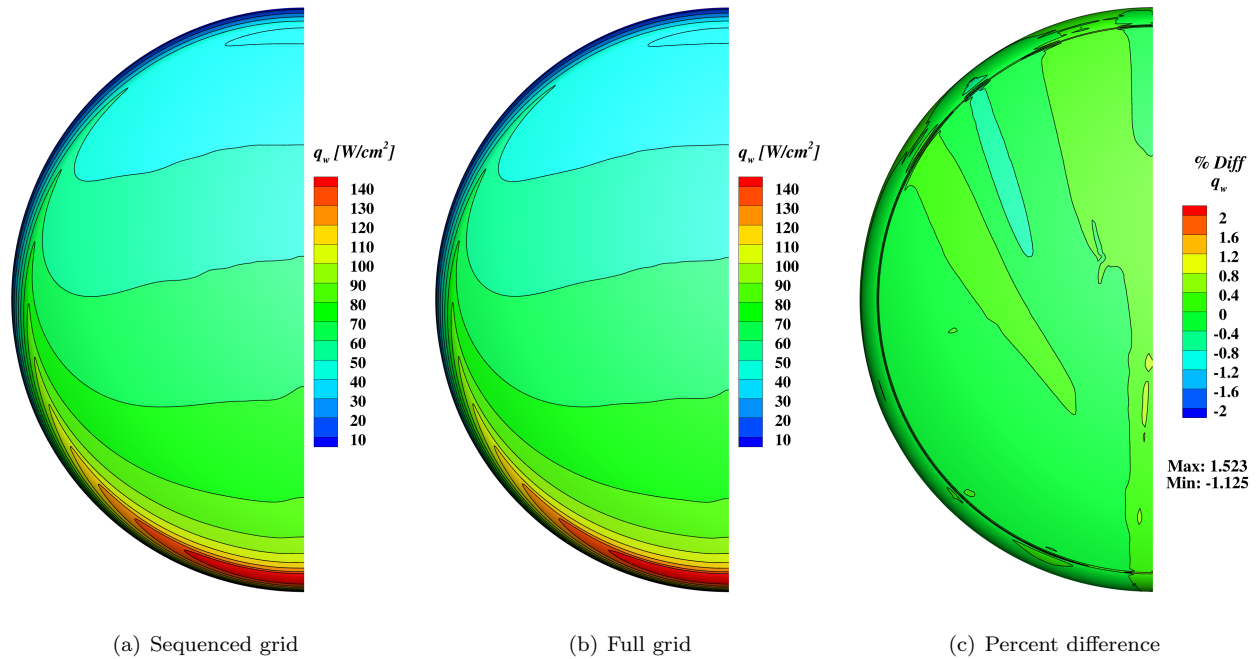
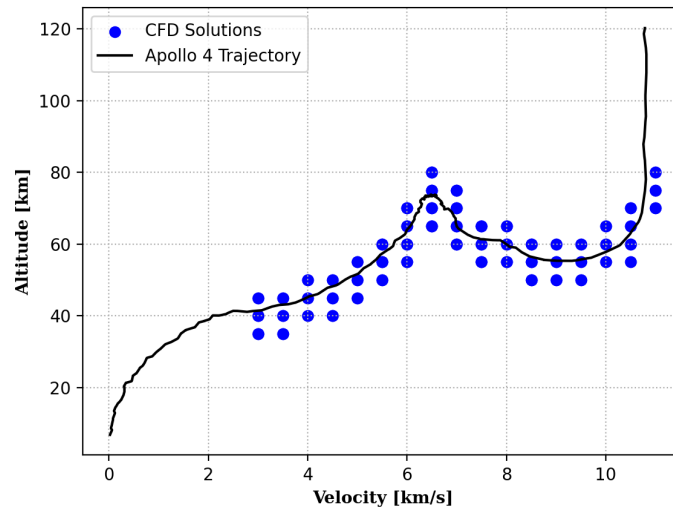


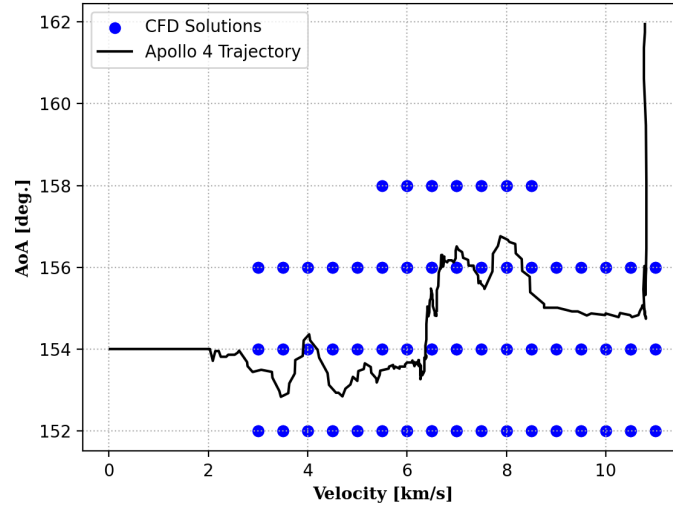
Figure 5. Comparison of the computed heat flux on the sequenced grid (database resolution) and the full resolution grid. The percent difference in computed heat flux between the two grids was less than 2%.

non-equilibrium by including a second temperature ( $T_v$ )<sup>17</sup> which was decoupled from the translational temperature ( $T_t$ ). The rotational ( $T_r$ ) temperature was coupled with the translational temperature. The surface was assumed to be fully catalytic and in radiative equilibrium with an emissivity ( $\epsilon$ ) of 0.85. The diffusion was modeled with Self-Consistent Effective Binary Diffusion (SCEBD).<sup>18</sup>

CFD solutions were generated around the Apollo 4 trajectory, between 3 km/s and 11 km/s at increments of 0.5 km/s. Three or four densities were assumed at each velocity, corresponding to altitudes in round kilometers. The 1976 standard atmosphere<sup>19</sup> was assumed to calculate the air density and temperature that correspond to each altitude. Finally, at each velocity and density combination, three or four angles-of-attack were assumed, leading to the 185 unique CFD solutions, depicted in Figure 6 and specified in Appendix B. A sample CFD solution is shown in Figure 7. The heat flux ( $q_w$ ) contours are shown on the surface and Mach contours are shown on the pitch plane. Note the solution domain has been reduced to a region starting just outside the shock down to the surface, as compared to the original volume grid shown in Figure 3b.



(a) CFD solutions in altitude versus velocity space



(b) CFD solutions in angle-of-attack versus velocity space

**Figure 6.** Discrete CFD solutions shown as blue freckles with the Apollo 4 trajectory included in black.

Each CFD solution was post-processed using the BLAYER<sup>20</sup> tool to identify the edge of the boundary layer and determine the boundary layer parameters of interest ( $M_e$ ,  $\delta$ ,  $Re_\theta$ ). BLAYER uses the total enthalpy profile from the surface to the outer boundary along grid lines in the off body direction to identify the edge of the boundary layer.

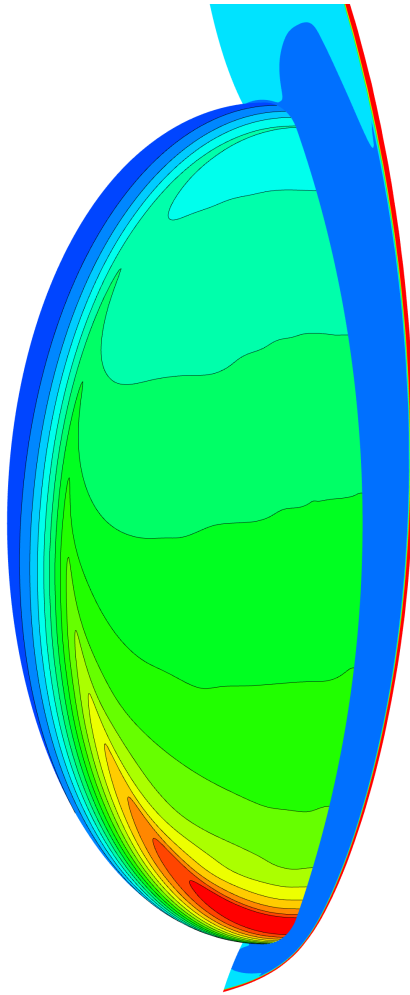


**Figure 7.** Sample CFD solution at a velocity of 6.5 km/s, 65 km altitude, and 154 degrees angle-of-attack. The surface contours show the heat flux and the pitch plane shows Mach contours.

### C. Interpolation Space

The discrete CFD solutions were used to generate a number of interpolation spaces for evaluation. The interpolation spaces were generated by creating a convex hull that encapsulated the desired CFD solutions, which could be the full set or any subset of solutions using the Python SciPy implementation of Delaunay triangulation,<sup>21</sup> leading to a series of tetrahedron for a three dimensional interpolation space. Solutions could then be generated at any point within this convex hull by 1) determining the element (tetrahedron) that contained the point of interest, 2) calculating the barycentric weights of the vertices of the element with respect to the point of interest, and 3) using the barycentric weights to weight the contribution from the solution corresponding to each vertex in the interpolation of the dependent parameter set. Dependent parameters included surface heat flux ( $q_w$ ), surface pressure ( $P_w$ ), surface shear stress ( $\tau_w$ ), and boundary layer properties such as edge Mach number ( $M_e$ ), boundary layer thickness ( $\delta$ ), and momentum thickness Reynolds number ( $Re_\theta$ ). The independent parameters used for interpolation could be any combination of parameters used to define flight spaces or trajectories, such as velocity ( $V$ ), density ( $\rho$ ), angle-of-attack ( $\alpha$ ),

Mach (M), dynamic pressure (q), and any derived quantities after applying a function to these parameters, like ( $V^3$ ) or ( $\log \rho$ ).

Figure 8a shows the convex hull for the three-dimensional interpolation space that is linear in density, velocity, and angle-of-attack. A slice through the same interpolation space at angle-of-attack of 154 degrees is shown in Figure 8b. This interpolation space is not expected to give the highest accuracy for any parameter of interest, but it is easier to visualize than many others.

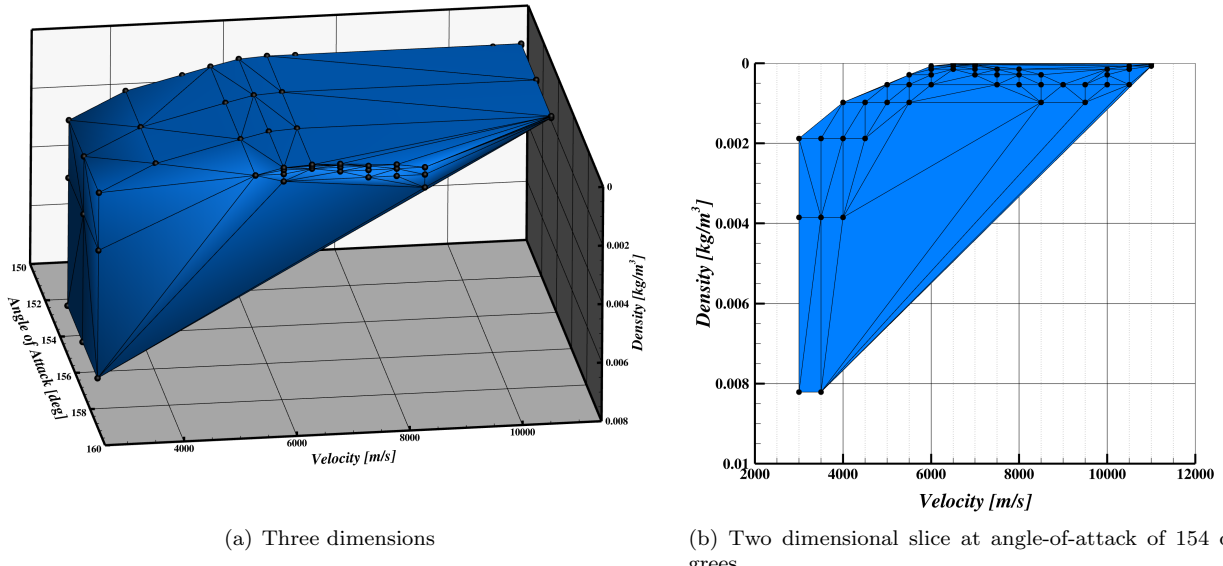


**Figure 8. Interpolation space convex hull created in dimensions of density, velocity, and angle-of-attck.**

An in-house Python library referred to as the Software Toolkit for Engineer and Aeroscience Models (STEAM)<sup>22</sup> was used to generate the interpolation spaces and generate solutions at any point of interest within a given interpolation space. STEAM made it possible to quickly generate a number of interpolation spaces using different combinations of independent parameters (or derived quantities) and different subsets of the database of CFD solutions. STEAM also provided the ability to scale each of the independent parameters so interpolation was performed in a unit cube, thereby giving equal weighting to each dimension of the interpolation space.

### III. Results

The results have been divided into three sections. The first focuses on defining the interpolation space that provides the most accurate prediction of each dependent parameter of interest. The second uses the recommended interpolation spaces and explores how the accuracy degrades with reduced CFD solution resolution in each dimension. The last section investigates a method to assess database coverage for a parameter of interest within a given interpolation space. While the method is applicable to all parameters of interest, the focus was on heat flux ( $q_w$ ) and spacing constraints in the altitude and velocity dimensions are recommended.

#### A. Interpolation Space Evaluation

A number of interpolation spaces were considered and evaluated, where each parameter was a separate dimension of the interpolation space. These interpolation spaces are listed below:

1.  $\rho, V^2, \alpha$
2.  $\sqrt{\rho}, V^3, \alpha$

3.  $M, q, \alpha$
4.  $M, \alpha$
5.  $\log \rho, \log V, \alpha$

As pointed out in Olynick et. al.<sup>5</sup> the surface pressure is nearly proportional to  $\rho V^2$  and convective heat flux is nearly proportional to  $\rho V^3$ . The heat flux relation was reinforced by those proposed by Sutton and Graves<sup>3</sup> as well as Brandis and Johnson.<sup>4</sup> Ultimately the first two interpolation spaces were considered because the independent dimensions were known to fit pressure and heat flux when combined. The third and fourth interpolation spaces were considered because they were used by Greene and Hamilton,<sup>6</sup> as well as CBAERO.<sup>8</sup> Finally, the last interpolation space was considered because the stagnation heat flux was nearly planar when plotted in  $\log(\rho), \log(V)$  space, as shown in Figure 9.

Two approaches were considered for interpolating within each of these interpolation spaces. The first approach interpolated for each of the dependent parameters ( $q_w, P_w, \tau_w, M_e, \delta, Re_\theta$ ) directly, referred to as dimensional or direct interpolation within this manuscript. A second approach followed a similar approach to that used in Greene and Hamilton<sup>6</sup> to 1) normalize the dependent parameters, 2) interpolate for these normalized parameters within the interpolation space to the point of interest, and 3) redimensionalize back to the desired dimensional parameters, referred to as normalized interpolation within this manuscript. Table 2 shows the quantity used to normalize each of the dependent parameters of interest. While Greene and Hamilton<sup>6</sup> used Fay and Riddell<sup>1</sup> to normalize the heat flux, this study instead used Sutton and Graves<sup>3</sup> due to its simplicity.

$$\begin{aligned}
q_{w_n} &= q_w/q_{ref} \\
P_{w_n} &= P_w/\rho_\infty V_\infty^2 \\
\tau_{w_n} &= \tau_w/\rho_\infty V_\infty^2 \\
M_{e_n} &= M_e/\sqrt{\frac{\rho_\infty V}{\mu_\infty}} \\
\delta_n &= \delta/\sqrt{\frac{\rho_\infty V}{\mu_\infty}} \\
Re_{\theta_n} &= Re_\theta/\sqrt{\frac{\rho_\infty V}{\mu_\infty}}
\end{aligned} \tag{5}$$

The freestream values used in the normalization were the conditions used to define the outer boundary of the CFD solutions. The Sutherland Law<sup>23</sup> was used to approximate the viscosity ( $\mu_\infty$ ). The interpolation for these normalized parameters was performed in any one of the interpolation spaces. The normalized parameters associated with the new solution corresponding to the point of interest were then redimensionalized by multiplying by the same normalizing quantity calculated using the independent quantities (freestream conditions) at the point of interest.

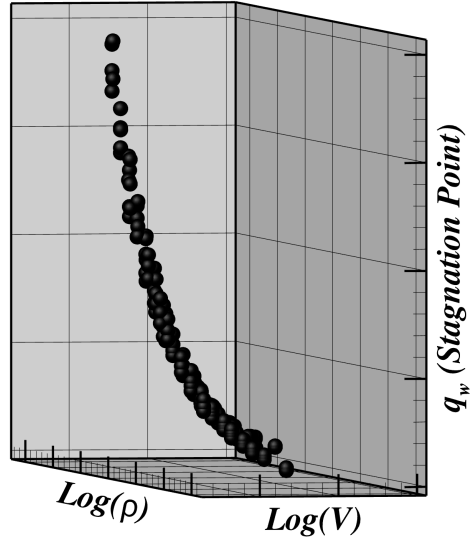


Figure 9. Stagnation point heat flux from each CFD solution plotted in  $\log \rho, \log V$  space.

$$\begin{aligned}
q_w &= q_{w_n} \times q_{ref_{poi}} \\
P_w &= P_{w_n} \times \rho_{poi} V_{poi}^2 \\
\tau_w &= \tau_{w_n} \times \rho_\infty V_\infty^2 \\
M_e &= M_{e_n} \times \sqrt{\frac{\rho_{poi} V}{\mu_{poi}}} \\
\delta &= \delta_n \times \sqrt{\frac{\rho_{poi} V}{\mu_{poi}}} \\
Re_\theta &= Re_{\theta_n} \times \sqrt{\frac{\rho_{poi} V}{\mu_{poi}}}
\end{aligned} \tag{6}$$

**Table 2.** Normalizing quantity used for each dependent parameter of interest.

Dependent Parameter	Normalizing Quantity
Pressure ( $P_w$ )	Dynamic Pressure ( $q$ )
Heat Flux ( $q_w$ )	Sutton-Graves <sup>3</sup> relation using radius of 4.694 meters
$\tau_w$	Dynamic Pressure ( $q$ )
$M_e$	$\sqrt{Re}$
$\delta$	$\sqrt{Re}$
$Re_\theta$	$\sqrt{Re}$

When comparing the quality of the interpolation spaces, it was advantageous to use a subset of the available CFD solutions to generate the interpolation spaces. As the number of individual CFD solutions used in the interpolation space increases, the error due to non-linearity of the dependent parameters within the interpolation space is reduced as the linearization between the discrete solutions better represents the true nature of the parameter. Using a subset of solutions helped accentuate the errors compared to using the full solution set and helped highlight which interpolation space performed best. In addition, by using a subset of the available solutions, the solutions left out of the interpolation space provided *truth* data for evaluating the interpolation spaces. A subset of 59 solutions was used in the generation of each of the interpolation spaces evaluated. These were the solutions at cardinal velocities (3, 4, 5, 6, 7, 8, 9, 10, 11) and the bounding altitudes at each velocity. At each of these velocity and altitude combinations, all available angles-of-attack were included in the interpolation space. Since this study used the Apollo geometry, which had a spherical heatshield, any variation in angle-of-attack was expected to simply rotate the dependent parameters on the heatshield, except at the shoulder, so including all available angles-of-attack helped to focus the evaluation on the other independent parameters. This left 126 solutions as *truth* data. Figure 10 shows the CFD solutions used to create the interpolation spaces (shown in blue) and the available *truth* data (shown in red). The specific CFD solutions included in the construction of the interpolation space correspond to the *Reduced Velocity Level 1 and Altitude* column in Appendix B.

Several approaches were used to compare and evaluate the various interpolation spaces, and each of these relied on calculating the percent difference of the dependent parameter of interest:

$$\text{Percent Difference} = \frac{p_i - p_{CFD}}{p_{CFD}} \times 100.0 \tag{7}$$

between the available CFD solutions that were not included in the interpolation space and an interpolated solution calculated by interpolating within the interpolation space at each element of the surface grid (mesh). Figure 11 shows heat flux ( $q_w$ ) from a CFD solution and the corresponding interpolated solution from the  $\log(\rho)$ ,  $\log(V)$ ,  $\alpha$  interpolation space, when interpolating for the normalized dependent parameters, along with the percent difference between the two solutions.

The maximum percent difference across all the solutions was compared as a first look to evaluate which interpolation space performed best for each dependent parameter. These maximum percent difference results

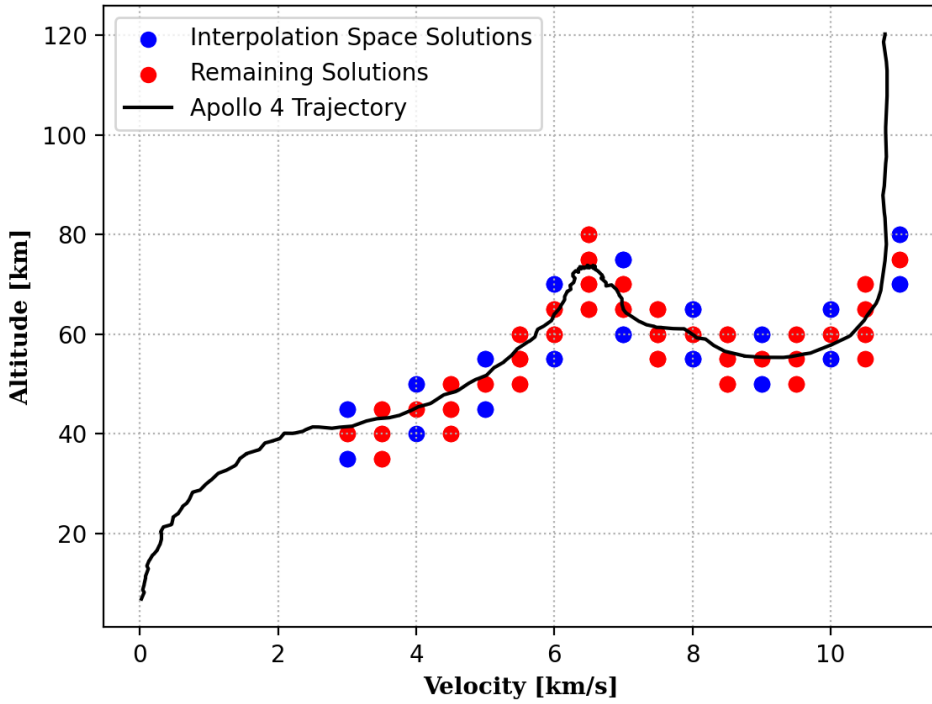


**Figure 10.** Subset of CFD solutions used in the construction of the evaluated interpolation spaces, shown in altitude versus velocity space. The blue points correspond to CFD solutions that were included in the construction of the interpolation spaces and the red correspond to CFD solutions left out of the interpolation space. The Apollo 4 trajectory is included in black.

are shown in Table 3. The heat flux ( $q_w$ ) and pressure ( $P_w$ ) had the lowest worst case percent difference when normalized and interpolated within the  $\text{Log}(\rho)$ ,  $\text{Log}(V)$ ,  $\alpha$  interpolation space before redimensionalizing. The boundary layer thickness ( $\delta$ ) had the lowest worst case percent difference when it was interpolated directly within the  $\text{Log}(\rho)$ ,  $\text{Log}(V)$ ,  $\alpha$  interpolation space. The other dependent parameters had worst case percent differences in the 10s to 100s in all the interpolation spaces. The momentum thickness Reynolds number ( $\text{Re}_\theta$ ) had percent differences in the millions. The remainder of this section provides a more in depth analysis of how well the interpolation spaces perform with each of the dependent parameters of interest ( $q_w$ ,  $P_w$ ,  $\tau_w$ ,  $M_e$ ,  $\delta$ ,  $\text{Re}_\theta$ ) and identifies which interpolation space performed best. Histograms of the percent difference in each interpolation space were also generated to understand whether the maximum represented a constant bias or a single outlier. The histograms for all dependent parameters of interest in each interpolation space have been provided in Appendix A.

The first dependent parameter of interest investigated further was heat flux ( $q_w$ ). Based on the maximum percent differences shown in Table 3, the  $\text{Log}(\rho)$ ,  $\text{Log}(V)$ ,  $\alpha$  interpolation space, with a maximum percent difference of 7.54%, performed best. The histogram of percent difference in heat flux ( $q_w$ ) for the  $\text{Log}(\rho)$ ,  $\text{Log}(V)$ ,  $\alpha$  interpolation space, shown in Figure 12, was both normally distributed and tightly clustered with a standard deviation ( $\sigma$ ) of 0.730 around a mean ( $\mu$ ) of -0.103. The low standard deviation ( $\sigma$ ) clustered near zero percent difference coupled with the lowest maximum percent difference made the  $\text{Log}(\rho)$ ,  $\text{Log}(V)$ ,  $\alpha$  interpolation space the best performing of all the interpolation space considered when interpolating for normalized heat flux ( $q_w$ ).

The distribution of worst case percent difference across the interpolation space was also considered to look for patterns. In particular, whether the error was biased to the low velocity or high velocity regimes, which might lead to different solution density requirements for each regime. Figure 13 shows the maximum percent difference of heat flux ( $q_w$ ) for each interpolated solution in the  $\text{Log}(\rho)$ ,  $\text{Log}(V)$ ,  $\alpha$  interpolation space. There were no obvious trends.

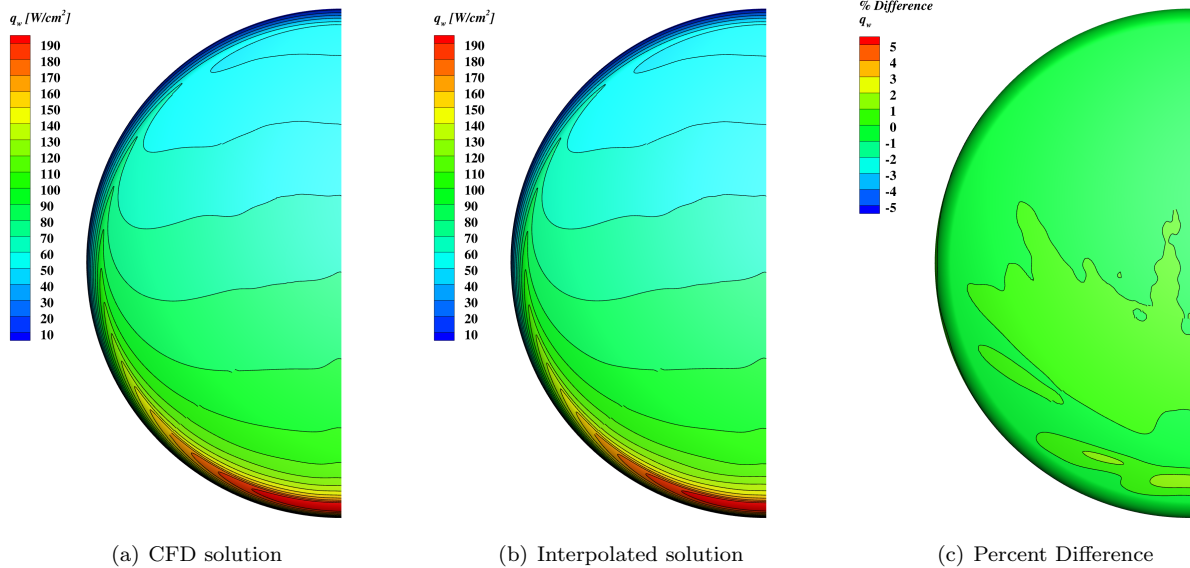


Figure 11. Comparison of the interpolated heat flux ( $q_w$ ) to the CFD solution at velocity=8.0 km/s, altitude=60.0 km, and angle-of-attack=154 degrees using the  $\text{Log}(\rho)$ ,  $\text{Log}(V)$ ,  $\alpha$  interpolation space.

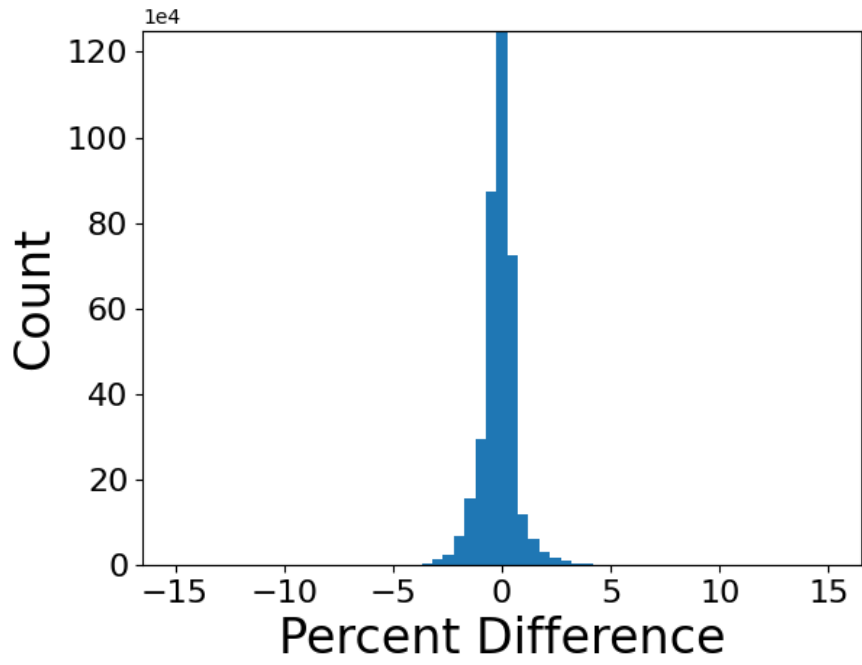


Figure 12. Histogram of the percent difference for heat flux ( $q_w$ ) in the  $\text{Log}(\rho)$ ,  $\text{Log}(V)$ ,  $\alpha$  interpolation space when interpolating for normalized heat flux ( $q_w$ ). The histograms for all the interpolation spaces are included in Appendix A.

**Table 3.** Comparison of the maximum percent difference between the interpolated solutions and the *truth* (CFD) solutions for each dependent parameter ( $q_w$ ,  $P_w$ ,  $\tau_w$ ,  $M_e$ ,  $\delta$ ,  $Re_\theta$ ).

Interpolation Space	$q_w$	$P_w$	$\tau_w$	$M_e$	$\delta$	$Re_\theta$
Direct Interpolation of Dependent Parameters						
Mach, Angle-of-Attack	296.14	1291.32	1594.56	162.51	166.42	$1.285 \times 10^9$
Mach, Dynamic Pressure, Angle-of-Attack	22.56	13.04	431.19	124.67	45.60	$8.460 \times 10^8$
$\log(\rho)$ , $\log(V)$ , Angle-of-Attack	19.62	64.36	342.34	103.18	<b>13.88</b>	$1.261 \times 10^9$
$\rho$ , Velocity <sup>2</sup> , Angle-of-Attack	-47.28	-59.58	441.26	152.37	92.61	$9.012 \times 10^8$
$\sqrt{(\rho)}$ , Velocity <sup>3</sup> , Angle-of-Attack	-26.92	-35.05	414.27	167.41	36.37	$1.010 \times 10^9$
Interpolation of Normalized Dependent Parameters						
Mach, Angle-of-Attack	35.15	47.92	1001.34	633.85	710.97	$1.045 \times 10^9$
Mach, Dynamic Pressure, Angle-of-Attack	13.20	17.55	454.11	155.06	138.09	$1.181 \times 10^9$
$\log(\rho)$ , $\log(V)$ , Angle-of-Attack	<b>7.54</b>	<b>11.81</b>	352.30	120.69	55.44	$9.227 \times 10^8$
$\rho$ , Velocity <sup>2</sup> , Angle-of-Attack	16.09	23.95	560.10	243.37	321.27	$1.412 \times 10^9$
$\sqrt{(\rho)}$ , Velocity <sup>3</sup> , Angle-of-Attack	-10.53	13.46	607.34	198.82	113.18	$1.211 \times 10^9$

The worst case percent difference occurred at 10.5 km/s and 70 km altitude at each of the angles-of-attack (152, 154, and 156), with the angle-of-attack of 154 degrees being slightly worse than than the others. Figure 14 shows the *truth* (CFD) heat flux ( $q_w$ ) distribution on the left, the heat flux ( $q_w$ ) distribution from the interpolated solution on the right, and the distribution of the percent differences in the middle, for the angle-of-attack of 154 degrees solution. The heatshield acreage had nearly zero error, except near the stagnation point, where it was off by 3% to 4%. The shoulder was where the highest percent difference of roughly 7%, was located.

The element of the interpolation space that contained the worst case percent difference point of interest was also one of the largest. The vertices of the element used to generate the interpolated solution, along with their weights, at the velocity of 10.5 km/s, altitude of 70 km, and angle-of-attack of 154 degrees point of interest are shown in Table 4. Since the point of interest was on the edge of the first entry corridor, it fell in an element that spanned the first and second entries. Figure 15 shows the interpolation space and highlights the point of interest (larger red symbol) and the contributing vertices (smaller red symbol) of the element. The contributions from the solutions at 7 and 8 km/s were likely what lead to the higher percent differences on the shoulder. By contrast, the element used for one of the lowest percent difference (1.13%) solutions at velocity of 8 km/s, altitude of 60 km, and angle-of-attack of 154 degrees, shown in Table 5, had vertices that were much closer to the point of interest. This point and the contributing vertices of the bounding element have been highlighted in green in Figure 15. Only two vertices were used because the weights of the other two vertices were zero, as was the case for the fourth vertex in the worst case example. This shows that the interpolation quality can be impacted by the size or skewness of the bounding element.

**Table 4.** Point of interest and element vertices for the worst case percent difference in the  $\log(\rho)$ ,  $\log(V)$ ,  $\alpha$  interpolation space.

Point	Velocity (km/s)	Altitude (km)	Angle-of-Attack (deg.)	Weight
Point of Interest	10.5	70.0	154.0	-
Vertex 1	11.0	70.0	154.0	0.878
Vertex 2	7.0	75.0	154.0	0.058
Vertex 3	8.0	65.0	154.0	0.064

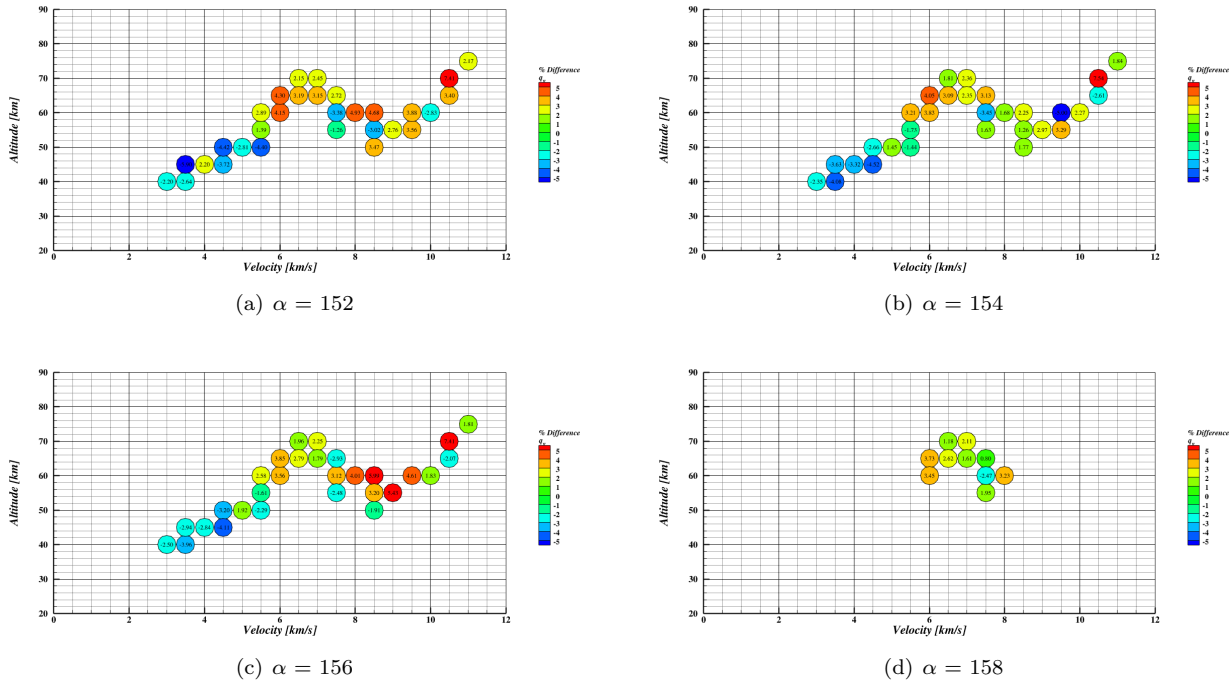


Figure 13. Worst case (maximum) percent difference for heat flux ( $q_w$ ) at each interpolated solution using the  $\text{Log}(\rho)$ ,  $\text{Log}(V)$ ,  $\alpha$  interpolation space.

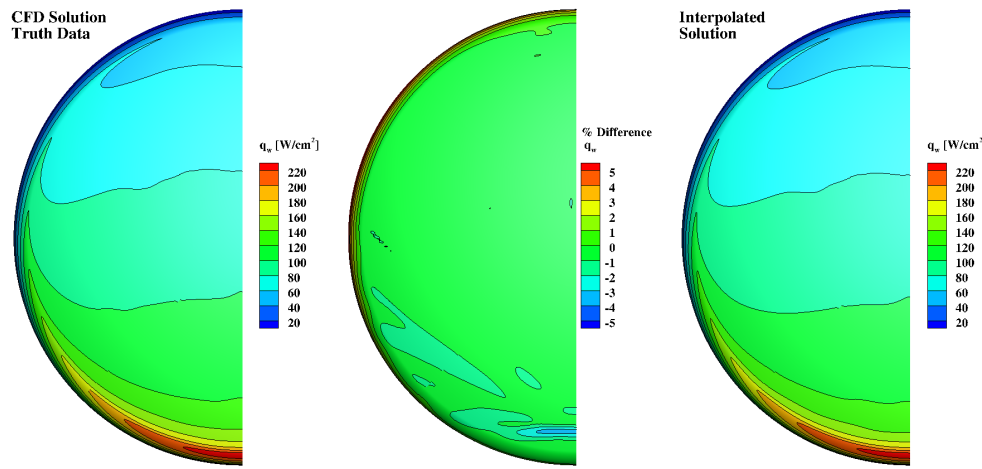
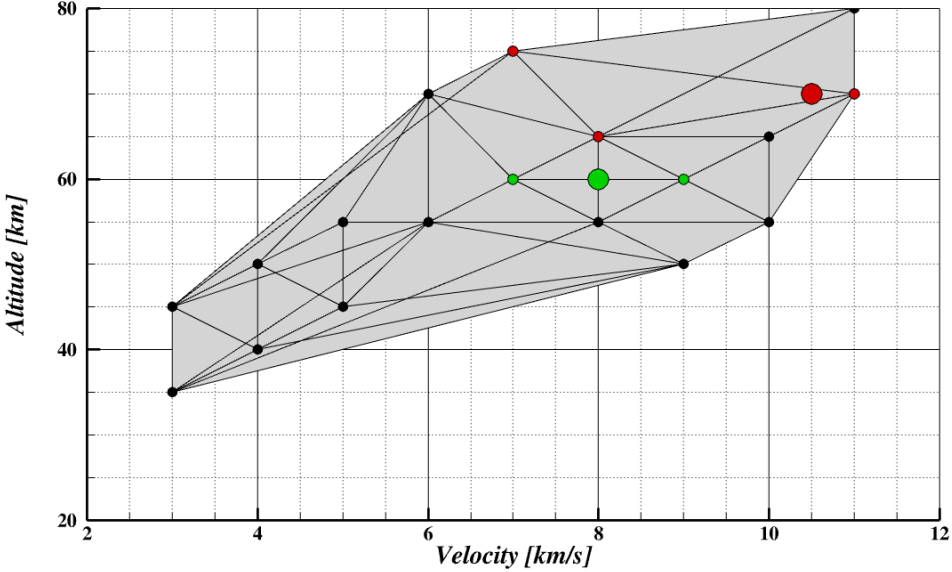


Figure 14. Comparison of the interpolated heat flux ( $q_w$ ) to the CFD solution at velocity=10.5 km/s, altitude=70.0 km, angle-of-attack=154 degrees using the  $\text{Log}(\rho)$ ,  $\text{Log}(V)$ ,  $\alpha$  interpolation space.



**Figure 15.** Slice through the Delaunay triangulated interpolation space. The vertices are displayed as black symbols. The point of interest at velocity of 10.5 km/s, altitude of 70 km, and angle-of-attack of 154 degrees (poor agreement) is displayed as a large red symbol. The vertices of the element containing that point are displayed as smaller red symbols. The point of interest at velocity of 8 km/s, altitude of 60 km, and angle-of-attack of 154 degrees (excellent agreement) is displayed as a large green symbol and the vertices of the element containing it are displayed as smaller green symbols.

**Table 5.** Point of interest and element vertices for one of the lowest percent difference solutions in the  $\text{Log}(\rho)$ ,  $\text{Log}(V)$ ,  $\alpha$  interpolation space.

Point	Velocity (km/s)	Altitude (km)	Angle-of-Attack (deg.)	Weight
Point of Interest	8.0	60.0	154.0	-
Vertex 1	7.0	60.0	154.0	0.47
Vertex 2	9.0	60.0	154.0	0.53

The same approach was used to further investigate the performance of each interpolation space for pressure ( $P_w$ ). Similar to heat flux ( $q_w$ ), the  $\text{Log}(\rho)$ ,  $\text{Log}(V)$ ,  $\alpha$  interpolation space was the best performing interpolation space. The corresponding mean ( $\mu$ ) and standard deviation ( $\sigma$ ) were 0.196 and 0.720 respectively.

The shear stress ( $\tau_w$ ) had maximum percent differences greater than 300% in all of the interpolation spaces, shown in Table 3. The  $\text{Log}(\rho)$ ,  $\text{Log}(V)$ ,  $\alpha$  interpolation space, when interpolating for shear stress ( $\tau_w$ ) directly or for normalized shear stress ( $\tau_w$ ), had similar maximum percent differences of roughly 350%, which were better than the other interpolation spaces evaluated. The solution with the maximum percent difference in the  $\text{Log}(\rho)$ ,  $\text{Log}(V)$ ,  $\alpha$  interpolation space, when interpolating for normalized shear stress ( $\tau_w$ ), was at velocity of 3.5 km/s, altitude of 40 km, and angle-of-attack of 152.0 degrees. At this point of interest, the percent difference across much of the heatshield was within 10%, but near the stagnation point, where the shear stress ( $\tau_w$ ) was small and less critical from a TPS capability perspective, the percent difference was larger, as shown in Figure 16.

Despite the majority of the heatshield agreeing within 10% at the worst case point of interest, none of the histograms were normally distributed, as can be seen in Appendix A. The  $\text{Log}(\rho)$ ,  $\text{Log}(V)$ ,  $\alpha$  interpolation space, when interpolating for shear stress ( $\tau_w$ ) directly or for normalized shear stress ( $\tau_w$ ), were skewed positive and the  $\sqrt{\rho}$ ,  $V^3$ ,  $\alpha$  interpolation space was skewed negative. These results suggested that either

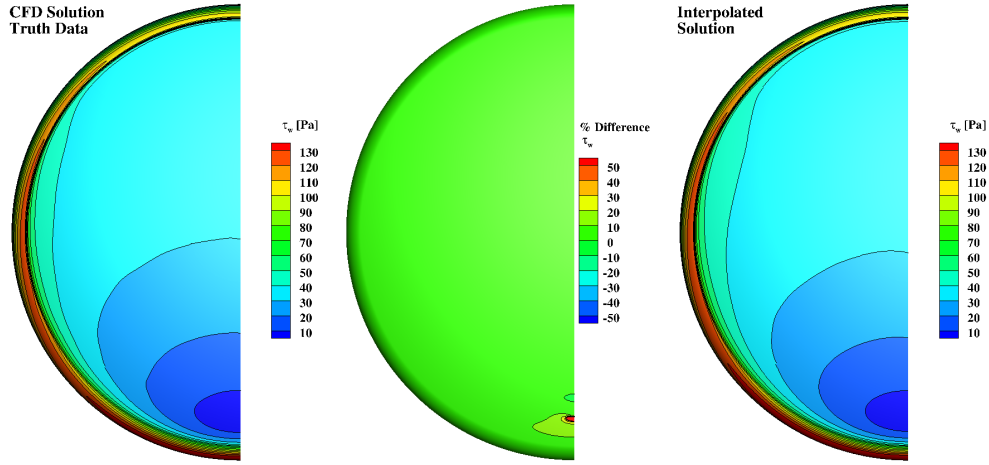


**Figure 16.** Comparison of the interpolated shear stress ( $\tau_w$ ) to the CFD solution at velocity=3.5 km/s, altitude=40.0 km, angle-of-attack=152 degrees using the  $\text{Log}(\rho)$ ,  $\text{Log}(V)$ ,  $\alpha$  interpolation space.

1) the resolution of solutions was inadequate for shear stress ( $\tau_w$ ), or 2) the interpolation spaces considered do not correlate the shear stress ( $\tau_w$ ) well. The  $\text{Log}(\rho)$ ,  $\text{Log}(V)$ ,  $\alpha$  interpolation space, when interpolating for normalized shear stress ( $\tau_w$ ) had a mean ( $\mu$ ) closer to zero than when interpolating for shear stress ( $\tau_w$ ) directly, shown in Table 6. The  $\text{Log}(\rho)$ ,  $\text{Log}(V)$ ,  $\alpha$  interpolation space also had a lower maximum percent difference than the  $\sqrt{\rho}$ ,  $V^3$ ,  $\alpha$  interpolation space. Based on these metrics, the  $\text{Log}(\rho)$ ,  $\text{Log}(V)$ ,  $\alpha$  interpolation space, when interpolating for normalized shear stress ( $\tau_w$ ), was considered the best performing of the interpolation spaces considered, but additional interpolation spaces should be considered in future work along with determining if the error can be isolated to regions that are not critical.

**Table 6.** Mean and standard deviation of the distribution of percent difference when interpolating for shear stress ( $\tau_w$ ) within each of the best performing interpolation spaces.

Interpolation Space	Mean	Standard Deviation
Direct Interpolation of Dependent Parameters		
$\text{Log}(\rho)$ , $\text{Log}(V)$ , Angle-of-Attack	5.848	3.477
$\sqrt{(\rho)}$ , Velocity <sup>3</sup> , Angle-of-Attack	-2.727	5.548
Interpolation of Normalized Dependent Parameters		
$\text{Log}(\rho)$ , $\text{Log}(V)$ , Angle-of-Attack	4.462	3.949

Similar to shear stress ( $\tau_w$ ), the edge Mach number ( $M_e$ ) had maximum percent differences greater than 100% in all of the interpolation spaces, shown in Table 3. Also similar to shear stress ( $\tau_w$ ), the largest percent differences were located near the stagnation point. This can be seen for the worst case percent difference point of interest in Figure 17, which compares the interpolated solution and the *truth* (CFD) solution. It can also be seen for the entire flight space in Figure 18, which shows the location of percent difference values greater than 20% from all points of interest. When using edge Mach number ( $M_e$ ) with momentum thickness Reynolds number ( $Re_\theta$ ) as a boundary layer transition indicator these errors would be inconsequential.

The edge Mach number ( $M_e$ ) was unique in that the distribution of percent difference was normally distributed in the  $\text{Log}(\rho)$ ,  $\text{Log}(V)$ ,  $\alpha$  interpolation space when interpolating for edge Mach number ( $M_e$ ) *directly*. The corresponding mean ( $\mu$ ) and standard deviation ( $\sigma$ ) were 0.124 and 0.795. These metrics showed that the worst case percent difference was an extreme outlier in the  $\text{Log}(\rho)$ ,  $\text{Log}(V)$ ,  $\alpha$  interpolation space, but that in general the interpolation space performed well.

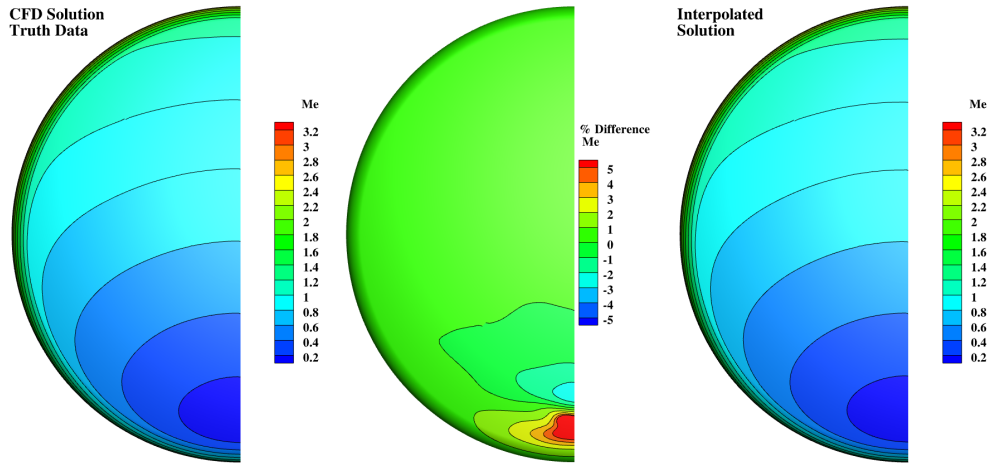


Figure 17. Comparison of the interpolated edge Mach number ( $M_e$ ) to the CFD solution at velocity=3.5 km/s, altitude=40.0 km, angle-of-attack=152 degrees using the  $\text{Log}(\rho)$ ,  $\text{Log}(V)$ ,  $\alpha$  interpolation space.

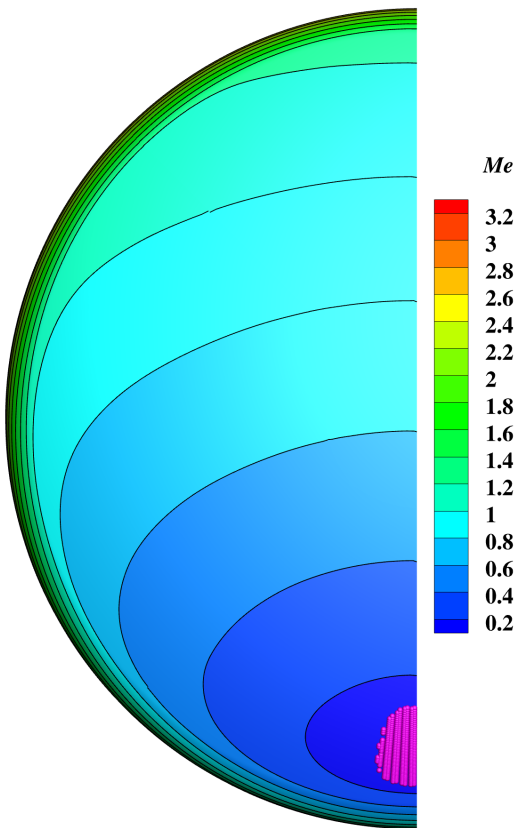
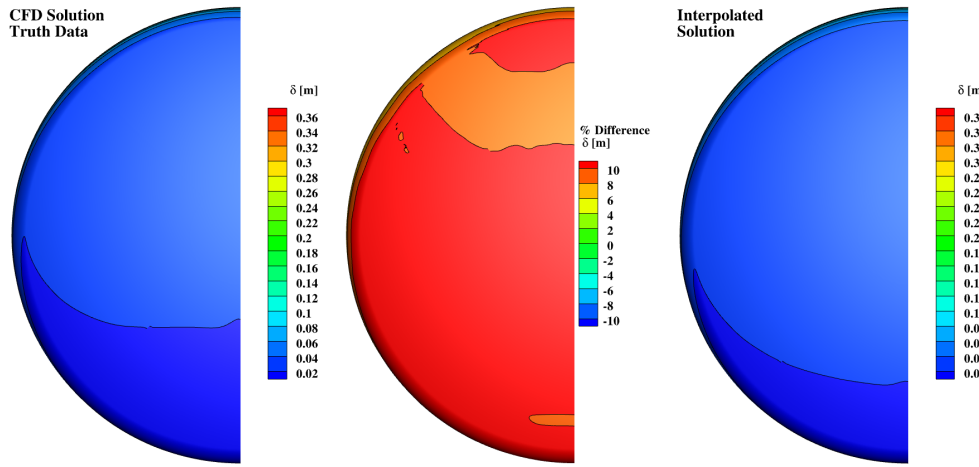


Figure 18. The location of edge Mach number ( $M_e$ ) percent difference values greater than 20% for all interpolated solutions in the  $\text{Log}(\rho)$ ,  $\text{Log}(V)$ ,  $\alpha$  interpolation space in magenta. Contours of edge Mach number ( $M_e$ ) at velocity=3.5 km/s, altitude=40.0 km, angle-of-attack=152 degrees included for reference.

The boundary layer thickness ( $\delta$ ) results were similar to shear stress ( $\tau_w$ ) in that the worst case percent difference was in the hundreds for some interpolation spaces and the distributions were not normal. Additionally, at the worst case percent difference point of interest in the  $\text{Log}(\rho)$ ,  $\text{Log}(V)$ ,  $\alpha$  interpolation space, the error was not isolated to the stagnation region, but instead was distributed across the entire heatshield, shown in Figure 19. The  $\text{Log}(\rho)$ ,  $\text{Log}(V)$ ,  $\alpha$  interpolation space, when interpolating directly for boundary layer thickness ( $\delta$ ), had a distribution that was skewed positive, but the worst case percent difference was only 13.9%, making it the best of the interpolation spaces considered. Since the disagreement in boundary layer thickness ( $\delta$ ) can be significant throughout the flight space and across the heatshield, appropriate uncertainties should be included when using this approach for estimating boundary layer thickness ( $\delta$ ) in design.



**Figure 19.** Comparison of the interpolated boundary layer thickness ( $\delta$ ) to the CFD solution at velocity=6.0 km/s, altitude=60.0 km, angle-of-attack=154 degrees using the  $\text{Log}(\rho)$ ,  $\text{Log}(V)$ ,  $\alpha$  interpolation space. This was the case with the maximum percent difference when interpolating for boundary layer thickness ( $\delta$ ) directly.

The maximum percent difference for momentum thickness Reynolds number ( $\text{Re}_\theta$ ) was extremely high, in the millions of percent difference, in each interpolation space, as seen in Table 3. The location of all the percent differences greater than 20% were plotted on the heatshield to help determine the source of these extreme values, shown in Figure 20. All of the points were located on the leeside shoulder and the stagnation region, which made them inconsequential to design when using momentum thickness Reynolds number ( $\text{Re}_\theta$ ) only as a transition indicator. Transition requires some running length and therefore occurs downstream of the stagnation region, which makes the error in that region inconsequential. A slice through the pitch plane shows that the momentum thickness Reynolds number ( $\text{Re}_\theta$ ) value has decayed considerably (less than half) from the peak where the error at the shoulder is high, shown in Figure 21, which makes this region inconsequential as well. To avoid skewing the statistics with the extremely high percent difference values, these inconsequential values were removed when calculating the mean ( $\mu$ ) and standard deviation ( $\sigma$ ). With the extreme values of momentum thickness Reynolds number ( $\text{Re}_\theta$ ) at the shoulder and the stagnation region removed, the  $\text{Log}(\rho)$ ,  $\text{Log}(V)$ ,  $\alpha$  interpolation space when interpolating for normalized momentum thickness Reynolds number ( $\text{Re}_\theta$ ) performed better than the other interpolation spaces considered. The resulting distribution was centered near zero with a mean ( $\mu$ ) of 0.071 and standard deviation ( $\sigma$ ) of 7.191.

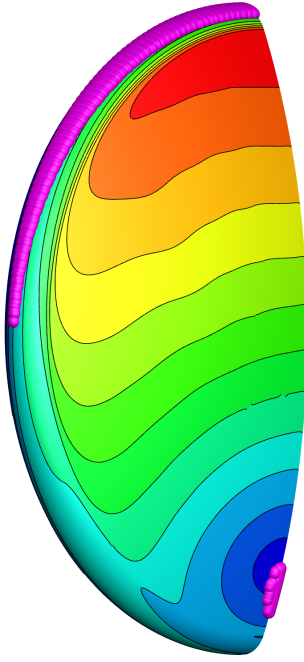


Figure 20. The location of percent differences in momentum thickness Reynolds number ( $Re_\theta$ ) greater than 20% are shown in magenta and were clustered on the leeside shoulder and stagnation region. The contours are momentum thickness Reynolds number ( $Re_\theta$ ).

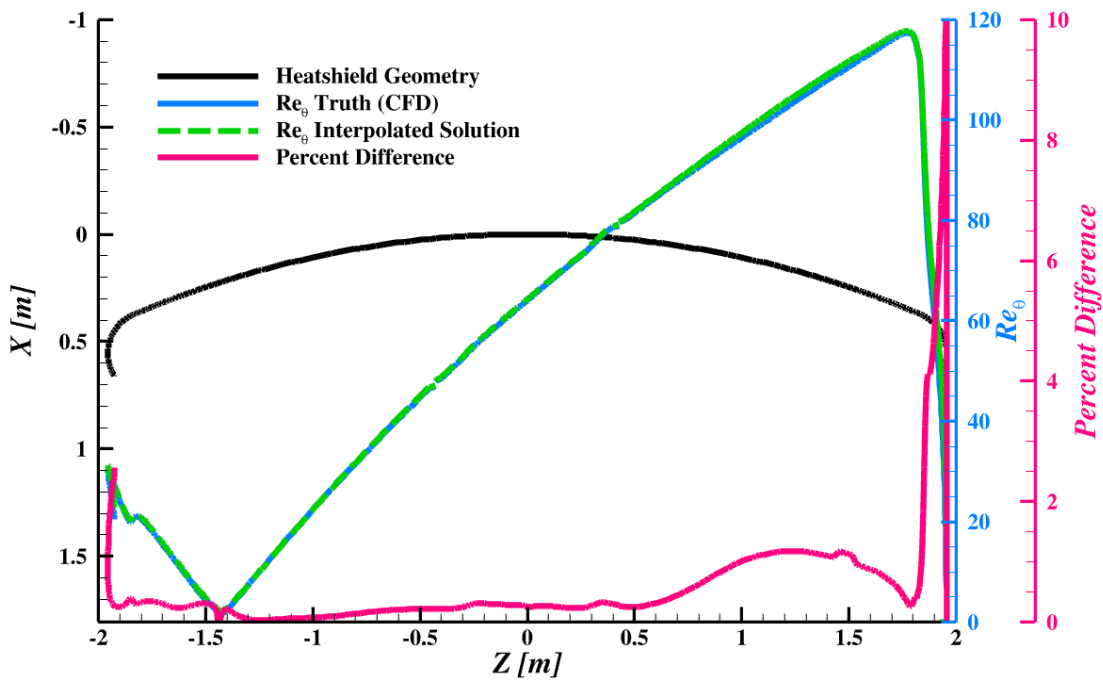


Figure 21. Comparison of the interpolated momentum thickness Reynolds number ( $Re_\theta$ ) to the CFD solution along the the pitch plane at velocity=6.0 km/s, altitude=65.0 km, angle-of-attack=158 degrees using the  $\log(\rho)$ ,  $\log(V)$ ,  $\alpha$  interpolation space.

In summary, the  $\text{Log}(\rho)$ ,  $\text{Log}(V)$ ,  $\alpha$  interpolation space performed better than the other interpolation spaces for all of the dependent parameters of interest except for shear stress ( $\tau_w$ ). The heat flux ( $q_w$ ), pressure ( $P_w$ ), and momentum thickness Reynolds number ( $Re_\theta$ ) performed best when interpolating the normalized values and then redimensionalizing at the point of interest. The edge Mach number ( $M_e$ ) and boundary layer thickness ( $\delta$ ) performed best when interpolated directly. Shear stress ( $\sigma$ ) had three interpolation spaces that performed similarly, including the  $\text{Log}(\rho)$ ,  $\text{Log}(V)$ ,  $\alpha$  interpolation space. Given the  $\text{Log}(\rho)$ ,  $\text{Log}(V)$ ,  $\alpha$  interpolation space was the best performing interpolation space for all the other parameters of interest, it is recommended that shear stress ( $\tau_w$ ) be estimated using  $\text{Log}(\rho)$ ,  $\text{Log}(V)$ ,  $\alpha$  interpolation space as well. Table 7 summarizes these details for each dependent parameter of interest along with the corresponding mean ( $\mu$ ) and standard deviation ( $\sigma$ ) of the percent difference between the interpolated solutions and *truth* (CFD) solutions.

**Table 7. Interpolation spaces that performed best for each dependent parameter of interest ( $q_w$ ,  $P_w$ ,  $\tau_w$ ,  $M_e$ ,  $\delta$ ,  $Re_\theta$ ), along with the corresponding mean ( $\mu$ ) and standard deviation ( $\sigma$ ).**

Dependent Parameter	Interpolation Space	Approach	Mean	Standard Deviation
Heat Flux ( $q_w$ )	$\text{Log}(\rho)$ , $\text{Log}(V)$ , $\alpha$	normalized	-0.103	0.730
Pressure ( $P_w$ )	$\text{Log}(\rho)$ , $\text{Log}(V)$ , $\alpha$	normalized	0.196	0.720
Shear Stress ( $\tau_w$ )	$\text{Log}(\rho)$ , $\text{Log}(V)$ , $\alpha$	normalized	4.462	3.949
Edge Mach Number ( $M_e$ )	$\text{Log}(\rho)$ , $\text{Log}(V)$ , $\alpha$	direct	0.124	0.795
Boundary Layer Thickness ( $\delta$ )	$\text{Log}(\rho)$ , $\text{Log}(V)$ , $\alpha$	direct	3.659	3.182
Momentum Thickness Reynolds Number ( $Re_\theta$ )	$\text{Log}(\rho)$ , $\text{Log}(V)$ , $\alpha$	normalized	0.071	7.191

## B. Interpolation Accuracy Dependence on Interpolation Space Resolution

The previous section identified the interpolation space that performed best for each of the dependent parameters of interest; this was done using interpolation spaces that were relatively sparse. Using a sparse interpolation space was done intentionally to exacerbate any error due to non-linearity of the dependent parameters in the interpolation spaces. This section explores how the interpolation error changes with solution resolution using the best performing interpolation spaces identified in the previous section. Since the best performing interpolation space for each dependent parameter of interest used density ( $\rho$ ), velocity ( $V$ ), and angle-of-attack, the performance of the interpolation spaces identified in the previous section have been evaluated as the resolution of solutions in each of these dimensions was progressively reduced.

CFD solutions along the Apollo 4 trajectory have been used as *truth* data for this evaluation. The location of these solutions are shown in Figure 22, and the conditions are specified in Table 8. In the previous section, the CFD solutions not included in the construction of the interpolation space were used as *truth* data. In this study, the performance of a given interpolation space was evaluated as the number of CFD solutions used to construct the interpolation space was reduced. The performance of the given interpolation space when using the full database (185) of CFD solutions was considered the benchmark.

To evaluate how the interpolation performance changes with reduced resolution in each dimension (independent parameter), a series of solution (CFD) subsets were considered. Two levels of reduced resolution were considered in velocity, removing every other velocity that gets included with each level, shown in Figure 23. The first level left out solutions at velocities of 3.5, 4.5, 5.5, 6.5, 7.5, 8.5, 9.5, and 10.5 km/s, and included those at 3, 4, 5, 6, 7, 8, 9, 10, and 11 km/s. The second level left out the solutions at velocities of 3.5, 4.0, 4.5, 5.5, 6.0, 6.5, 7.5, 8.0, 8.5, 9.5, 10.0, and 10.5 km/s, and included those at 3, 5, 7, 9, and 11 km/s. In both cases, all altitudes and all angles-of-attack available were included at each included velocity. The altitude and angle-of-attack dimensions were each reduced by retaining only the minimum and maximum available solutions at each velocity. Figure 24 shows the solutions that were included for the reduced altitude resolution subset. Again, all available velocity and angles-of-attack were included at each remaining altitude. Figure 25 shows the solutions that were included for the reduced angle-of-attack resolution subset, along with the full angle-of-attack resolution set for reference. Finally, two combined velocity and altitude reduced resolution subsets were also evaluated. These combined the two levels of velocity reduction with the altitude

**Table 8. Apollo 4 CFD solution conditions.**

Velocity [km/s]	Altitude [km]	Angle-of-Attack [deg.]
3.0	41.19	153.5
4.0	45.97	154.0
5.0	51.23	153.2
6.0	63.36	153.7
7.1	63.11	156.0
8.0	59.42	156.7
8.5	57.48	157.0
9.5	55.22	154.9
9.91	56.69	154.6
10.65	65.27	155.0
10.65	67.85	155.0
10.8	76.93	154.8

reduction. Figure 26 shows the solutions that were included for each of these combined subsets. In both of these combined cases, all available angles-of-attack were included. Table 9 provides the solution count associated with each reduced resolution subset and Appendix B shows the subset of CFD solutions used to construct each resolution of the interpolation spaces.

**Table 9. Reduced resolution subset solution counts.**

Subset	Count
Full	185
Velocity Level 1 Reduction	97
Velocity Level 2 Reduction	52
Altitude Reduction	113
Angle-of-Attack Reduction	106
Combined Velocity Level 1, Altitude	59
Combined Velocity Level 2, Altitude	32

Similar to the previous section, the distribution of percent difference along with the corresponding mean ( $\mu$ ) and standard deviation ( $\sigma$ ) were used as metrics for evaluating the impact that reducing the resolution in a given dimension had on performance for each parameter of interest. Appendix C shows the histograms for each parameter of interest using each subset of CFD solutions (resolution) to construct the interpolation space concluded to be the best performing in the previous section. These histograms are arranged by the dimension(s) being reduced: 1) velocity, 2) altitude, 3) angle-of-attack, and 4) combined velocity and altitude. Each of these have two figures. The first set of histograms shows the surface parameters: heat flux ( $q_w$ ), pressure ( $P_w$ ), and shear stress ( $\tau_w$ ). The second set of histograms shows the boundary layer parameters: edge Mach number ( $M_e$ ), boundary layer thickness ( $\delta$ ), and momentum thickness Reynolds number ( $Re_\theta$ ). Each row of histograms shows the histogram for the parameter of interest using the full set of CFD solutions followed by the histogram(s) with each level of reduced resolution.

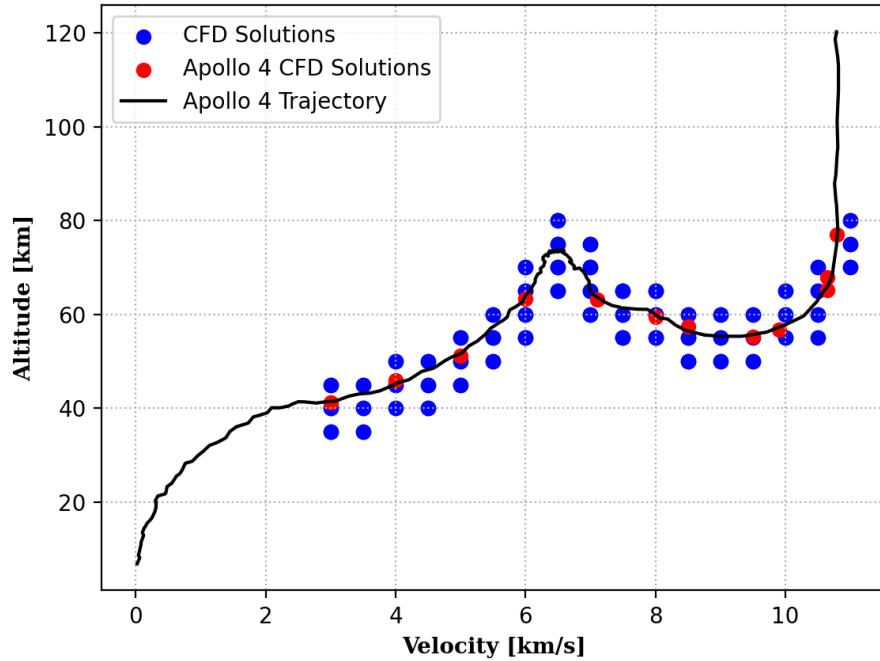


Figure 22. Apollo 4 CFD solutions in altitude as a function of velocity shown in red. The Apollo 4 trajectory is included in black. The database of CFD solutions used to develop interpolation spaces are shown in blue.

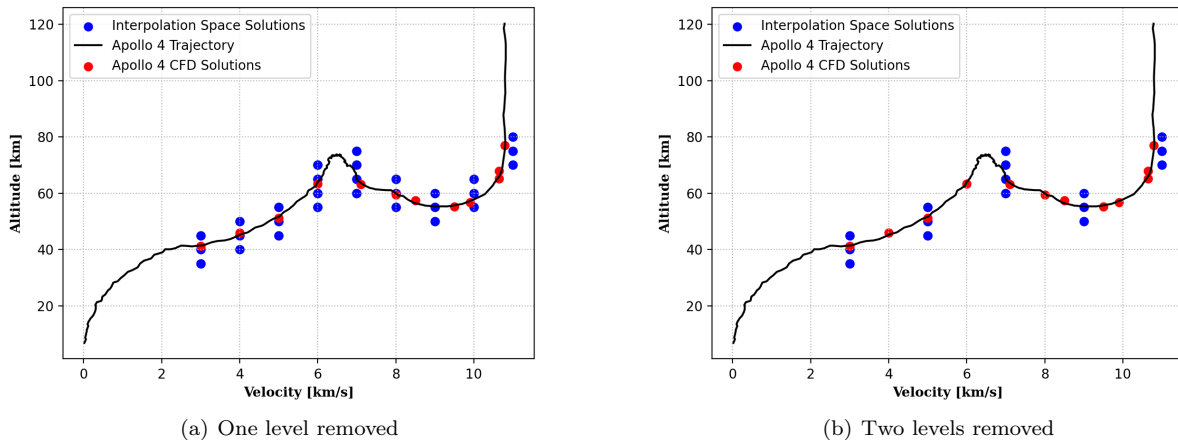
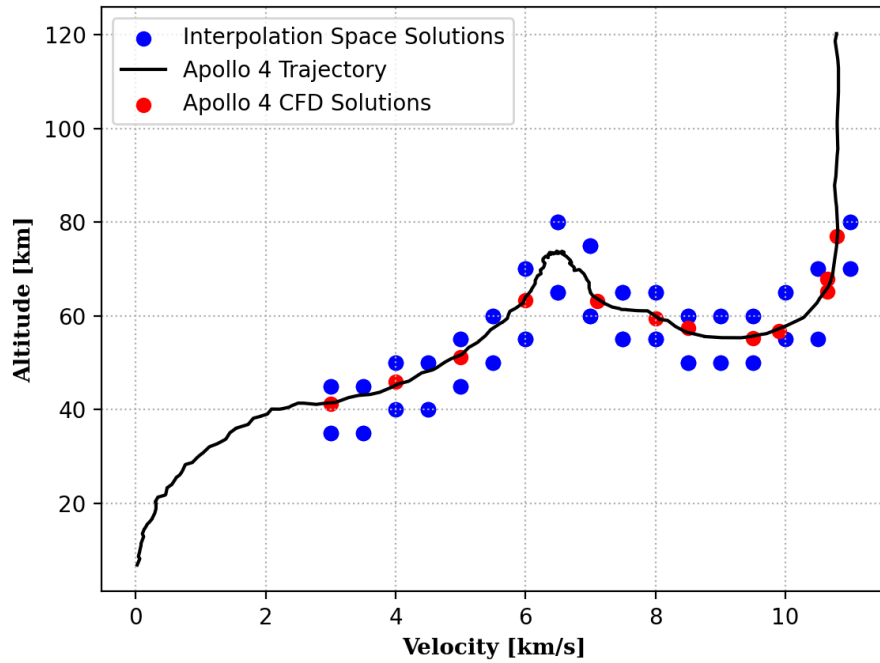
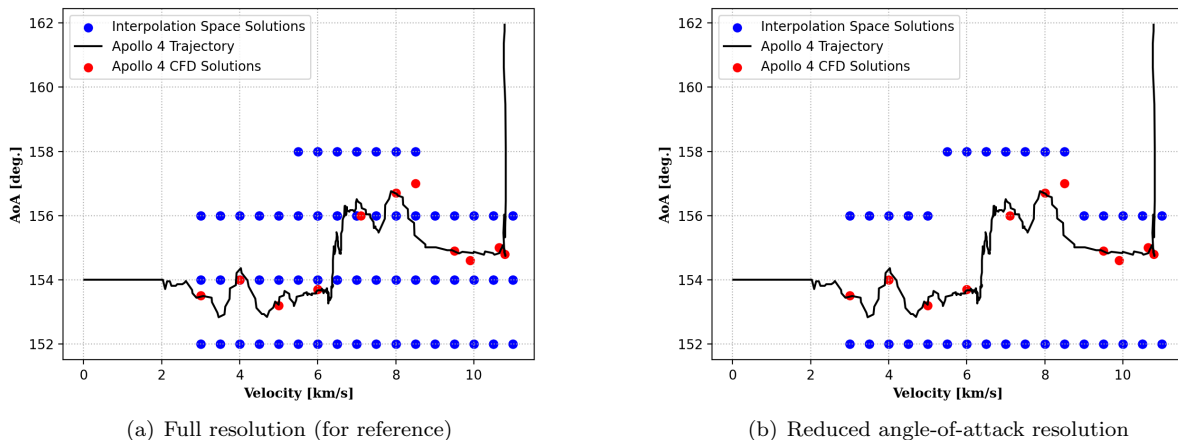


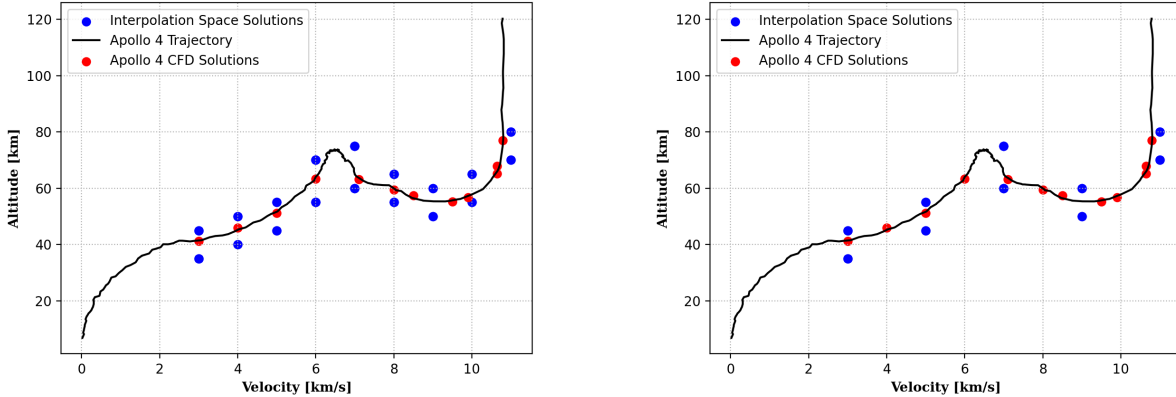
Figure 23. Solutions (CFD) included in the construction of the interpolation spaces when reducing the solution resolution in the velocity dimension.



**Figure 24.** Solutions (CFD) included in the construction of the interpolation spaces when reducing the solution resolution in the altitude dimension.



**Figure 25.** Solutions (CFD) included in the construction of the interpolation spaces when reducing the solution resolution in the angle-of-attack dimension.



(a) One level velocity combined with altitude reduction

(b) Two levels of velocity combined with altitude reduction

**Figure 26.** Solutions (CFD) included in the construction of the interpolation spaces when reducing the solution resolution in the both the velocity and altitude dimensions.

Heat flux ( $q_w$ ), pressure ( $P_w$ ), and edge Mach number ( $M_e$ ) saw limited degradation even after reducing the velocity resolution by two levels, as shown by the consistent mean ( $\mu$ ) and standard deviation ( $\sigma$ ) in Table 10. The boundary layer thickness ( $\delta$ ) saw minor degradation with each level of velocity resolution reduction; momentum thickness Reynolds number ( $Re_\theta$ ) had similar bias at each level, but the standard deviation roughly doubled. Shear stress ( $\tau_w$ ) saw a growing bias and an increase in the standard deviation ( $\sigma$ ) with each level of velocity resolution reduction. A second cluster can be seen in the histograms around 10% as the velocity resolution was reduced, shown in Figure 27. All of the solutions had near zero percent difference except at the heatshield to shoulder interface, shown in Figure 28, except for two solutions which saw elevated percent differences across the heatshield. These solutions likely drove the bias growth. Better understanding of the specific cause for the poor agreement at these two solutions has been identified for future work.

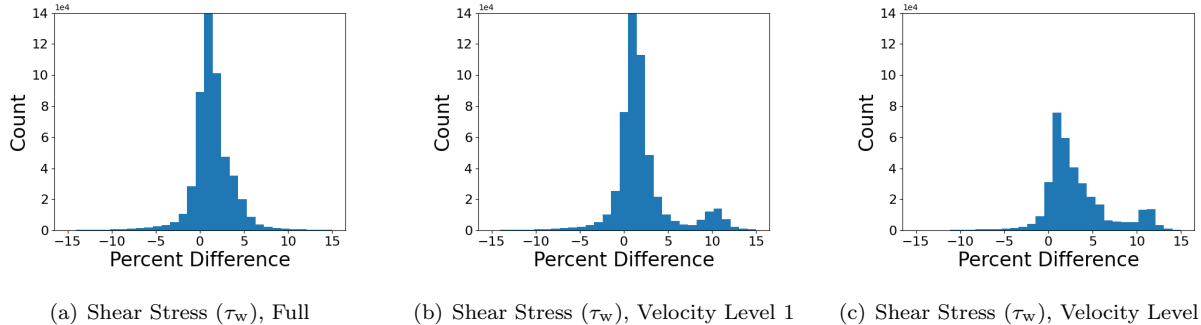
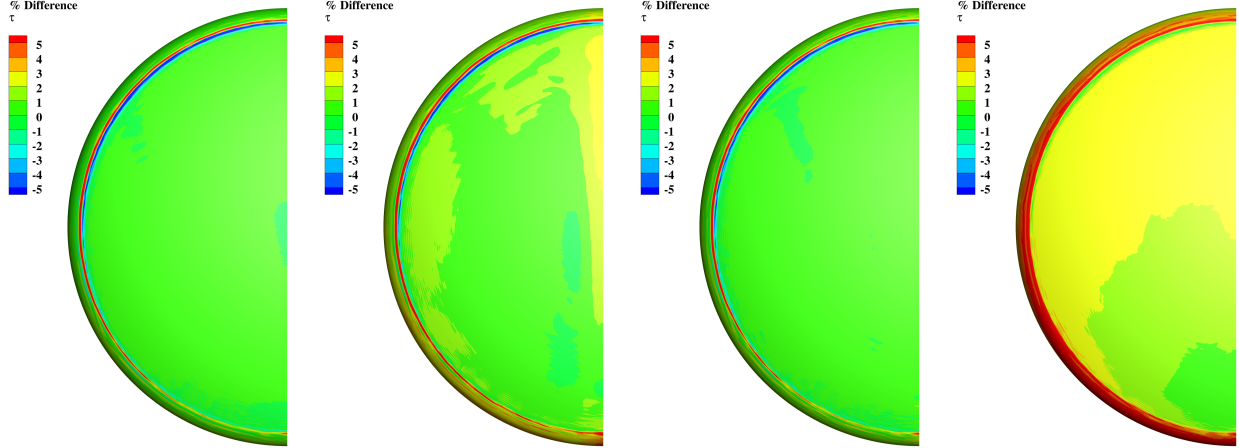


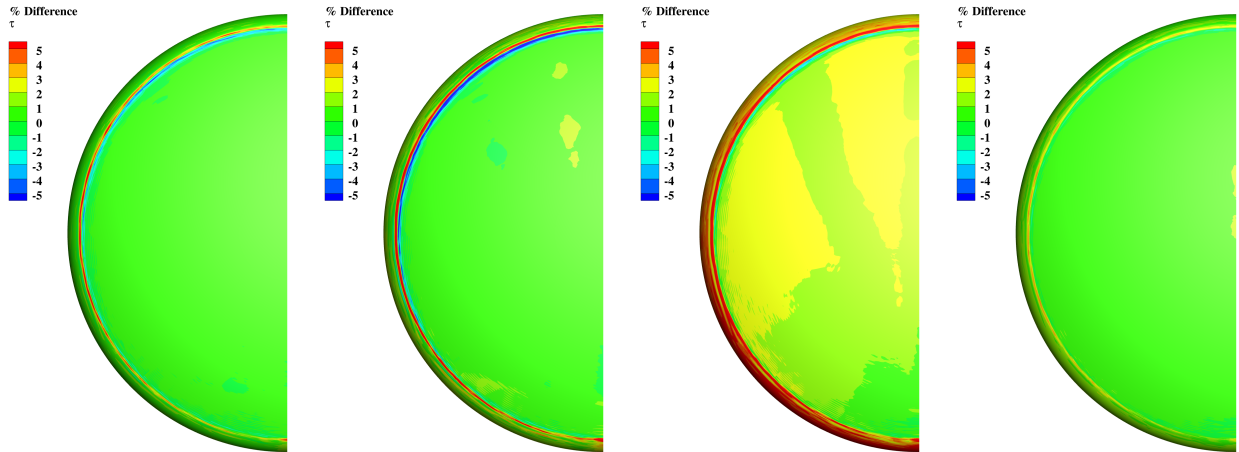
**Figure 27.** Comparison of the histograms of percent difference in shear stress ( $\tau_w$ ) for all surface elements from the Apollo 4 solutions with reduced resolution in the velocity dimension.

Heat flux ( $q_w$ ), pressure ( $P_w$ ), and edge Mach number ( $M_e$ ) were relatively insensitive to the reduction in altitude (density) resolution, as shown by the consistent mean ( $\mu$ ) and standard deviation ( $\sigma$ ) in Table 11. The momentum thickness Reynolds number ( $Re_\theta$ ) saw minor degradation. The shear stress ( $\tau_w$ ) and boundary layer thickness ( $\delta$ ) saw an increase in bias, roughly double, as well as an increase in the standard deviation ( $\sigma$ ), which was also evident by the spread in the histograms in Appendix C.

Reduced resolution in angle-of-attack had limited impact on the heat flux ( $q_w$ ) or pressure ( $P_w$ ), based on the consistent mean ( $\mu$ ) and standard deviation ( $\sigma$ ) in Table 12. The edge Mach number ( $M_e$ ), boundary layer thickness ( $\delta$ ), and momentum thickness Reynolds number ( $Re_\theta$ ) saw minor growth in standard deviation



(a)  $V = 3.0 \text{ km/s}$ , Alt. = 41.19 km, AoA = 153.5 deg. (b)  $V = 4.0 \text{ km/s}$ , Alt. = 45.97 km, AoA = 154.0 deg. (c)  $V = 5.0 \text{ km/s}$ , Alt. = 51.23 km, AoA = 153.2 deg. (d)  $V = 6.0 \text{ km/s}$ , Alt. = 63.36 km, AoA = 153.7 deg.



(e)  $V = 7.1 \text{ km/s}$ , Alt. = 63.11 km, AoA = 156.0 deg. (f)  $V = 8.0 \text{ km/s}$ , Alt. = 59.42 km, AoA = 156.7 deg. (g)  $V = 10.6 \text{ km/s}$ , Alt. = 67.85 km, AoA = 155.0 deg. (h)  $V = 10.8 \text{ km/s}$ , Alt. = 76.93 km, AoA = 154.8 deg.

**Figure 28.** Percent difference in shear stress ( $\tau_w$ ) between the interpolated solutions using the level two velocity resolution reduction and the *truth* (CFD) solutions at each of the Apollo 4 cases that were contained by interpolation space.

**Table 10.** Mean and standard deviation of the percent difference for each of the dependent parameters of interest ( $q_w$ ,  $P_w$ ,  $\tau_w$ ,  $M_e$ ,  $\delta$ ,  $Re_\theta$ ) with the full resolution interpolation space and both levels of reduced velocity resolution.

Subset	Full	Level 1	Level 2
mean ( $\mu$ )			
Heat Flux ( $q_w$ )	0.16	0.14	-0.19
Pressure ( $P_w$ )	0.08	0.10	0.18
Shear Stress ( $\tau_w$ )	1.41	2.04	3.24
Edge Mach Number ( $M_e$ )	0.19	0.22	0.34
Boundary Layer Thickness ( $\delta$ )	1.04	1.31	1.83
Momentum Thickness Reynolds Number ( $Re_\theta$ )	0.67	0.79	0.89
standard deviation ( $\sigma$ )			
Heat Flux ( $q_w$ )	1.49	1.51	1.73
Pressure ( $P_w$ )	1.68	1.70	1.75
Shear Stress ( $\tau_w$ )	4.28	4.91	5.27
Edge Mach Number ( $M_e$ )	1.55	1.57	1.83
Boundary Layer Thickness ( $\delta$ )	1.49	2.11	1.75
Momentum Thickness Reynolds Number ( $Re_\theta$ )	6.51	6.84	11.44

**Table 11.** Mean and standard deviation of the percent difference for each of the dependent parameters of interest ( $q_w$ ,  $P_w$ ,  $\tau_w$ ,  $M_e$ ,  $\delta$ ,  $Re_\theta$ ) with the full resolution interpolation space and the reduced altitude resolution.

Subset	Full	Reduced Altitude
mean ( $\mu$ )		
Heat Flux ( $q_w$ )	0.16	0.09
Pressure ( $P_w$ )	0.08	0.10
Shear Stress ( $\tau_w$ )	1.41	3.02
Edge Mach Number ( $M_e$ )	0.19	0.36
Boundary Layer Thickness ( $\delta$ )	1.04	2.24
Momentum Thickness Reynolds Number ( $Re_\theta$ )	0.67	0.89
standard deviation ( $\sigma$ )		
Heat Flux ( $q_w$ )	1.49	1.50
Pressure ( $P_w$ )	1.68	1.70
Shear Stress ( $\tau_w$ )	4.28	5.06
Edge Mach Number ( $M_e$ )	1.55	1.70
Boundary Layer Thickness ( $\delta$ )	1.49	2.47
Momentum Thickness Reynolds Number ( $Re_\theta$ )	6.51	6.80

( $\sigma$ ) as the histograms spread slightly. The shear stress ( $\tau_w$ ) saw the most significant impact with both the mean ( $\mu$ ) and the standard deviation ( $\sigma$ ) roughly doubling.

Reducing the resolution of solutions in both the velocity and altitude (density) dimensions had limited impact on heat flux ( $q_w$ ) and pressure ( $P_w$ ), based on the consistent mean ( $\mu$ ) and standard deviation ( $\sigma$ ) values, as seen in Table 13. The edge Mach number ( $M_e$ ) saw minor spreading of the histograms and as a result, the standard deviation ( $\sigma$ ) also increased compared to the full set. The impact to momentum thickness

**Table 12.** Mean and standard deviation of the percent difference for each of the dependent parameters of interest ( $q_w$ ,  $P_w$ ,  $\tau_w$ ,  $M_e$ ,  $\delta$ ,  $Re_\theta$ ) with the full resolution interpolation space and the reduced angle-of-attack resolution.

Subset	Full	Reduced Angle-of-Attack
mean ( $\mu$ )		
Heat Flux ( $q_w$ )	0.16	-0.07
Pressure ( $P_w$ )	0.08	0.13
Shear Stress ( $\tau_w$ )	1.41	3.58
Edge Mach Number ( $M_e$ )	0.19	0.58
Boundary Layer Thickness ( $\delta$ )	1.04	1.73
Momentum Thickness Reynolds Number ( $Re_\theta$ )	0.67	0.65
standard deviation ( $\sigma$ )		
Heat Flux ( $q_w$ )	1.49	1.69
Pressure ( $P_w$ )	1.68	1.96
Shear Stress ( $\tau_w$ )	4.28	8.85
Edge Mach Number ( $M_e$ )	1.55	3.60
Boundary Layer Thickness ( $\delta$ )	1.49	2.07
Momentum Thickness Reynolds Number ( $Re_\theta$ )	6.51	10.95

Reynolds number ( $Re_\theta$ ) was similar but more pronounced. The biggest degradation was to boundary layer thickness ( $\delta$ ) and shear stress ( $\tau_w$ ), which both developed a positive bias and significant spreading of their histograms as the solution resolution was reduced.

**Table 13.** Mean and standard deviation of the percent difference for each of the dependent parameters of interest ( $q_w$ ,  $P_w$ ,  $\tau_w$ ,  $M_e$ ,  $\delta$ ,  $Re_\theta$ ) with the full resolution interpolation space and both levels of reduced velocity resolution combined with altitude resolution reduction.

Subset	Full	Level 1	Level 2
mean ( $\mu$ )			
Heat Flux ( $q_w$ )	0.16	0.15	-0.09
Pressure ( $P_w$ )	0.08	0.18	0.37
Shear Stress ( $\tau_w$ )	1.41	4.90	8.01
Edge Mach Number ( $M_e$ )	0.19	0.40	0.68
Boundary Layer Thickness ( $\delta$ )	1.04	3.83	5.46
Momentum Thickness Reynolds Number ( $Re_\theta$ )	0.67	0.83	1.13
standard deviation ( $\sigma$ )			
Heat Flux ( $q_w$ )	1.49	1.53	1.78
Pressure ( $P_w$ )	1.68	1.78	1.86
Shear Stress ( $\tau_w$ )	4.28	5.87	8.17
Edge Mach Number ( $M_e$ )	1.55	1.73	2.07
Boundary Layer Thickness ( $\delta$ )	1.49	3.27	3.85
Momentum Thickness Reynolds Number ( $Re_\theta$ )	6.51	8.01	12.56

In summary, the dependent parameters of interest that were most sensitive to reduced solution resolution were the shear stress ( $\tau_w$ ) and boundary layer thickness ( $\delta$ ). The heat flux ( $q_w$ ) and pressure ( $P_w$ ) saw limited degradation with reduced resolution in velocity, altitude, or angle-of-attack and only saw a minor

increase with two levels of reduced velocity resolution combined with the altitude resolution reduction. The same was true for edge Mach number ( $M_e$ ) except that the standard deviation ( $\sigma$ ) did increase slightly with reduced resolution in angle-of-attack. The momentum thickness Reynolds number ( $Re_\theta$ ) saw limited degradation with one level of velocity resolution reduction, but was sensitive to the second level velocity resolution reduction and slightly sensitive to altitude (density) resolution. Angle-of-attack resolution was most impactful to shear stress ( $\tau_w$ ), boundary layer thickness ( $\delta$ ), and momentum thickness Reynolds number ( $Re_\theta$ ).

### C. Database Coverage Altitude and Velocity Spacing Recommendation for Heat Flux

Understanding CFD solution spacing is important for database coverage, where database coverage refers to having sufficient CFD resolution in the database such that the interpolated results can be trusted. When a database is first being developed, there is not enough time or resources to run CFD at every desired point in the flight space. In addition, as trajectories evolve throughout the design iteration cycle, it is not feasible to expand the database to cover every point along these new trajectories. However, it is critical to ensure the database has sufficient coverage across the desired flight space. This section investigates a method for how to assess database coverage, and provides a recommendation for altitude and velocity spacing between database points and the trajectory or trajectories (points to be interpolated to).

For this investigation, the interpolated parameter of interest is heat flux in the  $\text{Log}(\rho)$ ,  $\text{Log}(V)$ ,  $\alpha$  interpolation space as this was the interpolation space determined to minimize the overall heat flux error. The full 185 points were used for the database. A point of interest was selected from the 185 points, and that point of interest was then removed from the interpolation space. This resulted in one point to interpolate to, and 184 solutions used to construct the interpolation space. The next step in the process was to interpolate to that point of interest. Depending on where the point was located in the convex hull, up to four CFD solutions could be used for the interpolation, as each of these CFD solutions comprise the vertices of the tetrahedron in three-dimensional space. This interpolated point was then compared to the original CFD solution value that was in the original set of database points. For each iteration cycle, the heat flux percent difference was computed using the normalized approach previously discussed. Only the heatshield acreage was included in the surface elements considered for the percent difference calculations; the shoulder region was excluded. The corresponding mean and standard deviation values were also computed. In addition to percent difference in heat flux, a percent pass metric was evaluated, which was defined as the percentage of the number of points that were within  $+/- 5\%$  of the heat flux percent difference. For each tetrahedron used for the interpolation, volume and skew values were also calculated, where skew was determined using the formula:

$$Skew = \max \left[ \frac{(\theta_{max} - \theta_e)}{(180 - \theta_e)}, \frac{(\theta_e - \theta_{min})}{\theta_e} \right] \quad (8)$$

where  $\theta_{max}$  was the maximum of the largest angles in each triangle of the given tetrahedron,  $\theta_{min}$  was the smallest of the minimum angles in each triangle of the given tetrahedron, and  $\theta_e = 60^\circ$  corresponds to each angle value for an equilateral triangle.

For the next iteration cycle, the point of interest was still removed from the interpolation space, in addition to any of the CFD solutions used to compute the previous interpolation. The purpose of removing points used in the interpolation of a point of interest was to better understand when the quality of the interpolation starts to break down and what independent parameter delta values it corresponds to, where the delta value is the difference between the point of interest and each of the points of the tetrahedron. Whether or not a CFD solution was used for the interpolation was determined by looking at the weights of each of the CFD solutions used in the interpolation. If a weight value was equal to zero, that meant that the corresponding CFD solution was not used in the interpolation, thus that solution remained in the interpolation space for the next iteration cycle. Conversely, any CFD database point with a non-zero weight was removed from the interpolation space. This process was repeated for up to five iteration cycles or until the point of interest was outside the database for each of the 185 database points. The results collected were then used to inform recommended spacing values.

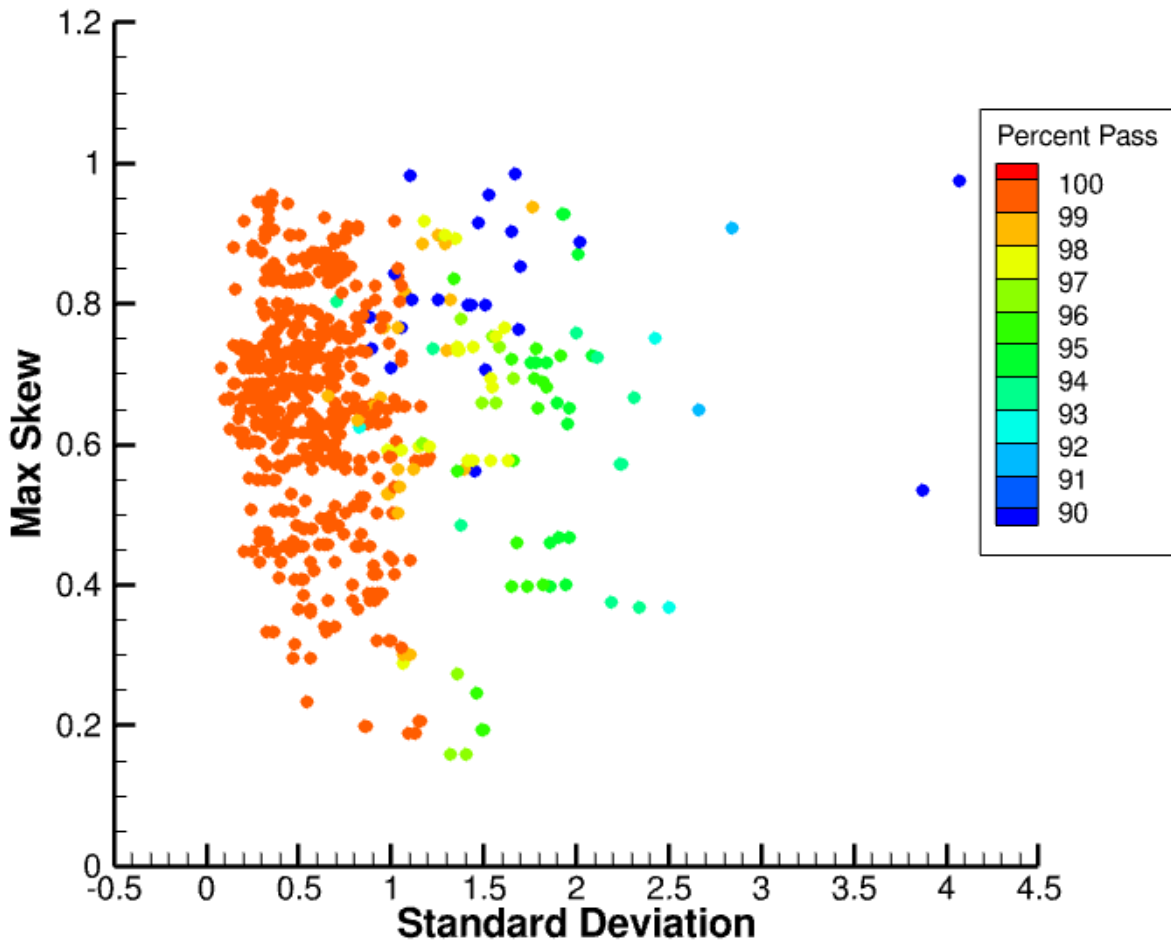


**Figure 29.** The figure shows the maximum skew value of each tetrahedron used for the interpolation versus standard deviation of the heat flux percent difference with percent pass color mapping.

As can be seen from Figure 29, smaller standard deviations of the heat flux percent difference generally correlate to higher percent pass values as would be expected. Another takeaway is that the percent pass value generally decreases as the maximum skew value for the tetrahedron increases for higher standard deviations. As most of the points with high percent pass values were within a standard deviation of 0.85, this value was used as an initial guideline to help inform recommended spacing. To determine recommended allowable delta values for altitude and velocity, only interpolated solution results that used database points that 1) were within a standard deviation of 0.85 and 2) had weight values greater than zero for the interpolation were included. The results for delta altitude and delta velocity with these criteria applied can be seen in Figure 30.

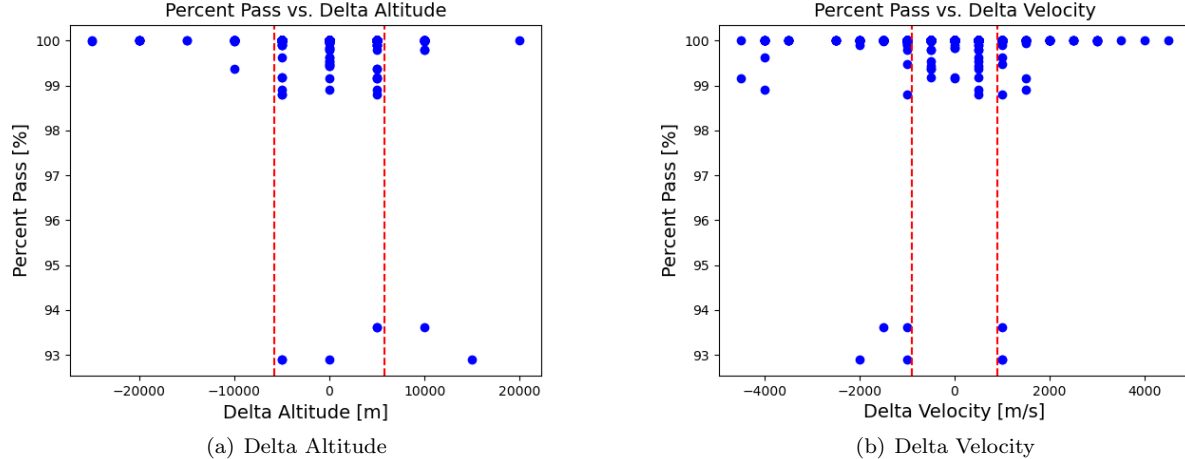


**Figure 30.** The plots show percent pass plotted versus the difference between the point of interest and the database point used in the interpolation in altitude (left) and velocity (right).

Delta altitude represents the difference between the point of interest altitude and the database point altitude, and similarly, the delta velocity represents the difference in velocity for the point of interest and the database point for velocity. The red lines correspond to the mean of the non-zero absolute value deltas; these were used to apply constraint values of 5800 m and 900 m/s to the final data collected for the histogram plots (constrained case). This meant that while all of the 185 points were still included in the full database, if any point outside the specified delta altitude or velocity range was used for the interpolation, that result would not be included in the final histogram plot.

From the data collected, histograms were plotted showing the number of counts versus heat flux percent difference (based on the normalized interpolation and then redimensionalizing). The results of the unconstrained results and constrained results are shown in Figure 31.

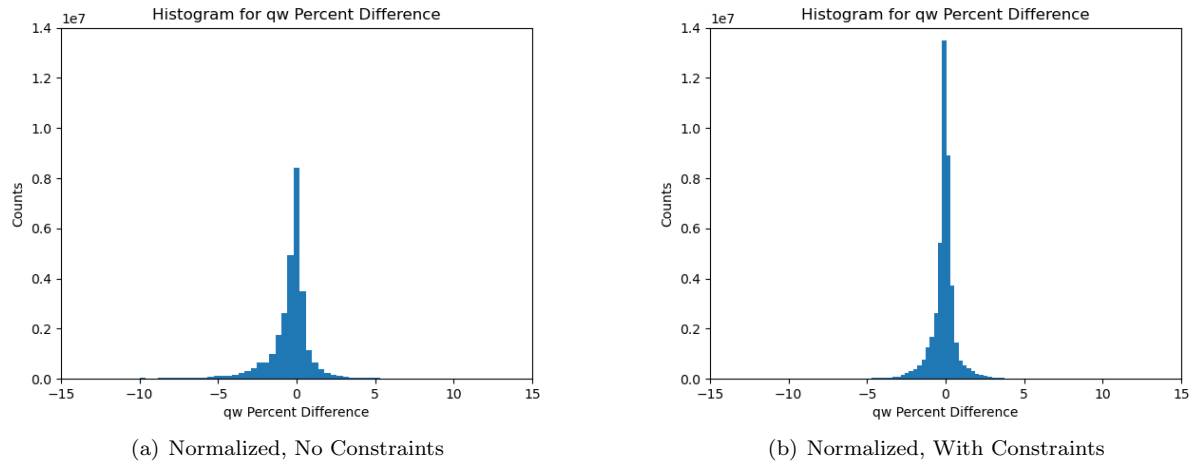


**Figure 31.** The plots show the results for the heat flux percent difference (based on interpolating to the normalized value and redimensionalizing) with no parameter constraints (left) and parameter constraints (right).

The plot on the lefthand side in Figure 31 corresponds to the results without any altitude or velocity spacing constraints, and the plot on the right corresponds to applying the aforementioned altitude and velocity constraints to the results. For the unconstrained case, 97.19% fell within  $\pm 5\%$  and over 99% (99.56%) were within  $\pm 5\%$  for the constrained case. As discovered from the previous section, if the

proper interpolation space is selected for a given variable of interest (in this case heat flux), the error in the result will be minimized. As the results of this section show, by ensuring that the difference between the interpolated point of interest and the nearby CFD database points remain within a specified altitude and velocity, the results can be even further improved, with nearly 100% of the heat flux percent difference being within +/-5%. This insight is important for future database development and coverage assessments.

While the recommendation for 5800 m in altitude spacing and 900 m/s in velocity spacing may not always be applicable as certain regions of the flight space may require more or less resolution, they are guidelines that can be used as a starting point for developing an aerothermal database using the  $\text{Log}(\rho)$ ,  $\text{Log}(V)$ ,  $\alpha$  interpolation space where heat flux is the primary variable of interest, or for assessing current database coverage when this interpolation space will be implemented. While heat flux is used as an example here, a similar process could be applied to other dependent variables of interest in order to determine what the altitude and velocity spacing should be for a database for a given interpolation space. In addition to being useful for future database development, the recommended spacing values could also be useful as a guideline for determining where to add database points for sufficient database coverage as the design cycle evolves.

#### IV. Conclusion

A methodology for estimating six critical aerothermodynamic parameters of interest ( $q_w$ ,  $P_w$ ,  $\tau_w$ ,  $M_e$ ,  $\delta$ ,  $Re_\theta$ ) throughout an entry corridor has been proposed. The proposed methodology recommends interpolating between discrete CFD solutions in a  $\text{Log}(\rho)$ ,  $\text{Log}(V)$ ,  $\alpha$  interpolation space. Four other interpolation spaces were considered and the  $\text{Log}(\rho)$ ,  $\text{Log}(V)$ ,  $\alpha$  interpolation space was found to perform best. Two approaches were considered within each of the five interpolation spaces, 1) interpolating for the parameters of interest directly from the CFD solutions and, 2) normalizing the parameters of interest before interpolating and then redimensionalizing to the point of interest after interpolating. The results showed that interpolating for edge Mach number ( $M_e$ ) and boundary layer thickness ( $\delta$ ) directly in the  $\text{Log}(\rho)$ ,  $\text{Log}(V)$ ,  $\alpha$  interpolation space performed better than all the other approaches considered. For heat flux ( $q_w$ ), pressure ( $P_w$ ), shear stress ( $\tau_w$ ), and momentum thickness Reynolds number ( $Re_\theta$ ), the results showed that normalizing the CFD results before interpolating, and then redimensionalizing with the same normalizing quantities computed at the point of interest out performed interpolating for these parameters directly.

The sensitivity of the proposed methodology to the CFD solution resolution in velocity, altitude, and angle-of-attack dimensions was also evaluated. The heat flux ( $q_w$ ), pressure ( $P_w$ ), and edge Mach number ( $M_e$ ) were found to be relatively insensitive to reduced resolution in each of these dimensions. The shear stress ( $\tau_w$ ) and boundary layer thickness ( $\delta$ ) were found to be sensitive to the resolution of each of these dimensions, particularly the altitude, or freestream density. The momentum thickness Reynolds number ( $Re_\theta$ ) was most sensitive to the resolution in the velocity dimension, though not until the velocity dimension was reduced to five points (3, 5, 7, 9, 11 km/s).

This paper also investigated an approach for determining sufficient database coverage and provides a recommendation on where to add points in altitude and velocity based on a desired level of accuracy for the given interpolation space and dependent variable. The method for doing so consisted of starting with the full 185 CFD solution database for the Apollo 4 trajectory, removing a point from the interpolation space to interpolate to, and subsequently removing points from the interpolation space that were being used to interpolate to that point of interest. Various values were calculated and used to develop recommended delta values in altitude and velocity, where delta is the difference between the point to interpolate to and each of the CFD database points used in the interpolation of that point of interest. It was found that for a  $\text{Log}(\rho)$ ,  $\text{Log}(V)$ ,  $\alpha$  interpolation space with the focus of minimizing the error in heat flux, the recommended altitude and velocity spacing in the CFD database should not exceed 5800 m in altitude and 900 m/s in velocity to achieve over 99% of the heat flux percent different values to be within +/-5% for this specific trajectory using the normalized approach. These delta parameter values are a recommendation or guideline, and depending on the application, more or less spacing may be required for a database. However, the process described can be applied to any interpolation space for any variable of interest for determining recommended independent parameter spacing.

## Appendix

### A. Histograms of Percent Difference in Each Interpolation Space

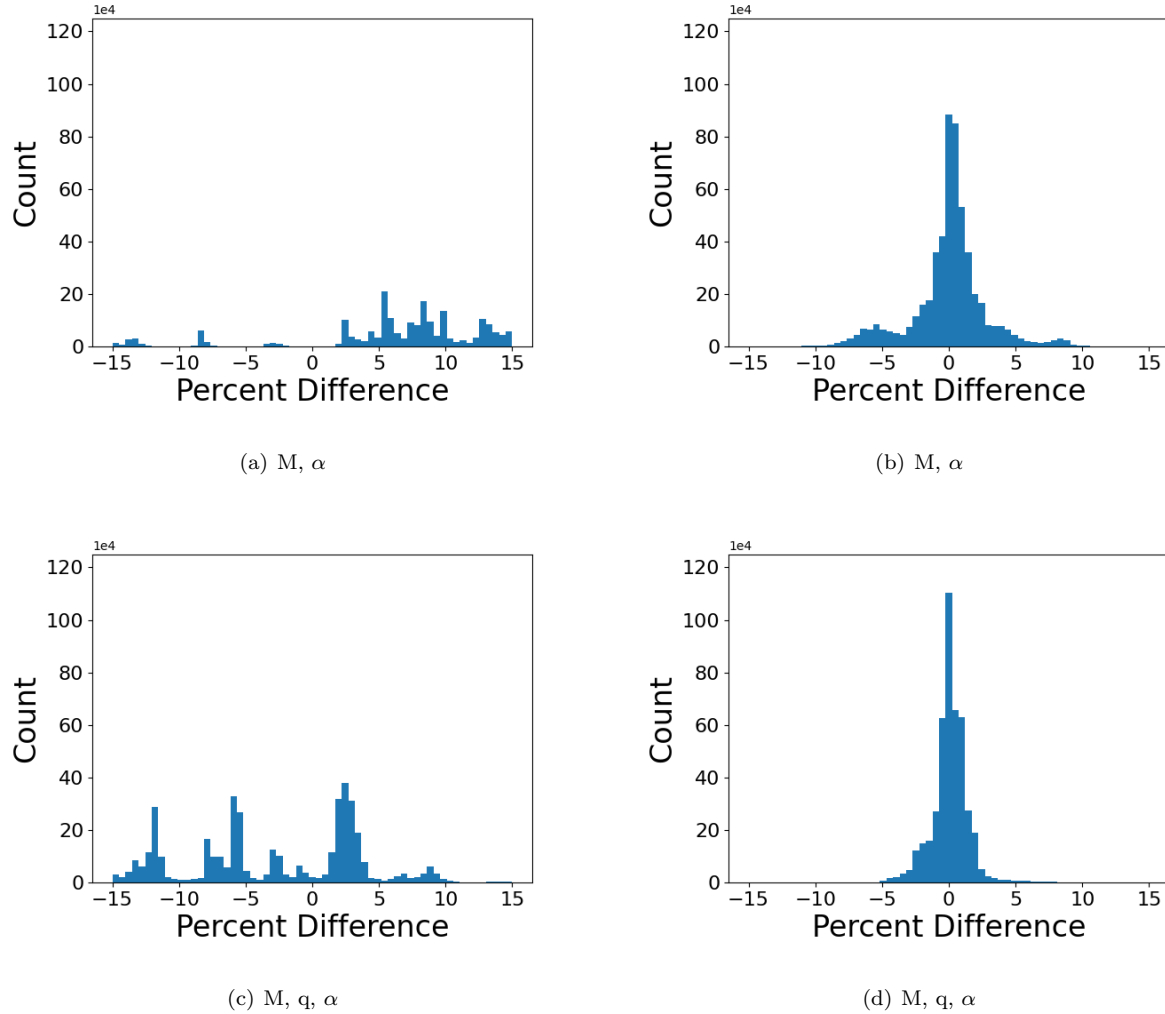
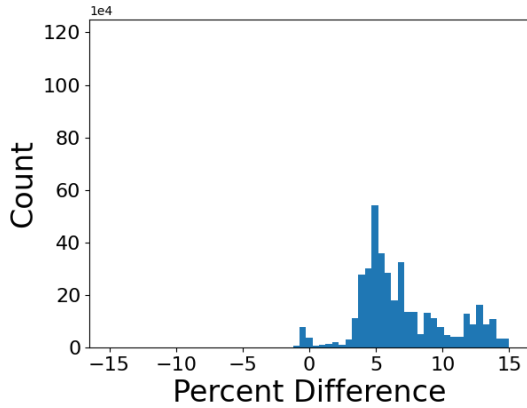
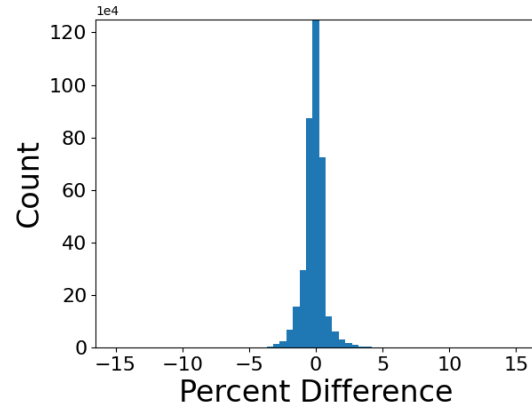


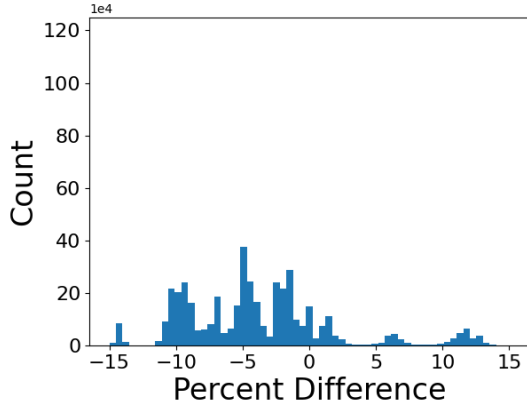
Figure 32. Histograms of the percent difference for heat flux ( $q_w$ ) in each interpolation space using Mach, dynamic pressure, and angle-of-attack. Direct interpolation for heat flux ( $q_w$ ) on the left column and interpolation of normalized heat flux ( $q_w$ ) on the right column.



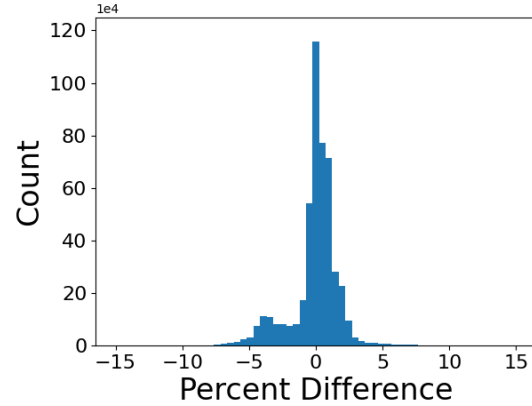
(a)  $\text{Log}(\rho)$ ,  $\text{Log}(V)$ ,  $\alpha$



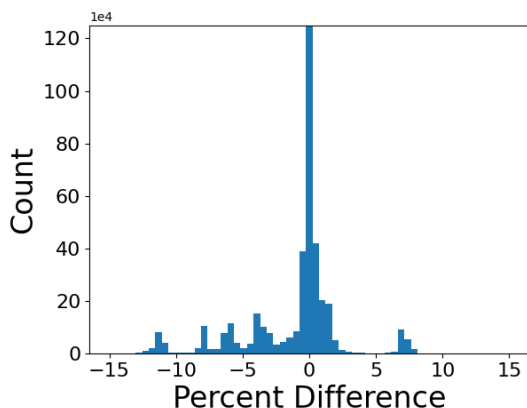
(b)  $\text{Log}(\rho)$ ,  $\text{Log}(V)$ ,  $\alpha$



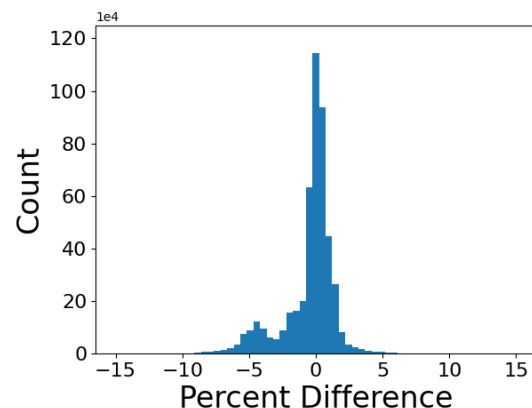
(c)  $\rho$ ,  $V^2$ ,  $\alpha$



(d)  $\rho$ ,  $V^2$ ,  $\alpha$

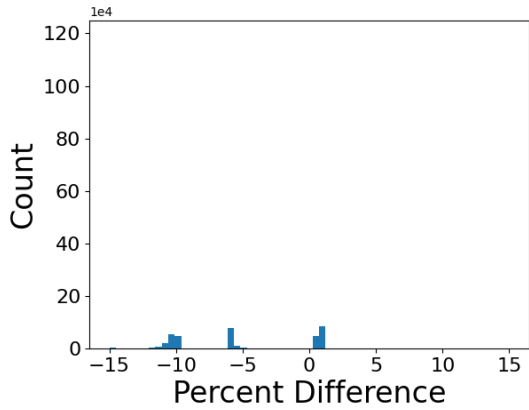


(e)  $\sqrt{\rho}$ ,  $V^3$ ,  $\alpha$

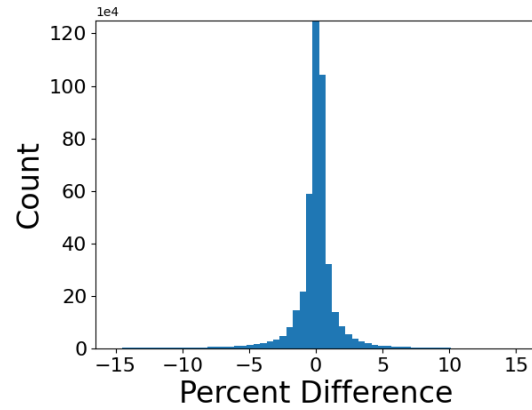


(f)  $\sqrt{\rho}$ ,  $V^3$ ,  $\alpha$

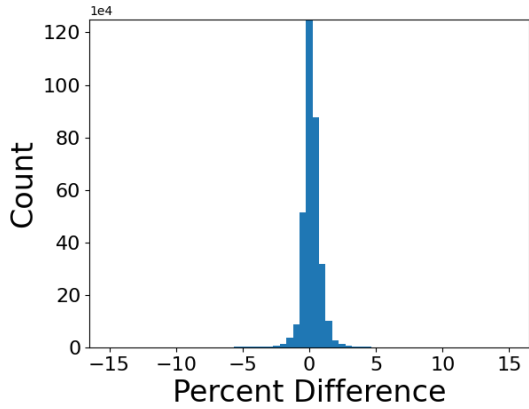
**Figure 33.** Histograms of the percent difference for heat flux ( $q_w$ ) in each interpolation space using density, velocity, and angle-of-attack. Direct interpolation for heat flux ( $q_w$ ) on the left column and interpolation of normalized heat flux ( $q_w$ ) on the right column.



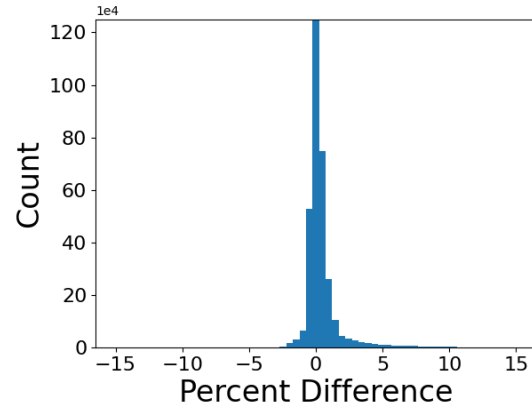
(a)  $M, \alpha$



(b)  $M, \alpha$

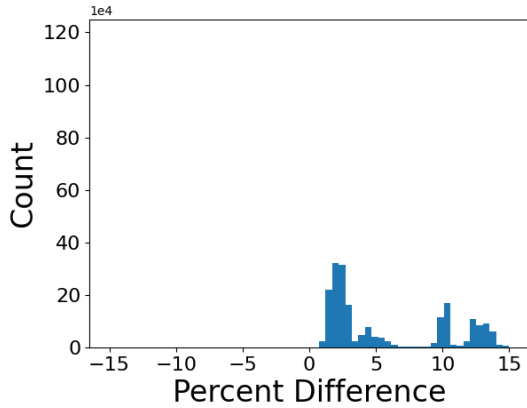


(c)  $M, q, \alpha$

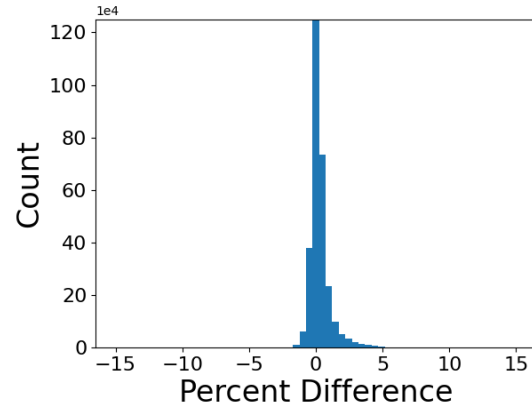


(d)  $M, q, \alpha$

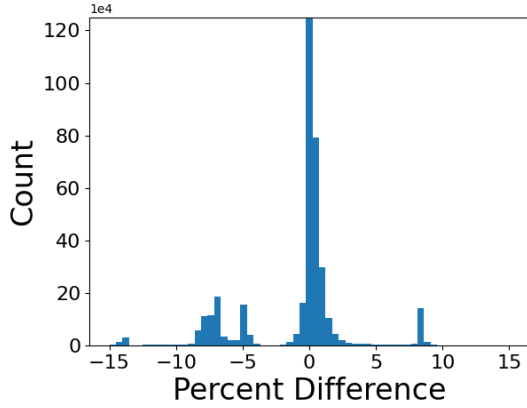
**Figure 34.** Histograms of the percent difference for pressure ( $P_w$ ) in each interpolation space using Mach, dynamic pressure, and angle-of-attack. Direct interpolation for pressure ( $P_w$ ) on the left column and interpolation of normalized pressure ( $P_w$ ) on the right column.



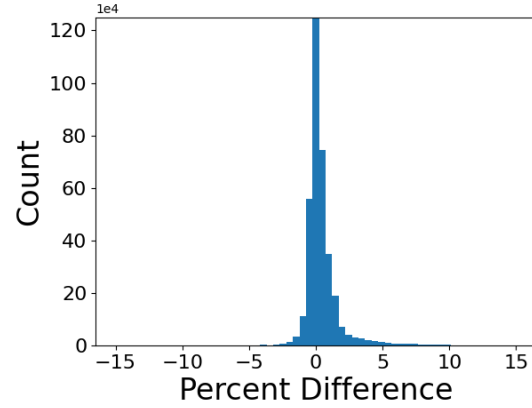
(a)  $\text{Log}(\rho)$ ,  $\text{Log}(V)$ ,  $\alpha$



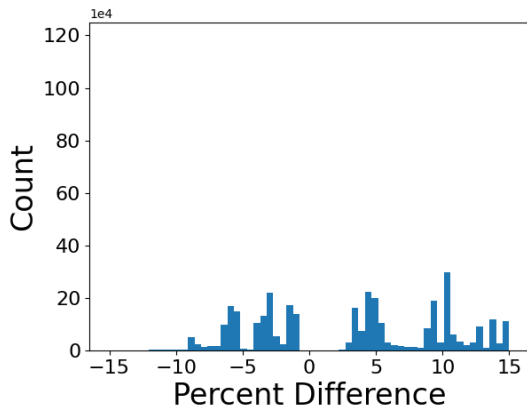
(b)  $\text{Log}(\rho)$ ,  $\text{Log}(V)$ ,  $\alpha$



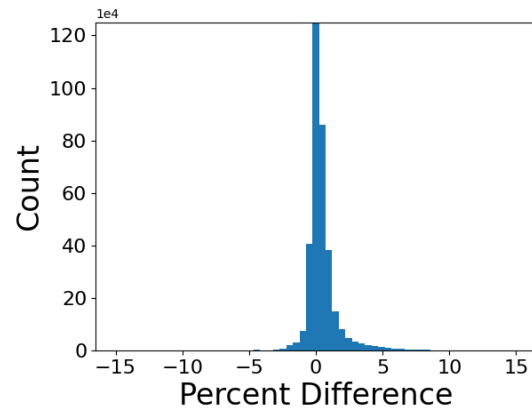
(c)  $\rho$ ,  $v^2$ ,  $\alpha$



(d)  $\rho$ ,  $v^2$ ,  $\alpha$



(e)  $\sqrt{\rho}$ ,  $v^3$ ,  $\alpha$



(f)  $\sqrt{\rho}$ ,  $v^3$ ,  $\alpha$

**Figure 35.** Histograms of the percent difference for pressure ( $P_w$ ) in each interpolation space using density, velocity, and angle-of-attack. Direct interpolation for pressure ( $P_w$ ) on the left column and interpolation of normalized pressure ( $P_w$ ) on the right column.

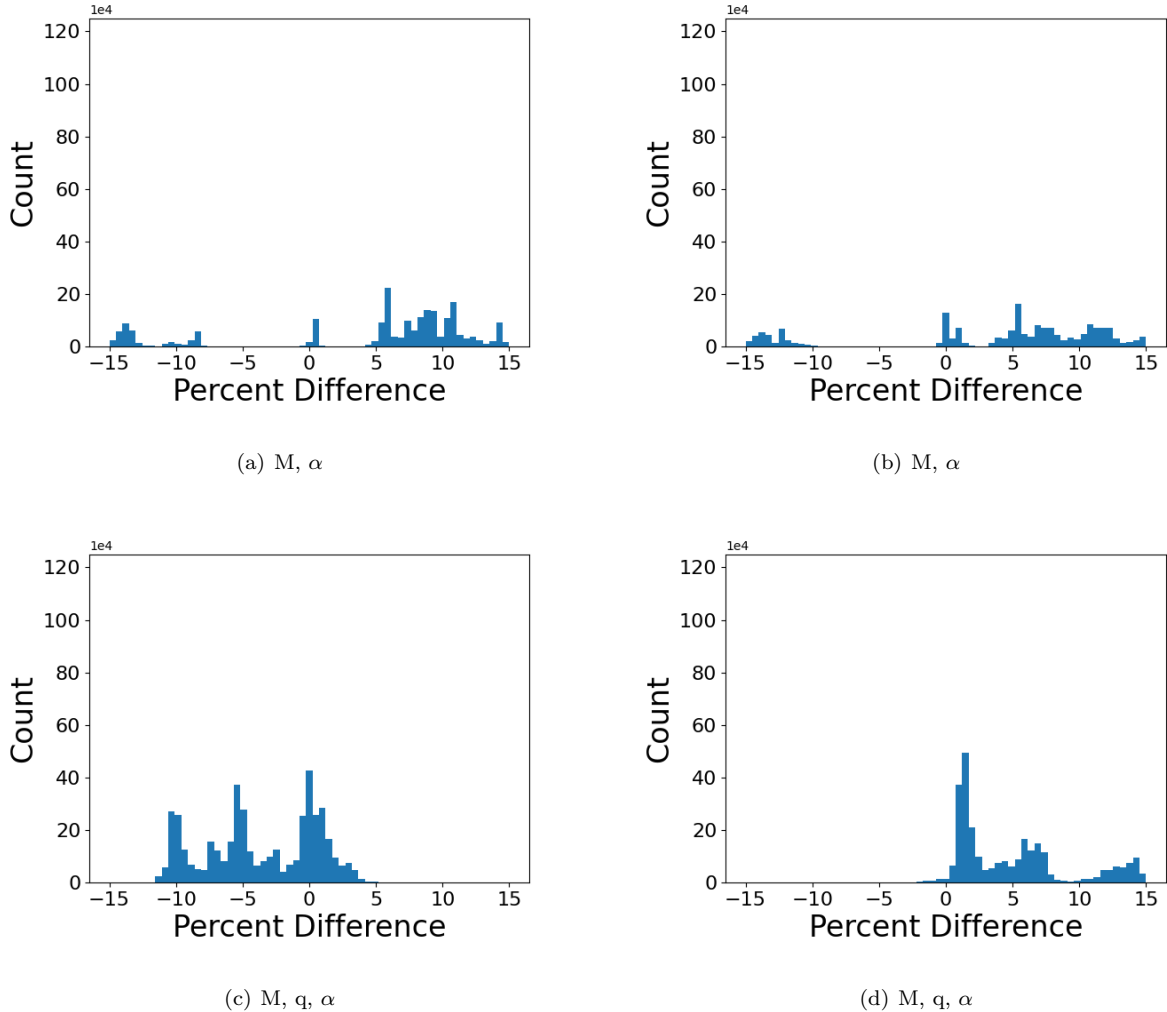


**Figure 36.** Histograms of the percent difference for shear stress ( $\tau_w$ ) in each interpolation space using Mach, dynamic pressure, and angle-of-attack. Direct interpolation for shear stress ( $\tau_w$ ) on the left column and interpolation of normalized shear stress ( $\tau_w$ ) on the right column.

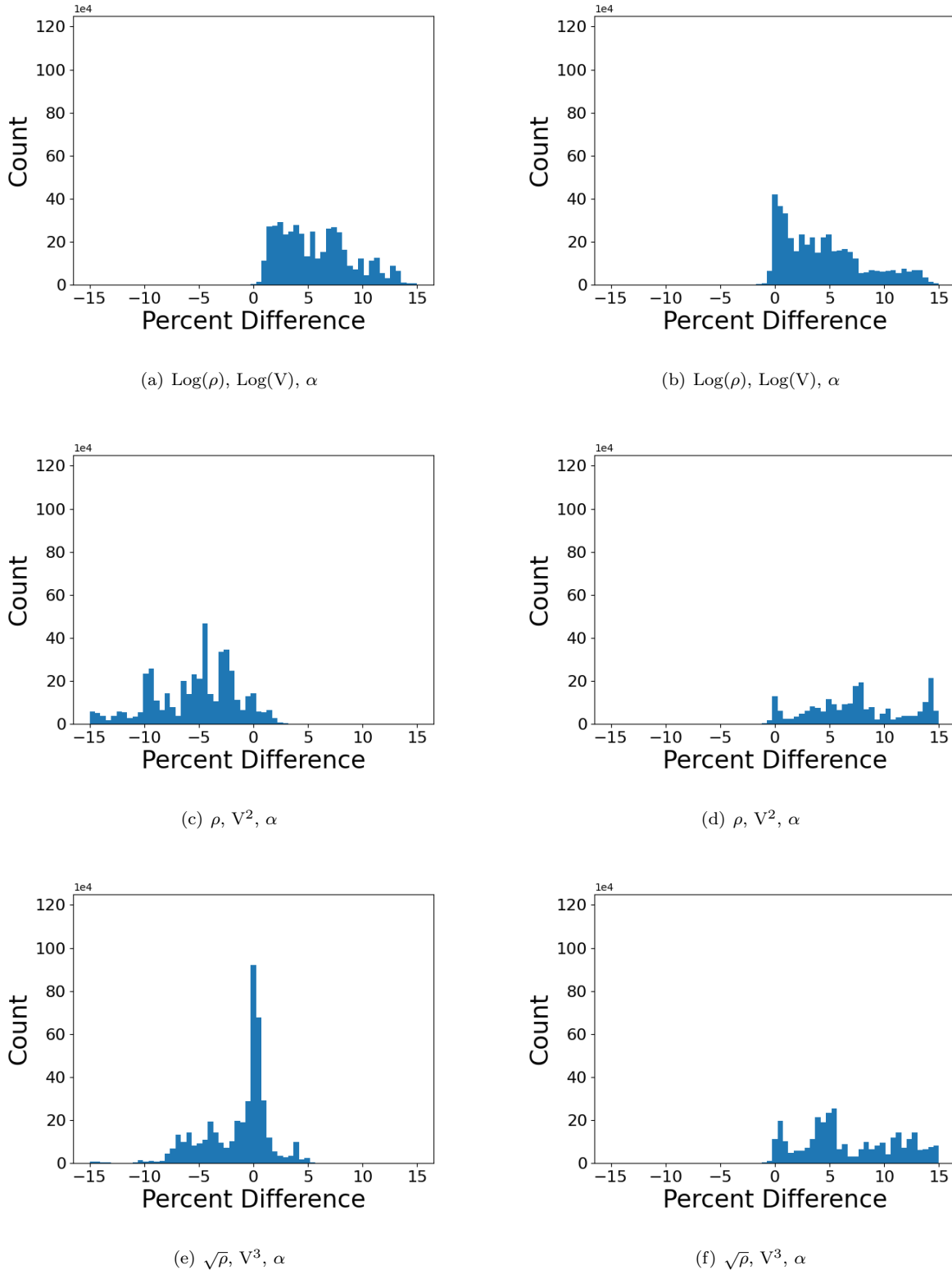
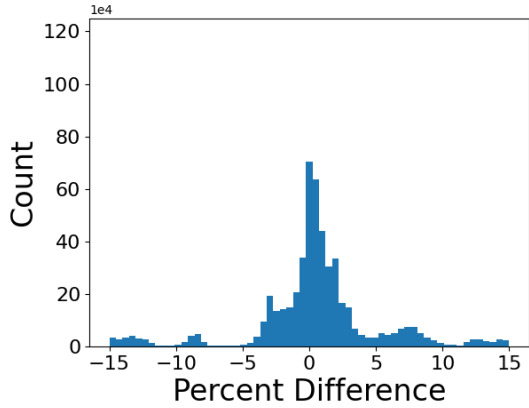
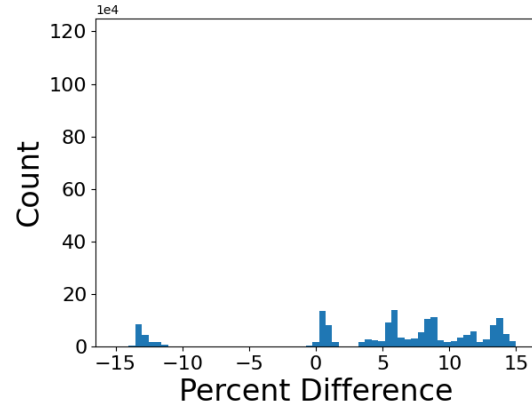


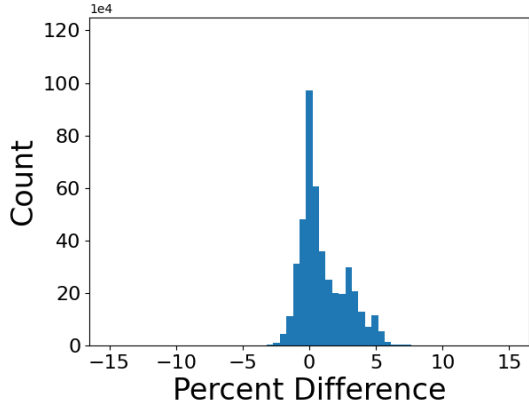
**Figure 37.** Histograms of the percent difference for shear stress ( $\tau_w$ ) in each interpolation space using density, velocity, and angle-of-attack. Direct interpolation for shear stress ( $\tau_w$ ) on the left column and interpolation of normalized shear stress ( $\tau_w$ ) on the right column.



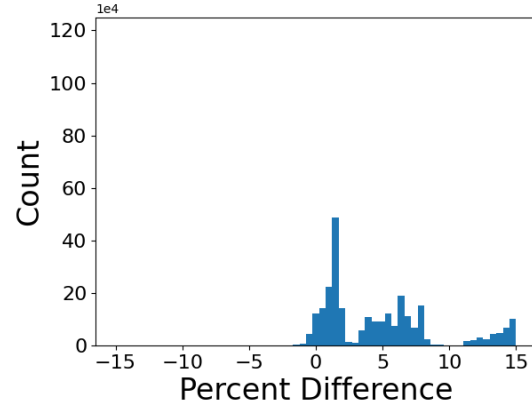
(a)  $M, \alpha$



(b)  $M, \alpha$

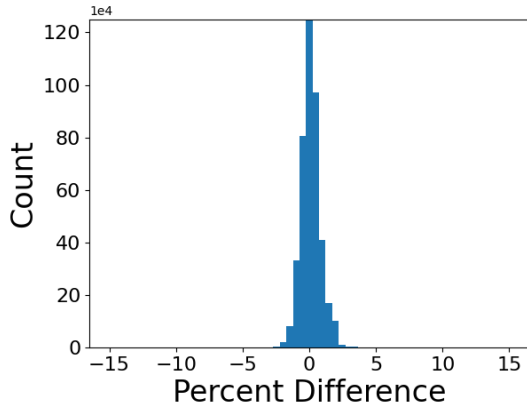


(c)  $M, q, \alpha$

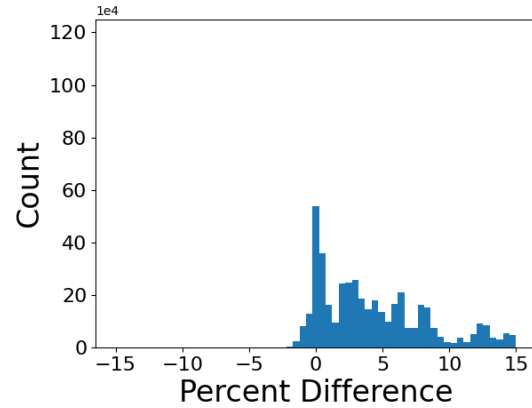


(d)  $M, q, \alpha$

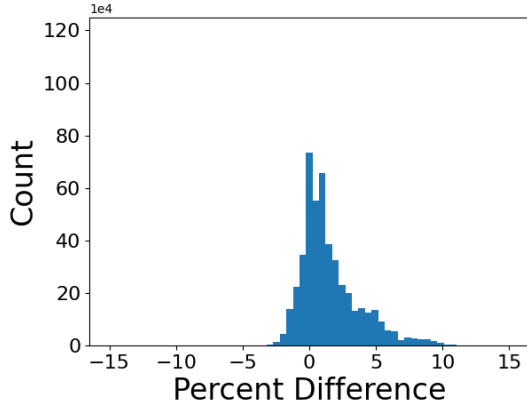
**Figure 38.** Histograms of the percent difference for edge Mach number ( $M_e$ ) in each interpolation space using Mach, dynamic pressure, and angle-of-attack. Direct interpolation for edge Mach number ( $M_e$ ) on the left column and interpolation of normalized edge Mach number ( $M_e$ ) on the right column.



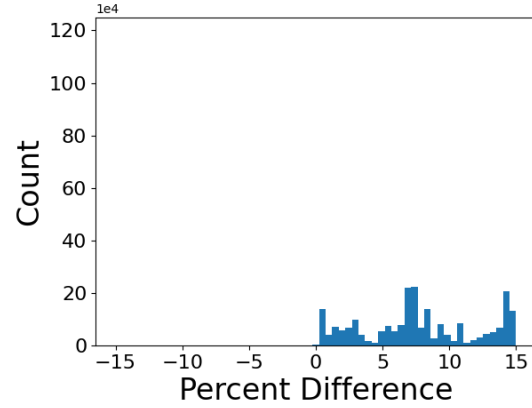
(a)  $\text{Log}(\rho)$ ,  $\text{Log}(V)$ ,  $\alpha$



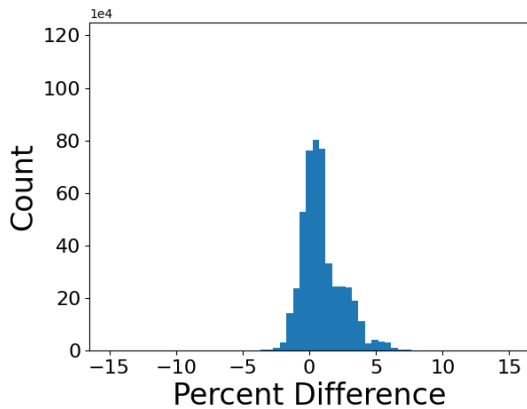
(b)  $\text{Log}(\rho)$ ,  $\text{Log}(V)$ ,  $\alpha$



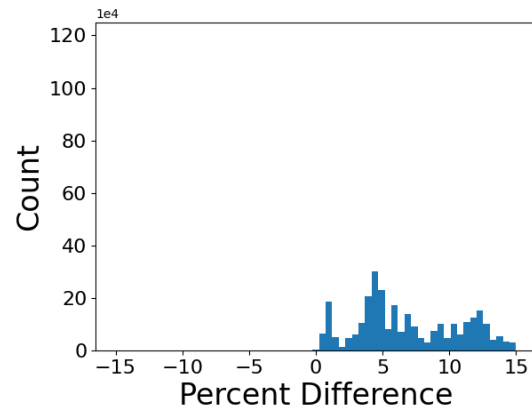
(c)  $\rho$ ,  $V^2$ ,  $\alpha$



(d)  $\rho$ ,  $V^2$ ,  $\alpha$

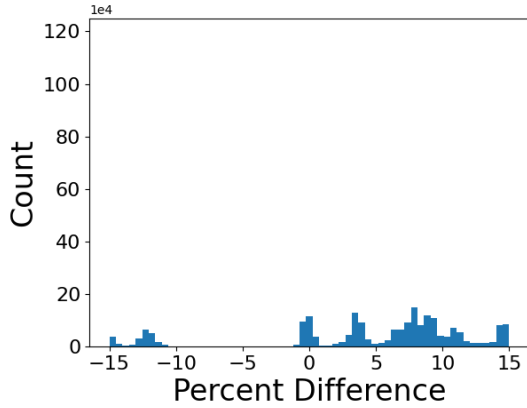


(e)  $\sqrt{\rho}$ ,  $V^3$ ,  $\alpha$

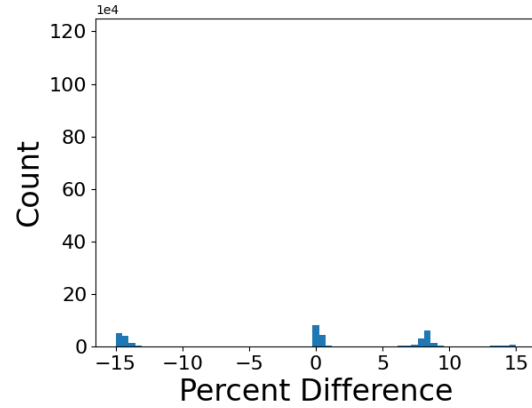


(f)  $\sqrt{\rho}$ ,  $V^3$ ,  $\alpha$

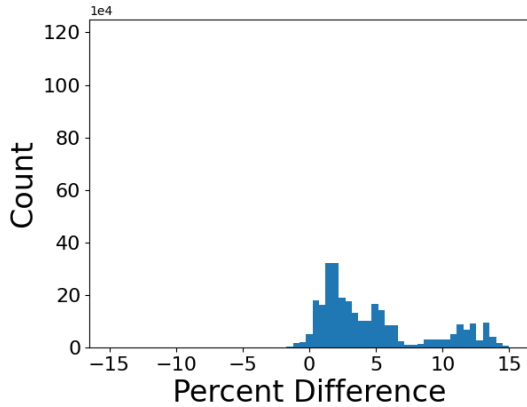
**Figure 39.** Histograms of the percent difference for edge Mach number ( $M_e$ ) in each interpolation space using density, velocity, and angle-of-attack. Direct interpolation for edge Mach number ( $M_e$ ) on the left column and interpolation of normalized edge Mach number ( $M_e$ ) on the right column.



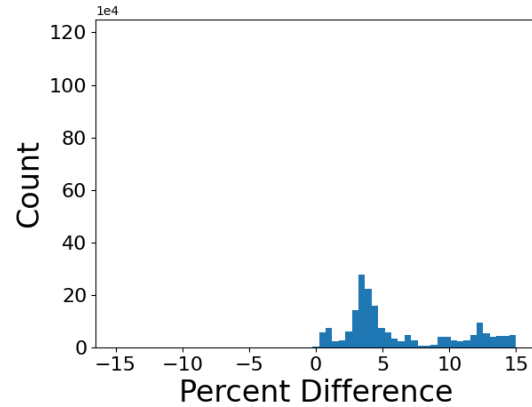
(a)  $M, q, \alpha$



(b)  $M, \alpha$

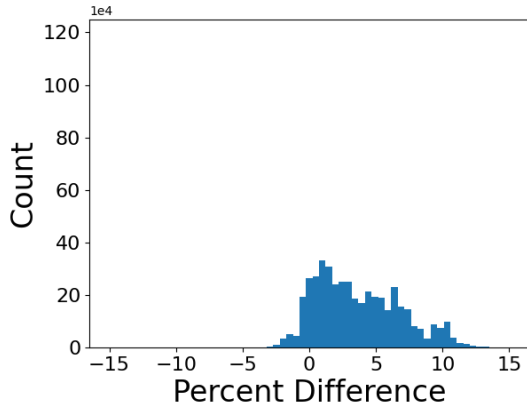


(c)  $M, q, \alpha$

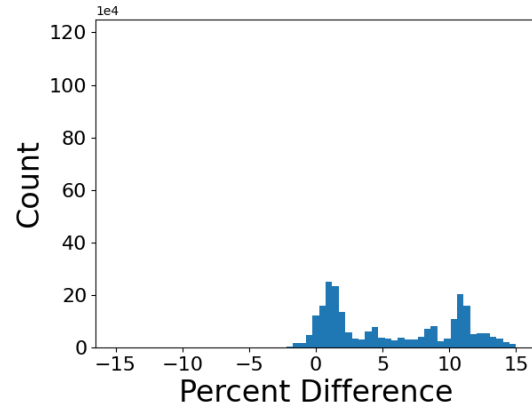


(d)  $M, q, \alpha$

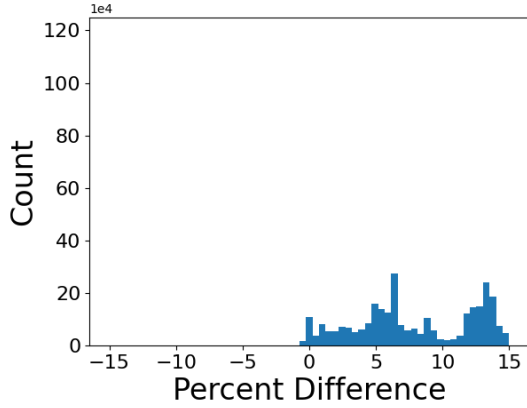
**Figure 40.** Histograms of the percent difference for boundary layer thickness ( $\delta$ ) in each interpolation space using Mach, dynamic pressure, and angle-of-attack. Direct interpolation for boundary layer thickness ( $\delta$ ) on the left column and interpolation of normalized boundary layer thickness ( $\delta$ ) on the right column.



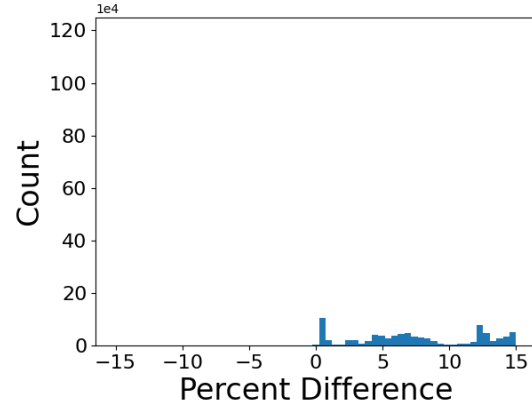
(a)  $\text{Log}(\rho)$ ,  $\text{Log}(V)$ ,  $\alpha$



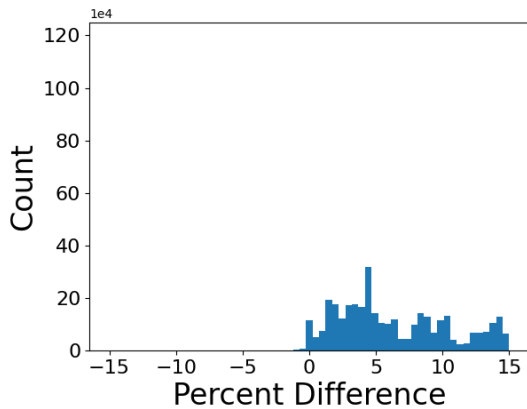
(b)  $\text{Log}(\rho)$ ,  $\text{Log}(V)$ ,  $\alpha$



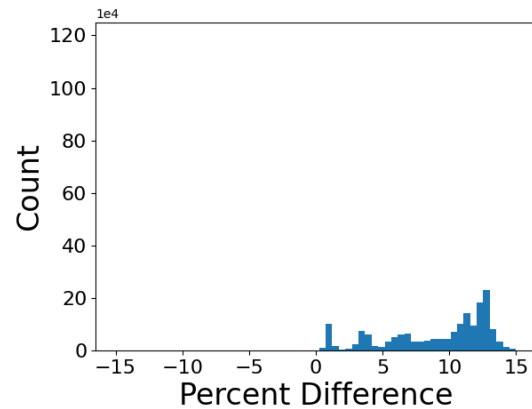
(c)  $\rho$ ,  $V^2$ ,  $\alpha$



(d)  $\rho$ ,  $V^2$ ,  $\alpha$

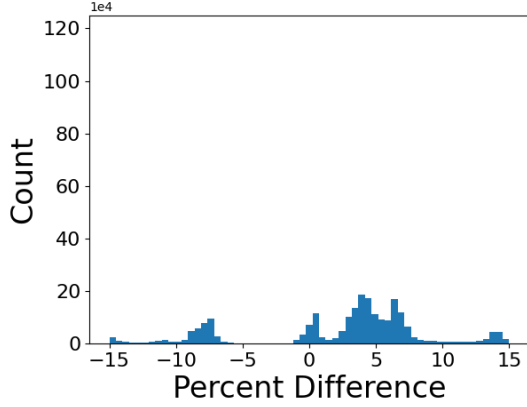


(e)  $\sqrt{\rho}$ ,  $V^3$ ,  $\alpha$

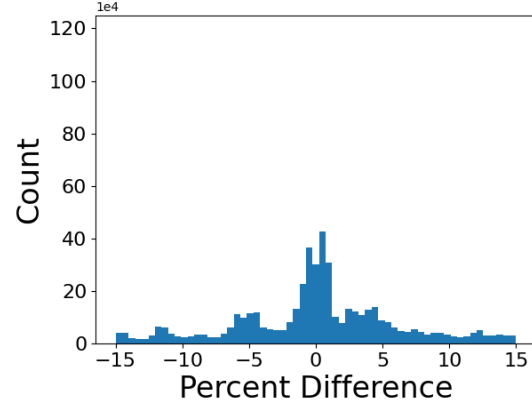


(f)  $\sqrt{\rho}$ ,  $V^3$ ,  $\alpha$

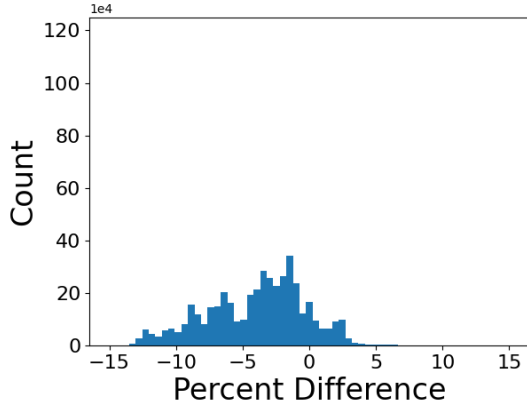
**Figure 41. Histograms of the percent difference for boundary layer thickness ( $\delta$ ) in each interpolation space using density, velocity, and angle-of-attack. Direct interpolation for boundary layer thickness ( $\delta$ ) on the left column and interpolation of normalized boundary layer thickness ( $\delta$ ) on the right column.**



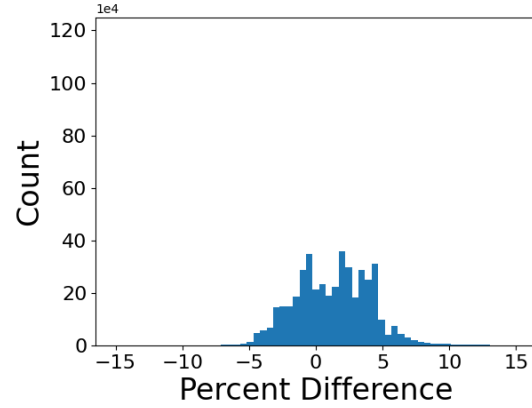
(a)  $M, \alpha$



(b)  $M, \alpha$

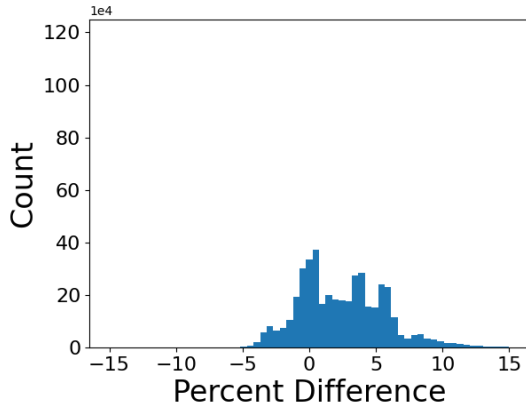


(c)  $M, q, \alpha$

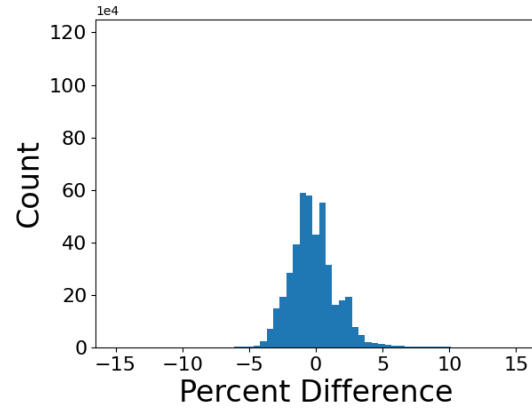


(d)  $M, q, \alpha$

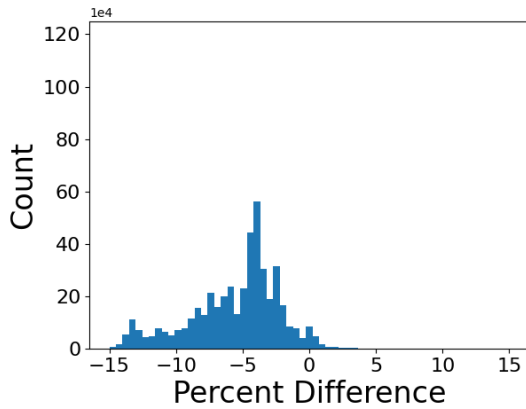
**Figure 42.** Histograms of the percent difference for momentum thickness Reynolds number ( $Re_\theta$ ) in each interpolation space using Mach, dynamic pressure, and angle-of-attack. Direct interpolation for momentum thickness Reynolds number ( $Re_\theta$ ) on the left column and interpolation of normalized momentum thickness Reynolds number ( $Re_\theta/q$ ) on the right column.



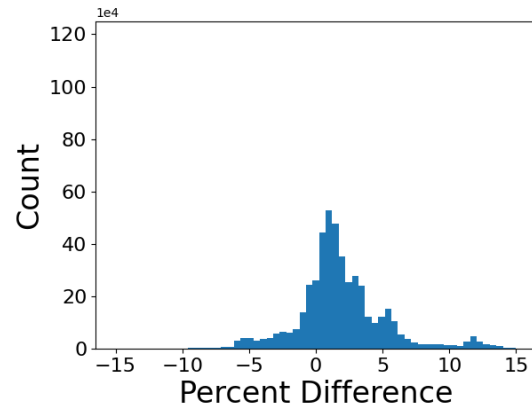
(a)  $\text{Log}(\rho)$ ,  $\text{Log}(V)$ ,  $\alpha$



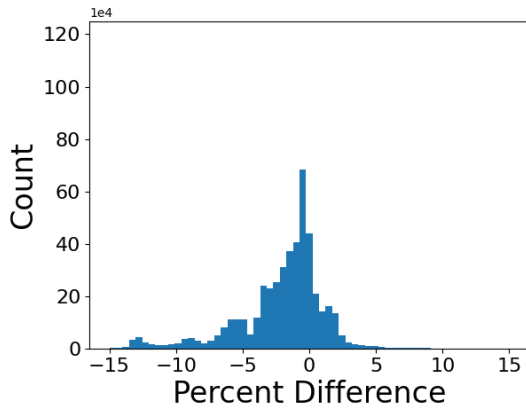
(b)  $\text{Log}(\rho)$ ,  $\text{Log}(V)$ ,  $\alpha$



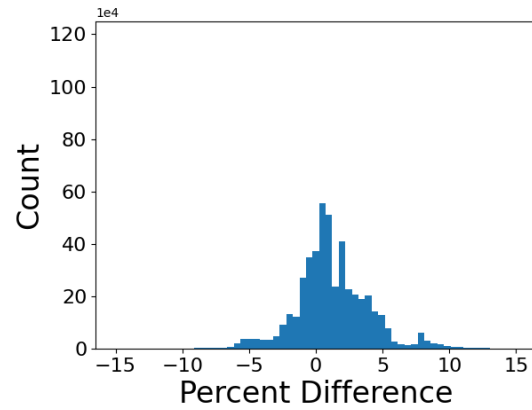
(c)  $\rho$ ,  $V^2$ ,  $\alpha$



(d)  $\rho$ ,  $V^2$ ,  $\alpha$



(e)  $\sqrt{\rho}$ ,  $V^3$ ,  $\alpha$



(f)  $\sqrt{\rho}$ ,  $V^3$ ,  $\alpha$

**Figure 43.** Histograms of the percent difference for momentum thickness Reynolds number ( $\text{Re}_\theta$ ) in each interpolation space using density, velocity, and angle-of-attack. Direct interpolation for momentum thickness Reynolds number ( $\text{Re}_\theta$ ) on the left column and interpolation of normalized momentum thickness Reynolds number ( $\text{Re}_\theta$ ) on the right column.

## B. CFD Solutions Used to Construct the Interpolation Spaces at Each Resolution

Velocity km/s	Altitude km	Angle-of-Attack deg.	Full	Reduced Velocity Level 1		Reduced Velocity Level 2		Reduced Altitude		Reduced Angle-of-Attack		Reduced Velocity Level 1 and Altitude		Reduced Velocity Level 2 and Altitude	
				X	X	X	X	X	X	X	X	X	X	X	X
3.0	35.0	152.0	X												
3.0	35.0	154.0	X	X	X	X	X	X	X			X		X	X
3.0	35.0	156.0	X	X	X	X	X	X	X	X	X	X	X	X	X
3.0	40.0	152.0	X	X	X	X				X					
3.0	40.0	154.0	X	X	X	X									
3.0	40.0	156.0	X	X	X	X				X					
3.0	45.0	152.0	X	X	X	X	X	X	X	X	X	X	X	X	X
3.0	45.0	154.0	X	X	X	X	X	X	X		X		X	X	X
3.0	45.0	156.0	X	X	X	X	X	X	X	X	X	X	X	X	X
3.5	35.0	152.0	X					X	X						
3.5	35.0	154.0	X					X							
3.5	35.0	156.0	X					X							
3.5	40.0	152.0	X								X				
3.5	40.0	154.0	X												
3.5	40.0	156.0	X									X			
3.5	45.0	152.0	X									X			
3.5	45.0	154.0	X										X		
3.5	45.0	156.0	X										X		
4.0	40.0	152.0	X	X				X	X	X	X	X	X	X	X
4.0	40.0	154.0	X	X				X				X		X	X
4.0	45.0	152.0	X	X							X				
4.0	45.0	154.0	X	X											
4.0	45.0	156.0	X	X							X				
4.0	50.0	152.0	X	X				X	X	X	X	X	X	X	X
4.0	50.0	154.0	X	X				X		X		X		X	X
4.0	50.0	156.0	X	X				X		X	X	X	X	X	X
4.5	40.0	152.0	X					X	X						
4.5	40.0	154.0	X							X					
4.5	40.0	156.0	X							X	X				
4.5	45.0	152.0	X								X				
4.5	45.0	154.0	X												

Velocity km/s	Altitude km	Angle-of-Attack deg.	Full	Reduced Velocity Level 1	Reduced Velocity Level 2	Reduced Altitude	Reduced Angle-of-Attack	Reduced Velocity Level 1 and Altitude	Reduced Velocity Level 2 and Altitude
4.5	45.0	156.0	X				X		
4.5	50.0	152.0	X			X	X		
4.5	50.0	154.0	X			X			
4.5	50.0	156.0	X			X	X		
5.0	45.0	152.0	X	X	X	X	X	X	X
5.0	45.0	154.0	X	X	X	X		X	X
5.0	45.0	156.0	X	X	X	X	X	X	X
5.0	50.0	152.0	X	X	X		X		
5.0	50.0	154.0	X	X	X				
5.0	50.0	156.0	X	X	X		X		
5.0	55.0	152.0	X	X	X	X	X	X	X
5.0	55.0	154.0	X	X	X	X		X	X
5.0	55.0	156.0	X	X	X	X	X	X	X
5.5	50.0	152.0	X			X	X		
5.5	50.0	154.0	X			X			
5.5	50.0	156.0	X			X			
5.5	55.0	152.0	X				X		
5.5	55.0	154.0	X						
5.5	55.0	156.0	X						
5.5	55.0	158.0	X				X		
5.5	60.0	152.0	X			X	X		
5.5	60.0	154.0	X			X			
5.5	60.0	156.0	X			X			
5.5	60.0	158.0	X			X	X		
6.0	55.0	152.0	X	X		X	X	X	X
6.0	55.0	154.0	X	X		X		X	X
6.0	55.0	156.0	X	X		X		X	X
6.0	55.0	158.0	X	X		X	X	X	X
6.0	60.0	152.0	X	X			X		
6.0	60.0	154.0	X	X					
6.0	60.0	156.0	X	X					
6.0	60.0	158.0	X	X			X		
6.0	65.0	152.0	X	X			X		

Velocity km/s	Altitude km	Angle-of-Attack deg.	Full		Reduced Velocity Level 1	Reduced Velocity Level 2	Reduced Altitude	Reduced Angle-of-Attack	Reduced Velocity Level 1 and Altitude	Reduced Velocity Level 2 and Altitude
			X	X						
6.0	65.0	154.0	X	X						
6.0	65.0	156.0	X	X						
6.0	65.0	158.0	X	X				X		
6.0	70.0	152.0	X	X			X	X	X	
6.0	70.0	154.0	X	X			X		X	
6.0	70.0	156.0	X	X			X		X	
6.0	70.0	158.0	X	X			X	X	X	
6.5	65.0	152.0	X				X	X		
6.5	65.0	154.0	X				X			
6.5	65.0	156.0	X				X			
6.5	65.0	158.0	X				X	X		
6.5	70.0	152.0	X					X		
6.5	70.0	154.0	X							
6.5	70.0	156.0	X							
6.5	70.0	158.0	X					X		
6.5	75.0	152.0	X					X		
6.5	75.0	154.0	X							
6.5	75.0	156.0	X							
6.5	75.0	158.0	X						X	
6.5	80.0	152.0	X				X	X		
6.5	80.0	154.0	X				X			
6.5	80.0	156.0	X				X			
6.5	80.0	158.0	X					X	X	
7.0	60.0	152.0	X	X	X	X	X	X	X	X
7.0	60.0	154.0	X	X	X	X			X	X
7.0	60.0	156.0	X	X	X	X			X	X
7.0	60.0	158.0	X	X	X	X	X	X	X	X
7.0	65.0	152.0	X	X	X			X		
7.0	65.0	154.0	X	X	X					
7.0	65.0	156.0	X	X	X					
7.0	65.0	158.0	X	X	X			X		
7.0	70.0	152.0	X	X	X			X		
7.0	70.0	154.0	X	X	X				X	

Velocity km/s	Altitude km	Angle-of-Attack deg.	Full			Reduced Velocity Level 1	Reduced Velocity Level 2	Reduced Altitude	Reduced Angle-of-Attack	Reduced Velocity Level 1 and Altitude	Reduced Velocity Level 2 and Altitude
7.0	70.0	156.0	X	X	X						
7.0	70.0	158.0	X	X	X			X			
7.0	75.0	152.0	X	X	X	X	X	X	X	X	
7.0	75.0	154.0	X	X	X	X	X		X	X	
7.0	75.0	156.0	X	X	X	X			X	X	
7.0	75.0	158.0	X	X	X	X	X	X	X	X	
7.5	55.0	152.0	X				X	X			
7.5	55.0	154.0	X				X				
7.5	55.0	156.0	X				X				
7.5	55.0	158.0	X				X	X			
7.5	60.0	152.0	X						X		
7.5	60.0	154.0	X								
7.5	60.0	156.0	X								
7.5	60.0	158.0	X						X		
7.5	65.0	152.0	X					X	X		
7.5	65.0	154.0	X					X			
7.5	65.0	156.0	X					X			
7.5	65.0	158.0	X					X	X		
8.0	55.0	152.0	X	X			X	X	X	X	
8.0	55.0	154.0	X	X			X			X	
8.0	55.0	156.0	X	X			X			X	
8.0	55.0	158.0	X	X			X	X	X	X	
8.0	60.0	152.0	X	X					X		
8.0	60.0	154.0	X	X							
8.0	60.0	156.0	X	X							
8.0	60.0	158.0	X	X					X		
8.0	65.0	152.0	X	X			X	X	X	X	
8.0	65.0	154.0	X	X			X			X	
8.0	65.0	156.0	X	X			X			X	
8.0	65.0	158.0	X	X			X	X	X	X	
8.5	50.0	152.0	X				X	X			
8.5	50.0	154.0	X				X				
8.5	50.0	156.0	X				X				

Velocity km/s	Altitude km	Angle-of-Attack deg.	Full	Reduced Velocity Level 1	Reduced Velocity Level 2	Reduced Altitude	Reduced Angle-of-Attack	Reduced Velocity Level 1 and Altitude	Reduced Velocity Level 2 and Altitude
8.5	50.0	158.0	X			X	X		
8.5	55.0	152.0	X			X			
8.5	55.0	154.0	X						
8.5	55.0	156.0	X						
8.5	55.0	158.0	X				X		
8.5	60.0	152.0	X			X	X		
8.5	60.0	154.0	X			X			
8.5	60.0	156.0	X			X			
8.5	60.0	158.0	X			X	X		
9.0	50.0	152.0	X	X	X	X	X	X	X
9.0	50.0	154.0	X	X	X	X		X	X
9.0	50.0	156.0	X	X	X	X	X	X	X
9.0	55.0	152.0	X	X	X		X		
9.0	55.0	154.0	X	X	X				
9.0	55.0	156.0	X	X	X		X		
9.0	60.0	152.0	X	X	X	X	X	X	X
9.0	60.0	154.0	X	X	X	X		X	X
9.0	60.0	156.0	X	X	X	X	X	X	X
9.5	50.0	152.0	X			X	X		
9.5	50.0	154.0	X			X			
9.5	50.0	156.0	X			X	X		
9.5	55.0	152.0	X				X		
9.5	55.0	154.0	X						
9.5	60.0	152.0	X			X	X		
9.5	60.0	154.0	X			X			
9.5	60.0	156.0	X				X	X	
10.0	55.0	152.0	X	X		X	X	X	
10.0	55.0	154.0	X	X		X		X	
10.0	55.0	156.0	X	X		X	X	X	
10.0	60.0	152.0	X	X			X		
10.0	60.0	154.0	X	X					
10.0	60.0	156.0	X	X			X		
10.0	65.0	152.0	X	X		X	X	X	

Velocity km/s	Altitude km	Angle-of-Attack deg.	Full		Reduced Velocity Level 1	Reduced Velocity Level 2	Reduced Altitude	Reduced Angle-of-Attack	Reduced Velocity Level 1 and Altitude	Reduced Velocity Level 2 and Altitude
			X	X	X	X	X	X	X	X
10.0	65.0	154.0	X	X		X		X	X	
10.0	65.0	156.0	X	X		X	X	X		
10.5	55.0	152.0	X			X	X			
10.5	55.0	154.0	X			X				
10.5	60.0	152.0	X				X			
10.5	60.0	154.0	X							
10.5	60.0	156.0	X				X			
10.5	65.0	152.0	X				X			
10.5	65.0	154.0	X							
10.5	65.0	156.0	X				X			
10.5	70.0	152.0	X			X	X			
10.5	70.0	154.0	X			X				
10.5	70.0	156.0	X			X	X			
11.0	70.0	152.0	X	X	X	X	X	X	X	X
11.0	70.0	154.0	X	X	X	X		X	X	X
11.0	70.0	156.0	X	X	X	X	X	X	X	X
11.0	75.0	152.0	X	X	X		X			
11.0	75.0	154.0	X	X	X					
11.0	75.0	156.0	X	X	X		X			
11.0	80.0	152.0	X	X	X	X	X	X	X	X
11.0	80.0	154.0	X	X	X	X		X	X	X
11.0	80.0	156.0	X	X	X	X	X	X	X	X

### C. Histograms of Percent Difference with Reduced Solution Resolution

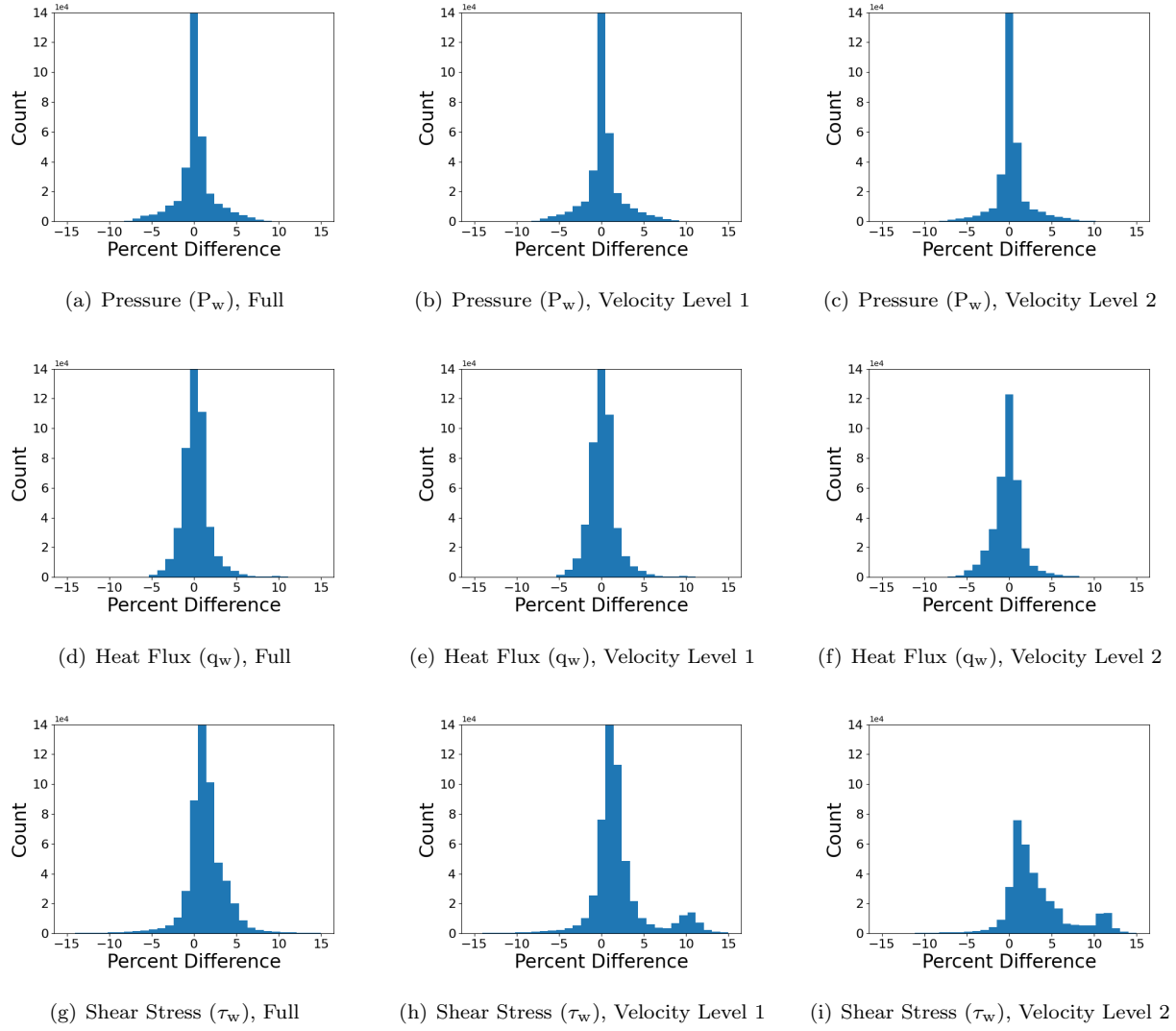


**Figure 44.** Histograms of percent difference of all surface elements from all the Apollo 4 solutions, helping to characterize the sensitivity of the dependent surface parameters ( $P_w$ ,  $q_w$ ,  $\tau_w$ ) with reduced resolution in the velocity dimension.

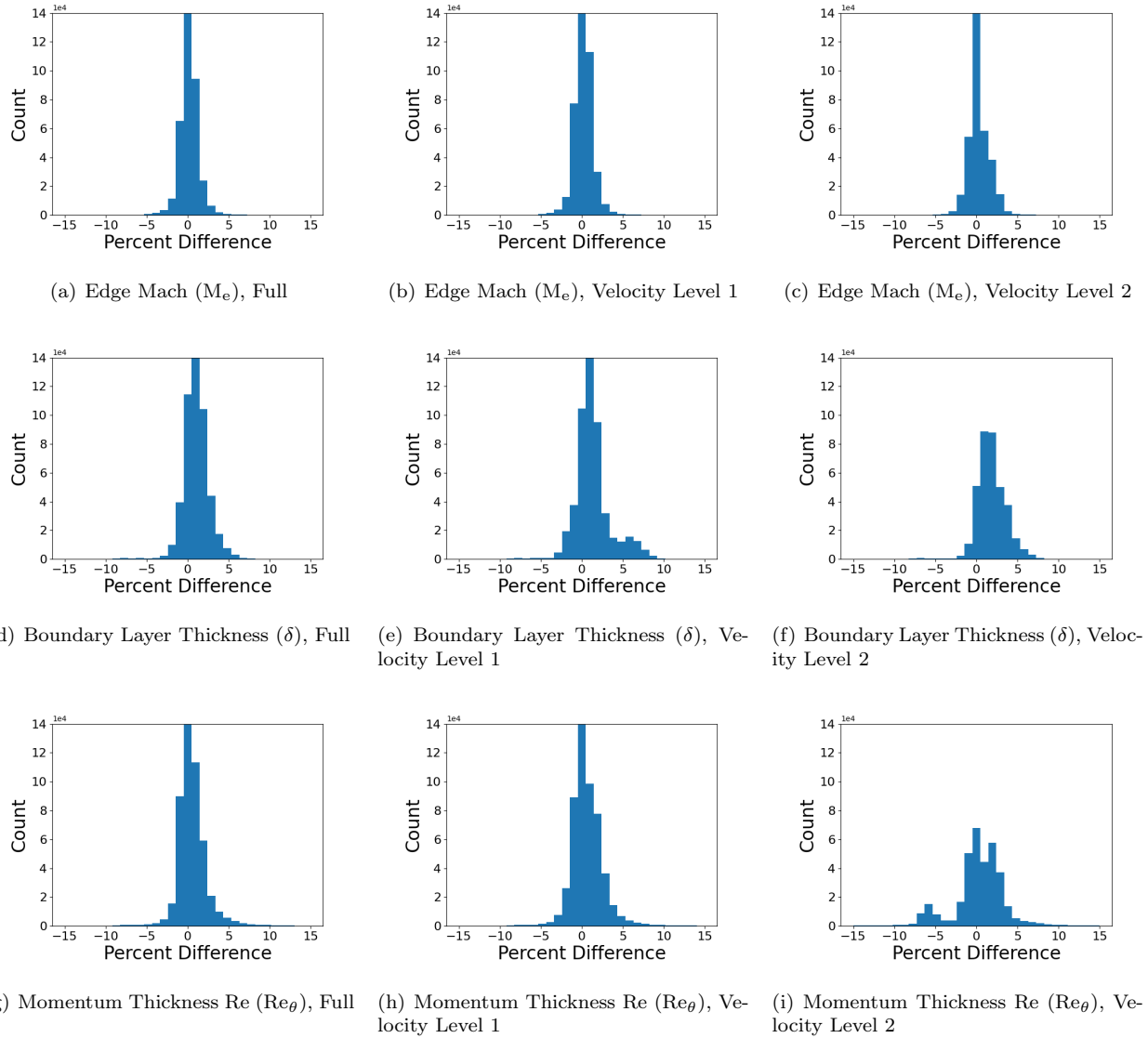
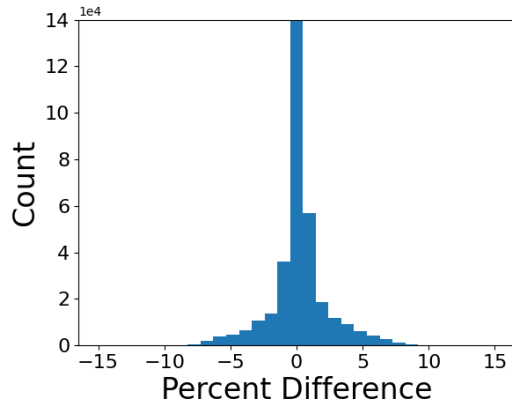
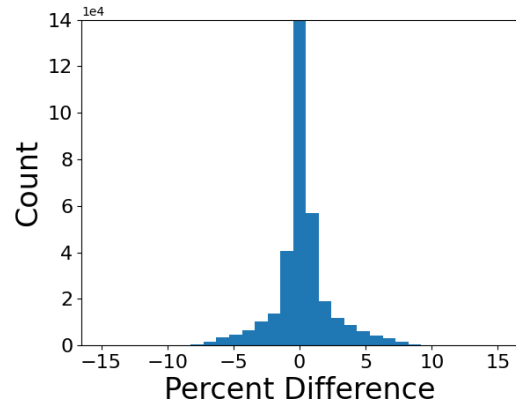


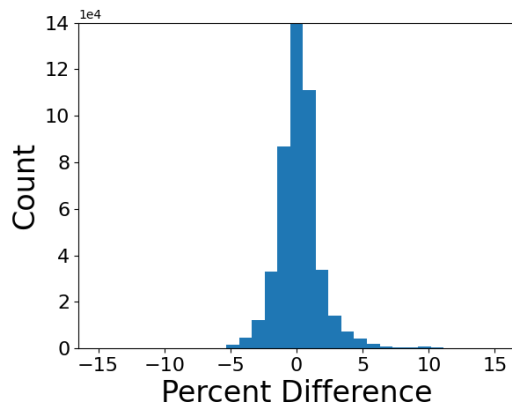
**Figure 45. Histograms of percent difference of all surface elements from all the Apollo 4 solutions, helping to characterize the sensitivity of the dependent boundary layer parameters ( $M_e$ ,  $\delta$ ,  $Re_\theta$ ) with reduced resolution in the velocity dimension.**



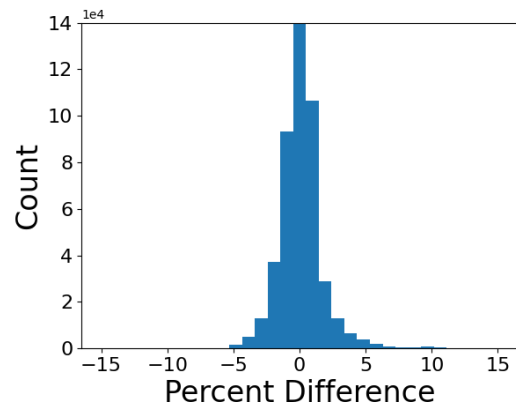
(a) Pressure ( $P_w$ ), Full



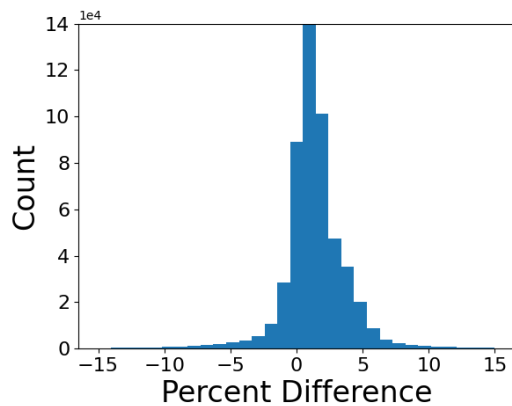
(b) Pressure ( $P_w$ ), Altitude



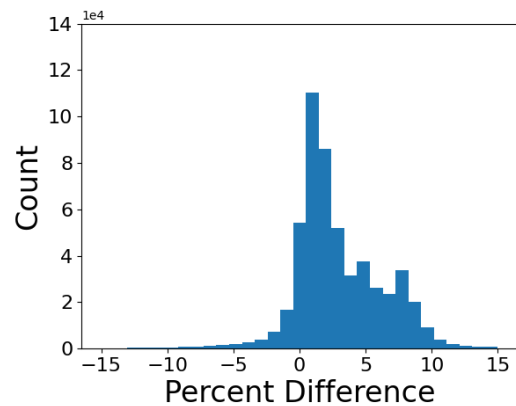
(c) Heat Flux ( $q_w$ ), Full



(d) Heat Flux ( $q_w$ ), Altitude

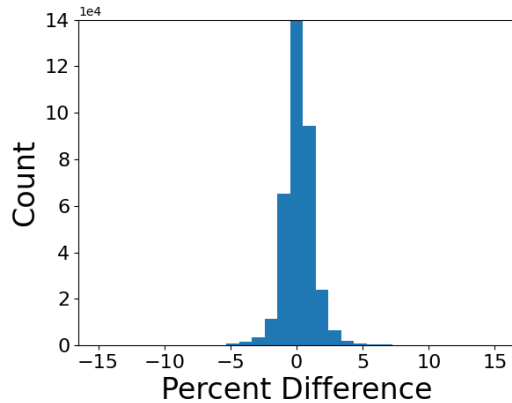


(e) Shear Stress ( $\tau_w$ ), Full

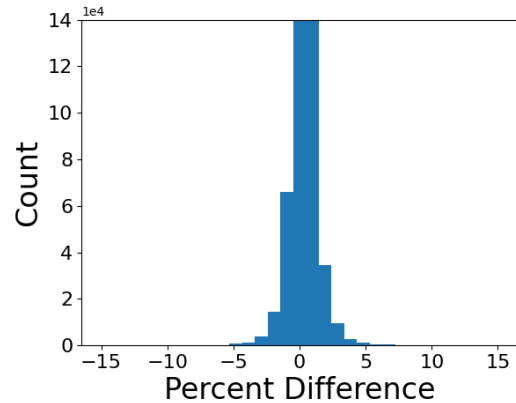


(f) Shear Stress ( $\tau_w$ ), Altitude

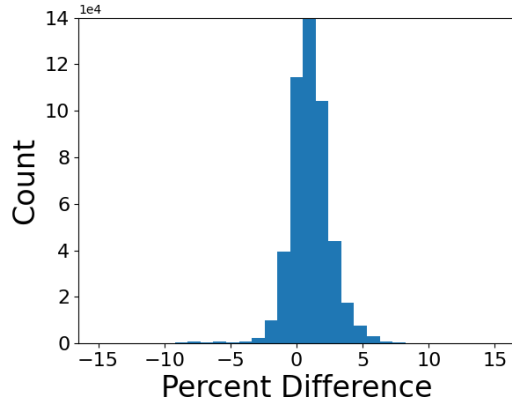
**Figure 46. Histograms of percent difference of all surface elements from all the Apollo 4 solutions, helping to characterize the sensitivity of the dependent surface parameters ( $P_w$ ,  $q_w$ ,  $\tau_w$ ) with reduced resolution in the altitude dimension.**



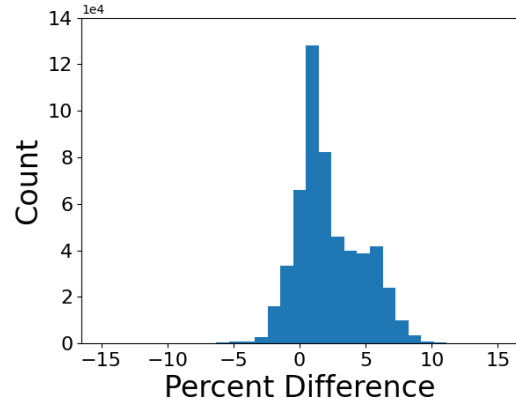
(a) Edge Mach ( $M_e$ ), Full



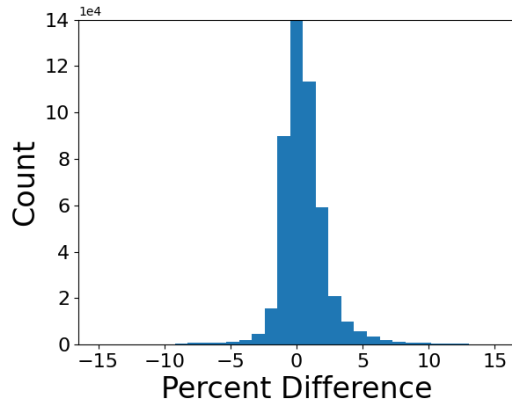
(b) Edge Mach ( $M_e$ ), Altitude



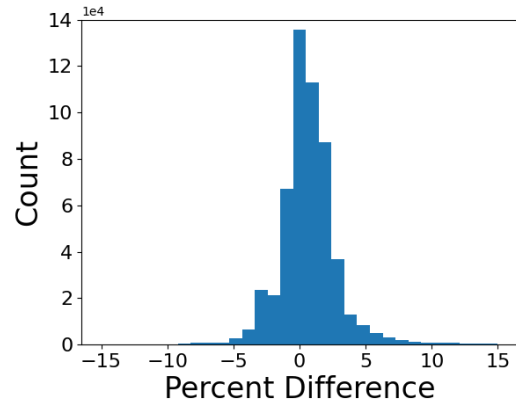
(c) Boundary Layer Thickness ( $\delta$ ), Full



(d) Boundary Layer Thickness ( $\delta$ ), Altitude

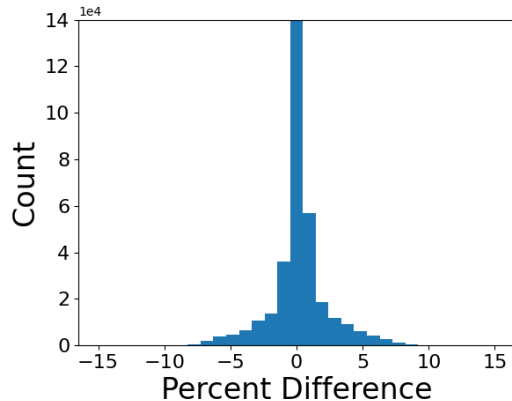


(e) Momentum Thickness Re ( $Re_\theta$ ), Full

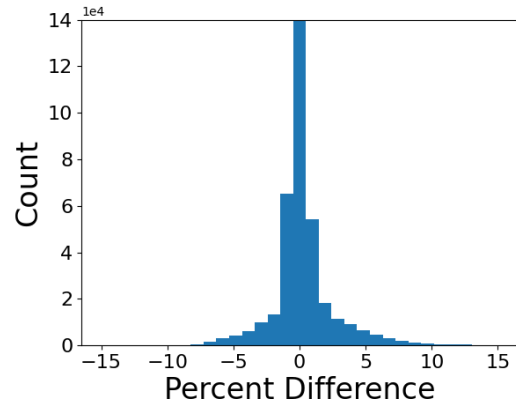


(f) Momentum Thickness Re ( $Re_\theta$ ), Altitude

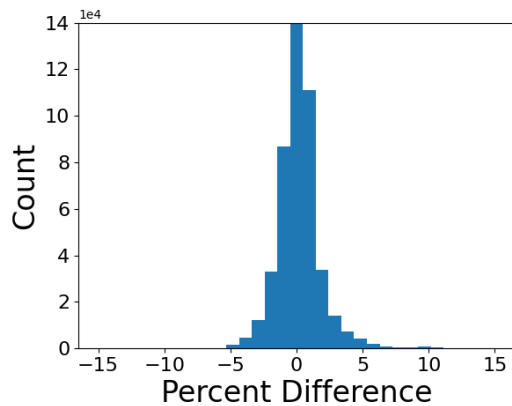
**Figure 47.** Histograms of percent difference of all surface elements from all the Apollo 4 solutions, helping to characterize the sensitivity of the dependent boundary layer parameters ( $M_e$ ,  $\delta$ ,  $Re_\theta$ ) with reduced resolution in the altitude dimension.



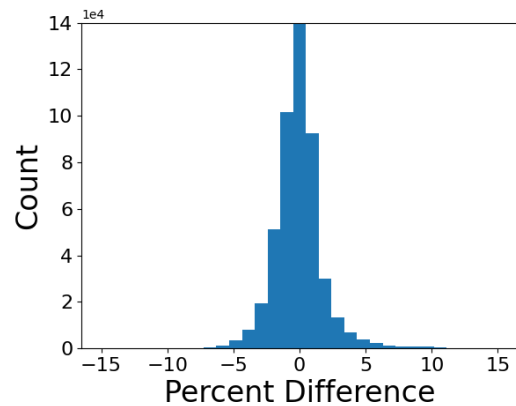
(a) Pressure ( $P_w$ ), Full



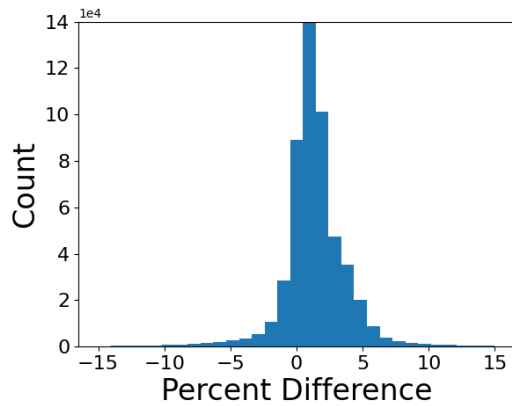
(b) Pressure ( $P_w$ ), Angle-of-Attack



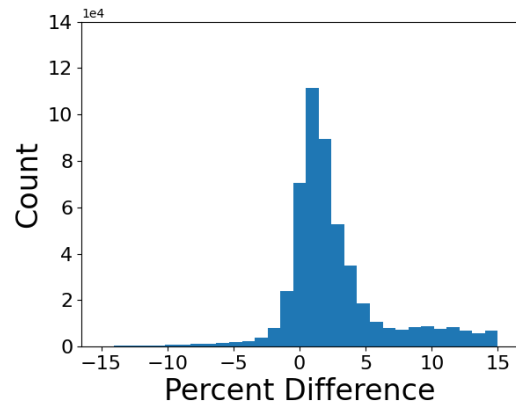
(c) Heat Flux ( $q_w$ ), Full



(d) Heat Flux ( $q_w$ ), Angle-of-Attack

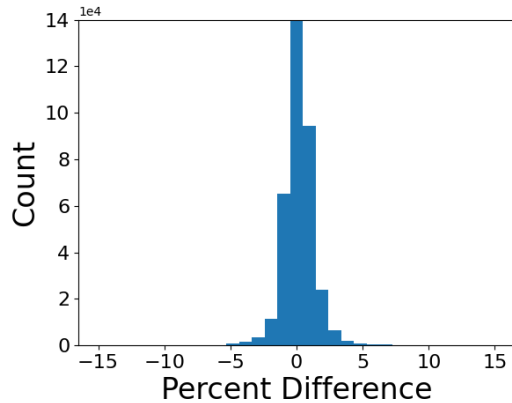


(e) Shear Stress ( $\tau_w$ ), Full

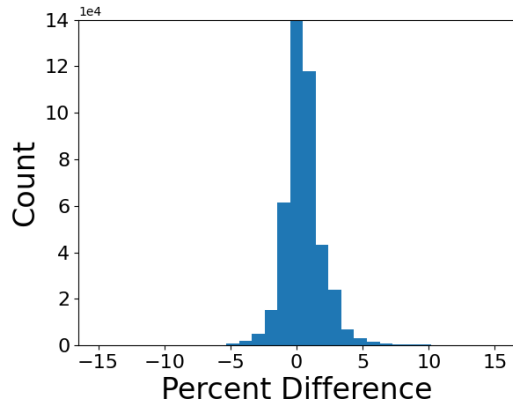


(f) Shear Stress ( $\tau_w$ ), Angle-of-Attack

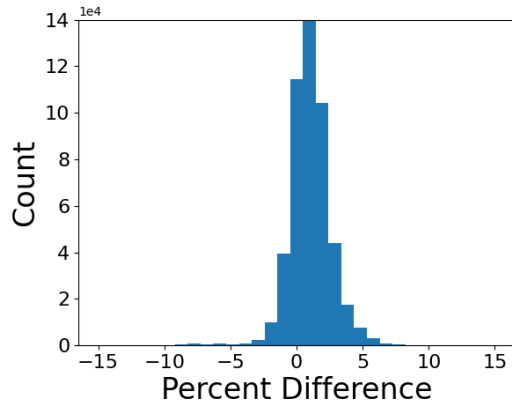
**Figure 48.** Histograms of percent difference of all surface elements from all the Apollo 4 solutions, helping to characterize the sensitivity of the dependent surface parameters ( $P_w$ ,  $q_w$ ,  $\tau_w$ ) with reduced resolution in the altitude dimension.



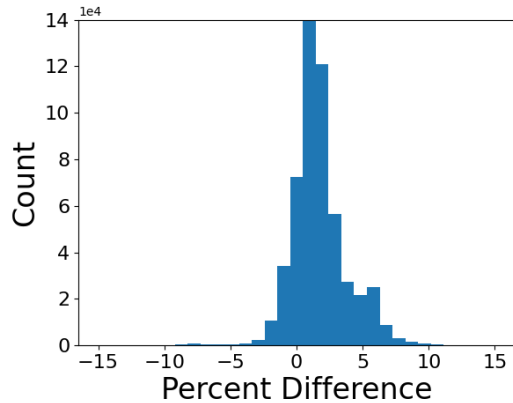
(a) Edge Mach ( $M_e$ ), Full



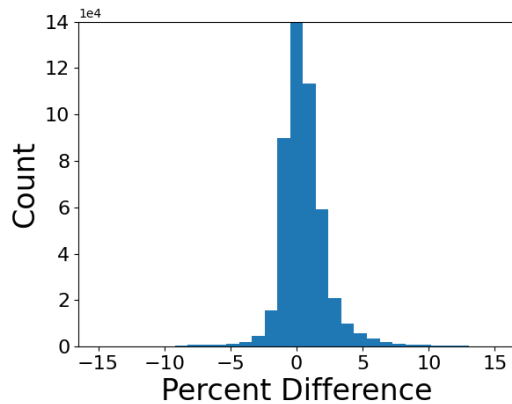
(b) Edge Mach ( $M_e$ ), Angle-of-Attack



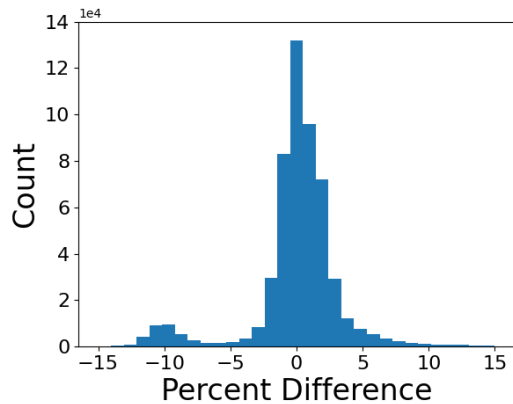
(c) Boundary Layer Thickness ( $\delta$ ), Full



(d) Boundary Layer Thickness ( $\delta$ ), Angle-of-Attack



(e) Momentum Thickness Re ( $Re_\theta$ ), Full



(f) Momentum Thickness Re ( $Re_\theta$ ), Angle-of-Attack

**Figure 49.** Histograms of percent difference of all surface elements from all the Apollo 4 solutions, helping to characterize the sensitivity of the dependent boundary layer parameters ( $M_e$ ,  $\delta$ ,  $Re_\theta$ ) with reduced resolution in the altitude dimension.

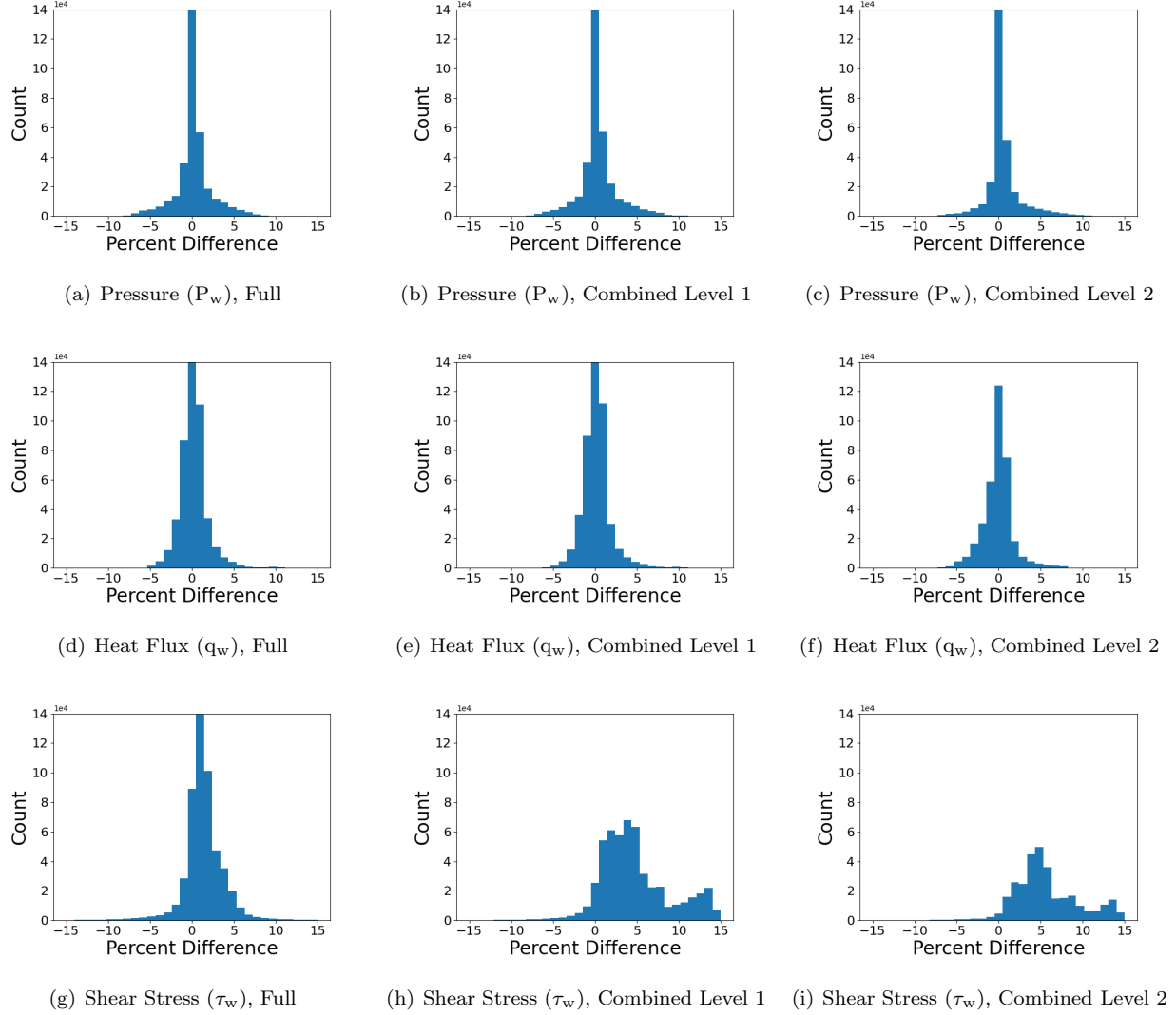


**Figure 50. Histograms of percent difference of all surface elements from all the Apollo 4 solutions, helping to characterize the sensitivity of the dependent surface parameters ( $P_w$ ,  $q_w$ ,  $\tau_w$ ) with reduced resolution in the combined velocity and altitude dimensions.**

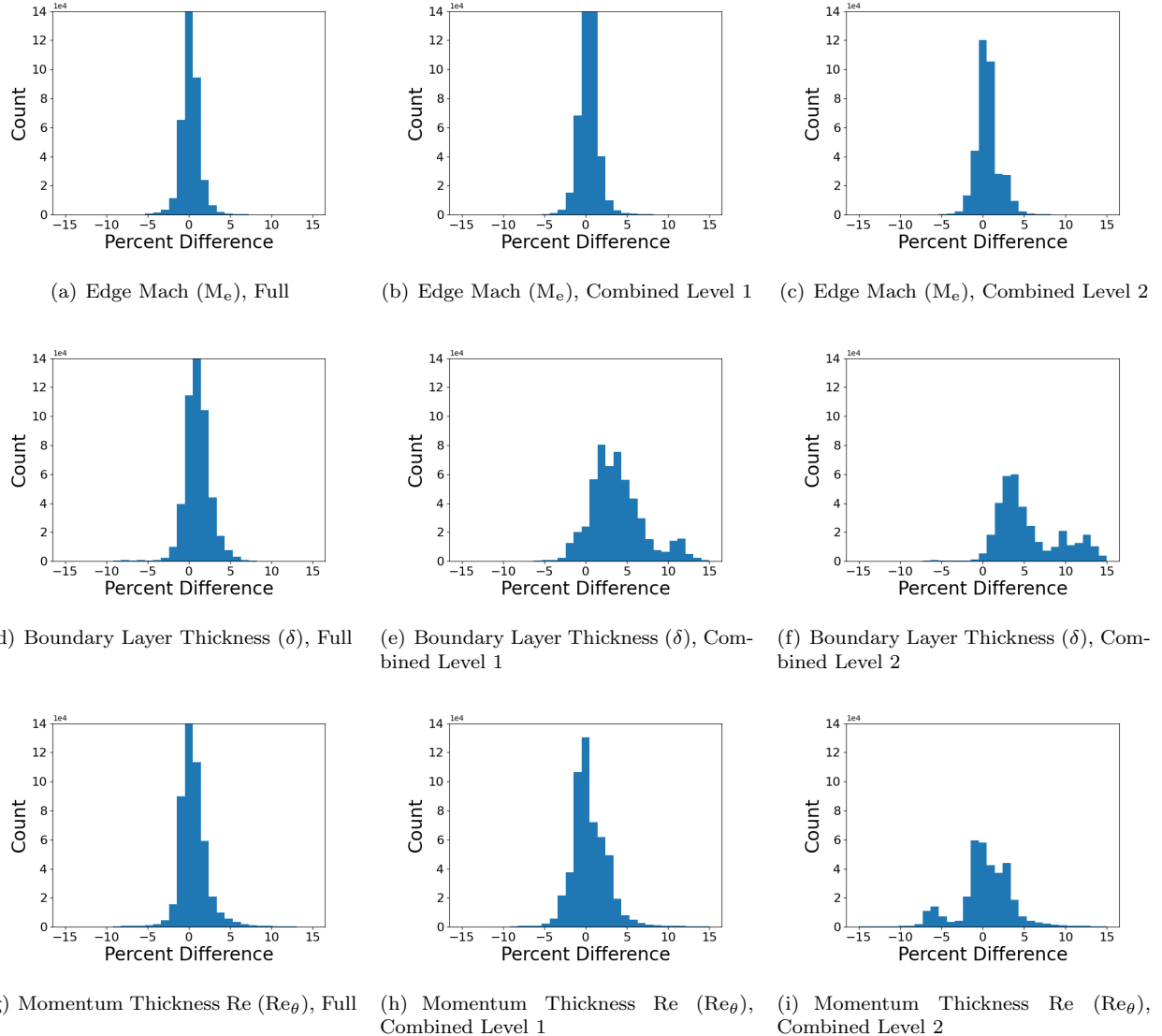


**Figure 51. Histograms of percent difference of all surface elements from all the Apollo 4 solutions, helping to characterize the sensitivity of the dependent boundary layer parameters ( $M_e$ ,  $\delta$ ,  $Re_\theta$ ) with reduced resolution in the combined velocity and altitude dimensions.**

## Acknowledgments

This investigation would not have been possible without the work of Alan Schwing (NASA Johnson Space Center) and Cameron Ebner (formerly NASA Johnson Space Center) in developing the STEAM tool. STEAM made it possible to quickly evaluate different interpolation spaces and high-fidelity solution densities. Additionally, Molly Bannon (NASA Johnson Space Center) generated the CFD solutions along the Apollo 4 trajectory.

## References

- <sup>1</sup>Fay, J. A. and Riddell, F. R., *Theory of Stagnation Point Heat Transfer in Dissociated Air*, Journal of the Aeronautical Sciences, February, 1958
- <sup>2</sup>Marvin, Joseph G. and Deiwert, George S., *Convective Heat Transfer in Planetary Gases*, AIAA Journal, April 1966
- <sup>3</sup>Sutton, K. and Graves Jr., R., *A general stagnation-point convective heating equation for arbitrary gas mixtures*, Tech. Rep. NASA TR R-376, 1971
- <sup>4</sup>Brandis, A. and Johnson, C. O., *Characterization of Stagnation-Point Heat Flux for Earth Entry*, AIAA-2014-2374, Atlanta, GA, 2014
- <sup>5</sup>Olynick, D., Loomis, M., and Chen, Y. K., *New TPS Design Strategies for Planetary Entry Vehicle Design*, AIAA 99-0348, Reno, NV, 1999.
- <sup>6</sup>Greene, F. and Hamilton, H., *Development of a Boundary Layer Properties Interpolation Tool in Support of Orbiter Return to Flight*, AIAA 2006-2920, San Francisco, CA, 2006.
- <sup>7</sup>Kinney, D., *Aerothermal Anchoring of CBAERO Using High Fidelity CFD*, AIAA 2007-608, Reno, NV, 2007.
- <sup>8</sup>Kinney, D., *Aero-Thermodynamics for Conceptual Design*, AIAA 2004-31, Reno, NV, 2004.
- <sup>9</sup>Hollis, Brian R., *Distributed Sand-Grain Roughness Effects on Blunt Body Hypersonic Transition and Heating*, AIAA 2024-0224,
- <sup>10</sup>Berry, Scott A. and Horvath, Thomas J., *Discrete Roughness Transition for Hypersonic Flight Vehicles*, AIAA-2007-0307, Reno, NV 2007
- <sup>11</sup>Everhart, Joel L., *Supersonic/Hypersonic Laminar Heating Correlations for Rectangular and Impact-Induced Open and Closed Cavities*, Journal of Spacecraft and Rockets, 2009
- <sup>12</sup>Everhart, Joel L. and Greene, Francis A., *Turbulent Supersonic/Hypersonic Heating Correlations for Open and Closed Cavities*, Journal of Spacecraft and Rockets, 2012
- <sup>13</sup>Wright, M., Prabhu, D., and Martinez, E., *Analysis of Apollo Command Module Afterbody Heating Part I: AS-202*, Journal of Thermophysics and Heat Transfer, 2006
- <sup>14</sup>Greathouse, J., Kirk, B., Lillard, R., Truong, T., Robinson, P., and Cerimele, C., *Crew Exploration Vehicle (CEV) Crew Module shape selection analysis and CEV Aerospace Project Overview*, AIAA 2007-603, Reno, NV, 2007.
- <sup>15</sup>Wright, Michael, *Data Parallel Line Relaxation Code*, Journal of Thermophysics and Heat Transfer, 2001
- <sup>16</sup>Park, C., *Chemical Kinetics for Air*, Journal of Thermophysics and Heat Transfer, 1990
- <sup>17</sup>Park, C., *Nonequilibrium Hypersonic Aerothermodynamics*, Wiley, 1990.
- <sup>18</sup>Ramshaw, J. *Self-Consistent Effective Binary Diffusion in Multicomponent Gas Mixtures*, Journal of Non-Equilibrium Thermodynamics, 15,295. 1990.
- <sup>19</sup>NOAA, *U. S. Standard Atmosphere, 1976*, 1976
- <sup>20</sup>Private communication, Saunders, D. AMA Incorporated
- <sup>21</sup>Scipy, <https://docs.scipy.org/doc/scipy/reference/generated/scipy.spatial.Delaunay.html>, 2024
- <sup>22</sup>Private communication, Schwing, A., Ebner, C., Amar, A., Hyatt, A. NASA Johnson Space Center
- <sup>23</sup>White, F. M. *Viscous Fluid Flow, 2nd Edition*, McGraw-Hill, 1991.